UNIVERSITÀ DEGLI STUDI PADOVA

Dipartimento di Fisica e Astronomia "Galileo Galilei"

Master Degree in Physics

Final Dissertation

Study of the ^{14}N(p,γ)^{15}O reaction in a wide energy range in underground with LUNA

Thesis supervisor
Prof. Antonio Caciolli
Thesis co-supervisor
Ph.D. Jakub Skowronski

Candidate
Vigolo Anna

Academic Year 2022/2023

Contents

Abstract

Stars derive their energy from thermonuclear reactions, which provide enough energy to counteract gravitational collapse and enter a state of hydrostatic equilibrium. These processes are also responsible for the production of elements ranging from helium to iron through nucleosynthesis. The ignition of hydrogen is provided by two mechanisms: the pp-chains and the CNO cycles. The CNO cycles, comprising sequences of nuclear reactions, play a significant role in the synthesis of carbon, nitrogen, oxygen, and fluorine. This thesis focuses on the investigation of the $^{14}N(p,\gamma)^{15}O$ reaction, the bottleneck of the first CNO cycle, which determines its energy production rate and influences the nucleosynthesis of carbon, nitrogen, and oxygen.

The cross section of this reaction has to be known with high accuracy since it is an important input parameter for the Standard Solar Model for determining solar abundances and the solar neutrino fluxes. Furthermore, the rate of the $^{14}N(p,\gamma)^{15}O$ reaction is important for dating the Globular Clusters stars and thus to estimate the age of the Universe.
Resonant states are of particular importance for determining the cross section behavior versus energy and for its extrapolation to low astrophysical energies. The resonant state at $E_r = 259$ keV in the center of mass reference frame is well known from previous measurements. In addition, a wide energy range of measurements from keV to MeV is required to obtain a good extrapolation of the cross section at low energies: for that purpose a new experiment at the new LUNA MV accelerator is planned for 2022-2023.

The objective of this thesis is the characterization of the TaN solid targets that will be employed for the new measurements, which represent one of the most important sources of uncertainty in the absolute cross section experiments. These targets are produced via implantation and sputtering techniques at LNL laboratories and at Lisbon. The analysis takes place at the LUNA 400 accelerator at the LNGS laboratories. A proton beam is delivered to the TaN targets and gamma rays emitted from the reaction are collected by a germanium detector. Long runs are alternated to scans of the $E_r = 259$ keV resonance in order to check targets' stability, to study contaminants and to determine targets' stoichiometry. What's more, an estimation of an important parameter such as the strength of the $E_r = 259$ keV resonant state can be obtained from the analysis of the resonance scans, thus to have a comparison with the literature value. Parameters obtained from these targets also allow for calculating the expected count rate for energies planned for the new experiment, ranging from 200 keV to 1.4 MeV. From those measurements it is possible to estimate the time required to acquire all the data with sufficient statistics and to plan new measurements foreseen for the new LUNA MV accelerator.

The thesis is organized into four chapters. The first one briefly describes stellar evolution and hydrogen burning processes, followed by the astrophysical relevance of the $^{14}N(p,\gamma)^{15}O$ reaction and on some results obtained in previous experiments. Cap. 2 describes the two techniques used to produce the targets analyzed in this thesis: sputtering and implantation. Cap. 3 introduces the LUNA 400 and LUNA MV accelerators and focuses on data analysis. Finally Cap. 4 concludes with a planning of the new measurements to be performed at the new LUNA MV accelerator.

1 The $^{14}N(p,\gamma)^{15}O$ reaction in stars

Stars are powered by thermonuclear fusion reactions that are responsible for energy production and nucleosynthesis. Hydrogen burning in stars is possible due to the pp chains and to the CNO cycles [1], which are sets of nuclear reactions that convert hydrogen into helium. The $^{14}N(p,\gamma)^{15}O$ reaction is the bottleneck of the first CNO cycle and controls its rate. The latter quantity is important to determine the turnoff luminosity point of a star, i.e. its departure from the main sequence to the phase of CNO burning, which is fundamental for dating the Globular Clusters stars and thus to have an estimation for the age of the Universe [9]. Furthermore, the cross section of this reaction is related to the Standard Solar Model (SSM) [7], which determines the Sun's chemical composition, and to the solar neutrino fluxes recently measured at Borexino [6]. Several experiments [13–17] were performed in order to obtain data for the cross section of the $^{14}N(p,\gamma)^{15}O$ reaction, focusing in particular on the resonant states, fundamental for the determination of the cross section energy dependence and for its extrapolation to low astrophysical energies [12]. The resonance at $E_r = 259$ keV in particular is a point of interest and is well known from previous measurements. A wide energy range of data from keV to MeV is required in order to have a good extrapolation of the cross section at low energies, the experiment to be performed at the new LUNA MV accelerator aims to obtain the cross section in a wide range up to 2 MeV [37]. In this thesis we focused on the production and analysis of the TaN targets produced at Lisbon and LNL laboratories via implantation and sputtering that will be used for the new measurements. Data is taken at the LUNA 400 accelerator at LNGS laboratories, where a proton beam is provided on the solid targets and a germanium detector is used to get the gamma rays from the $^{14}N(p,\gamma)^{15}O$ reaction.

1.1 Stellar evolution and hydrogen burning

Stellar evolution starts by the contraction of a gas cloud which is composed mainly by hydrogen and helium [1]. In this phase gravitational energy is transformed into thermal energy and radiation. At a certain point, some of the radiation is retained in the gas cloud instead of being released and the gravitational collapse slows down. Hydrogen then starts to dissociate and ionize, and when the central temperature reaches few million kelvins, firstly deuterium and then hydrogen start burning. At this stage stability is reached and the star enters the main sequence, which represents the longest phase of a star's life. In the Hertzsprung-Russel diagram [12], which shows the luminosity of a star as a function of its temperature in Fig. 1, the main sequence phase is represented by a diagonal line.

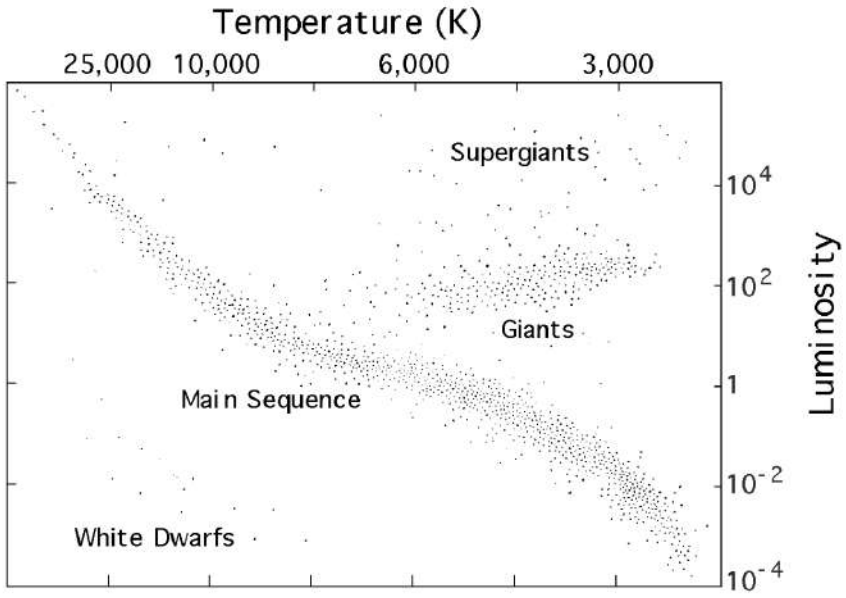

Figure 1: Hertzsprung-Russel (or color-magnitude) diagram: luminosity (relative to the Sun luminosity $L_\odot$) versus effective surface temperature. The regions of main sequence, giants and white dwarfs are indicated [12].

The evolutionary phases of a star and its entire lifetime strongly depend on its initial mass. Stars with initial masses in the range 0.013 $M_\odot$-0.08 $M_\odot$ do not evenly start burning hydrogen, since they are not able to reach the threshold temperature ($M_\odot$ is the mass of the Sun). These objects are known as brown dwarfs. If the initial mass ranges between 0.08 $M_\odot$ and 0.4 $M_\odot$, hydrogen is burnt via processes called pp-chains, but these stars are not able to start helium burning after H is exhausted: they end their lives as white dwarfs, cooling down by radiating away their energy.
A different path is followed by stars with masses in the range 0.4 $M_\odot$-2 $M_\odot$: depending on this value they burn hydrogen in the core through pp-chains or the CNO cycles (which we will better explain in this section). After they finish burning hydrogen in the core, these stars leave the main sequence and start to burn He, becoming red giants. At the end the envelope will be expelled in the cosmos and the star ends its life as a white dwarf.
If the initial mass exceeds 8 $M_\odot$, also carbon is burnt in the core after the He burning stage. Depending on its initial mass, the star ends its life as an oxygen-neon white dwarf after having expelled the hydrogen rich envelope, or continues burning heavier elements i.e. neon, oxygen and silicon [1], producing heavy and stable nuclei, the most abundant being ^{56}Fe. Heavy stars end their lives as neutron stars after core collapse exploding as supernovae (if the final core mass exceeds 1.4 $M_\odot$, the Chandrasekhar limit). The envelope can be ejected before core collapse by explosive nuclear burning [1]. If the core mass is sufficiently high, the star is unable to counteract gravity and it ends its life as a black hole.

Hydrogen burning in stars is possible thanks to the three pp chains (for low mass stars) and to the CNO cycles, in which carbon, oxygen and nitrogen are involved [4]. In both cases the final outcome of the process is:

$$4\mathrm{p} \rightarrow {}^4\mathrm{He} + 2\mathrm{e}^- + 2\nu + 26.73 \ \mathrm{MeV}. \tag{1}$$

Above 20 MK the dominant processes for hydrogen burning are the CNO cycles, while at lower temperatures most of the energy is produced by pp chains (this is shown in Fig. 2). Stellar temperature depends on its mass, as a consequence low mass stars will be dominated by

the pp chains, while in stars with mass slightly above the Sun's one CNO cycles will generate most of the nuclear energy.

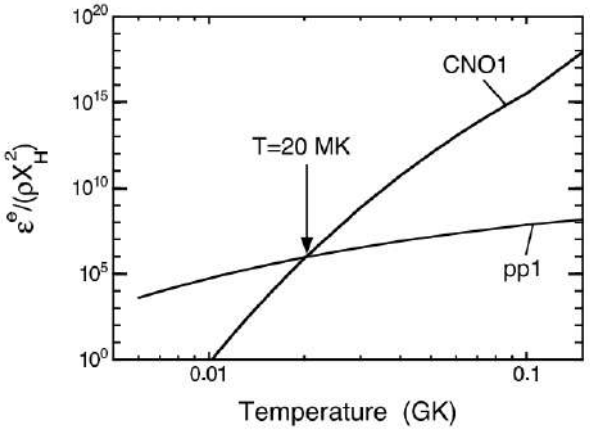

Figure 2: Equilibrium energy generation rates (normalized to the density ρ and to the square of the H mass fraction X_H) of the pp1 chain and the CNO1 cycle. The curve for the CNO1 cycle is calculated for a solar system composition [1].

The pp chains (displayed in Fig. 3) are three sequences of nuclear processes [1]. The first two reactions are common, then depending on the stellar temperature three different paths are possible. The first reaction involves the fusion of two protons into one deuterium nucleus, with the production of a neutrino and a positron. The deuterium produced by the first process is then destroyed by the d(p,γ)^{3}He reaction, thanks to the high amount of protons present in the environment compared to deuterium (the d+d interaction is more probable compared to proton capture on deuterium, but it is disfavored by the lower amount of d). The first pp chain is dominant at lower temperatures and involves the fusion of two ^{3}He nuclei to produce ^{4}He. In the second pp chain instead ^{3}He captures an α particle to produce a gamma ray and ^{7}Be, that decays into ^{7}Li, which in turns captures a proton to produce two α particles. At sufficiently high temperatures [1] the proton capture on ^{7}Be to produce ^{8}B dominates, and is followed by the β^+ decay of ^{8}B into ^{8}Be. The latter nucleus then breaks up into two ^{4}He nuclei.

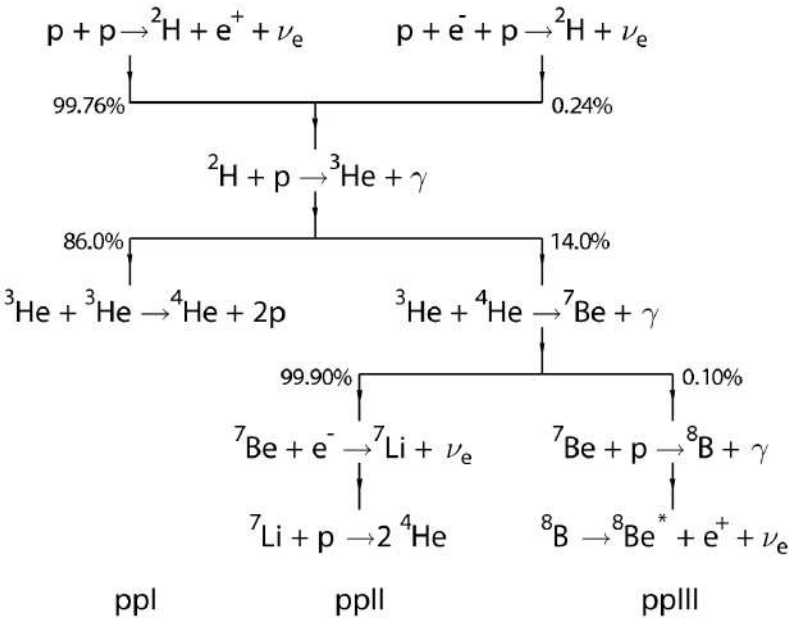

Figure 3: The pp chains for hydrogen burning [8].

If a star consists only of hydrogen and helium, the only mechanism to burn H are the pp chains; most stars however contain also heavier nuclides, in particular C, N and O. These nuclei, which are produced in a previous star generation, contribute to the hydrogen burning thanks to the CNO cycles [1], which are four loops of reactions involving C, N, O, and F (see Fig. 4). Since these heavier elements act as catalysts (i.e. their total abundance remains the same after one entire cycle), starting from a relatively low abundance a large amount of energy can be produced and the abundance of a single catalyst will change during the operation of one of these cycles.

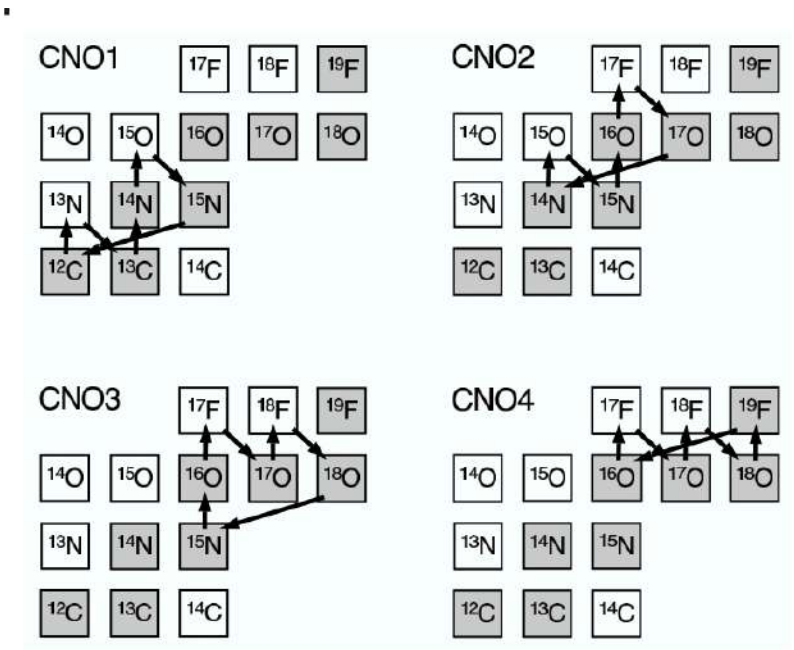

Figure 4: Representation of the four CNO cycles in the chart of the nuclides. Stable nuclides are shown as shaded squares. Each reaction cycle fuses effectively four protons to one ^{4}He nucleus [1].

The reactions involved are proton induced reactions on the C, N, O and F nuclei, among which there are radiative captures (p,γ) and (p,α) and β^+ decays of unstable nuclei. The

branching points between the cycles are represented by the proton captures on ^{15}N, ^{17}O, ^{18}O and ^{19}F, where the (p,α) reaction that closes a cycle competes with the radiative capture. The ratio of the probabilities between the (p,α) and (p,γ) is temperature dependent. The first cycle consists into proton captures on ^{12}C, ^{13}C, ^{14}N and ^{15}N and β^+ decays of ^{13}N and ^{15}O; the latter two reactions are responsible for the emission of two neutrinos of 1.20 MeV and 1.73 MeV respectively. The processes involved in the first CNO cycle are described by:

$$\begin{aligned} {}^{12}\mathrm{C} + \mathrm{p} &\rightarrow {}^{13}\mathrm{N} + \gamma \\ {}^{13}\mathrm{N} &\rightarrow {}^{13}\mathrm{C} + \mathrm{e}^+ + \nu \\ {}^{13}\mathrm{C} + \mathrm{p} &\rightarrow {}^{14}\mathrm{N} + \gamma \\ {}^{14}\mathrm{N} + \mathrm{p} &\rightarrow {}^{15}\mathrm{O} + \gamma \\ {}^{15}\mathrm{O} &\rightarrow {}^{15}\mathrm{N} + \mathrm{e}^+ + \nu \\ {}^{15}\mathrm{N} + \mathrm{p} &\rightarrow {}^{12}\mathrm{C} + \alpha. \end{aligned} \tag{2}$$

Since the ^{14}N(p,γ)^{15}O is the slowest reaction and thus the bottleneck of the cycle, it determines its energy production rate inside the hydrogen burning regions in equilibrium; in addition it controls the nucleosynthesis and therefore the C, N and O production.

1.2 Solar abundance problem

The solar chemical composition is fundamental to understand the formation, structure and evolution of the Sun and of the Solar System [5]. Abundances of the solar photosphere reflect the chemical composition of the Sun at its birth and can be studied starting from spectral absorption lines and theoretical models of the solar atmosphere. These models have to be constrained by observations: elemental abundances in the Sun can be also obtained from the CI chondrites or by helioseismology data [5].
CI chondrites are pristine meteorites which have modified their chemical composition about 4.56 Gy ago. The abundances of the elements found in these objects, normalized to the photospheric abundance of Si, can give information about the chemical abundances present at the Sun's birth. Volatile elements abundances like H, He, C, N, O and Ne cannot be estimated from CI chondrites because they easily evaporate. In Helioseismology acoustic waves propagating inside the Sun are observed at its surface and provide useful information about the solar temperature and chemical composition [11]. A key quantity for the propagation of these waves is the adiabatic sound speed, which varies with the depth inside the Sun: an increase in the sound speed is related to an increase in the temperature. Moreover, gradients of the temperature and sound speed are influenced by the opacity of the material, which is an important microphysical input for modelling the stars interiors. Helioseismology observation uses acoustic p-waves to map the solar depth: measured variation of the sound speed as a function of depth is compared with the expected values from model abundances.

The new solar model [5], based on a three dimensional hydrodinamical theory, predicts non volatile elemental photospheric abundances in good agreement with data from CI chondrites. Anyway for C, N, O and Ne lower abundances are estimated (if compared with previous models), which are not consistent with the observed helioseismology data, as seen in Fig. 5, where the variation of the sound speed with respect to the observed one as a function of solar depth is reported for three different models. The older model studied in 1998 is in a better agreement with observations due to higher predicted abundances. Furthermore, the calculated mass fraction of He at the surface $Y_s = 0.238$ is not compatible with the one given by helioseismology

($Y_s = 0.2485 \pm 0.0034$).

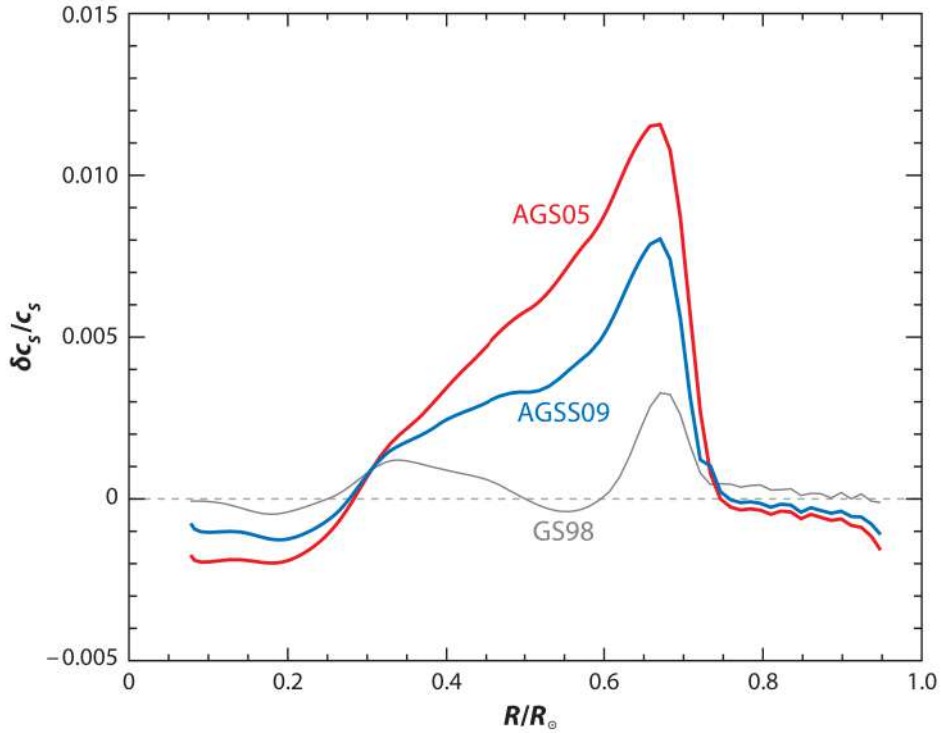

Figure 5: The differences between the helioseismic and predicted sound speeds c_s as a function of depth. The standard solar models shown here only differ in the assumed chemical compositions: Grevesse & Sauval (1998, here denoted as GS98), gray line; Asplund, Grevesse & Sauval (2005, AGS05), red line; and the present work (AGSS09), blue line [5].

The new models also provide a metallicity value 1.4 % lower compared with previous calculations by Anders and Grevesse on 1989 [5]. Since the metallicity predicted by a theoretical model modifies the conditions in the core, also neutrino fluxes coming from pp-chain and CNO cycles are affected. Neutrinos can also be detected experimentally, and due to their negligible probability of interaction with matter, they reach us giving direct information about the astrophysical site from which they originate. Further experimental constraints are expected from neutrino flux measurements (Borexino, SNO, SuperKamiokande) coming from ^{8}B beta decay in the third pp-chain and from the same process in the CNO cycles.

The evidence of CNO neutrinos was obtained in the Borexino experiment [6] performed at the Gran Sasso laboratories, using a large volume of liquid scintillator to detect gamma rays from scattered off electrons (originated from neutrino interaction with matter). The main issue was to isolate the signal attributed to CNO neutrinos from the background, represented mainly by ^{11}C and ^{210}Bi β decays, and neutrinos coming from the pep reaction, alternative to the first step of the pp chain. The count rate obtained for the CNO neutrinos was (5.6 ± 1.6) counts per day per 100 tons of liquid scintillator, confirming their presence at 3.5 σ level [6]. The reactions which contribute to the CNO solar neutrinos are:

$$\begin{aligned} {}^{13}\mathrm{N} &\rightarrow {}^{13}\mathrm{C} + \mathrm{e}^+ + \nu \\ {}^{15}\mathrm{O} &\rightarrow {}^{15}\mathrm{N} + \mathrm{e}^+ + \nu. \end{aligned} \tag{3}$$

It is supposed that the fluxes of neutrinos coming from ^{13}N and ^{15}O are used together with the ^{8}B ones to obtain information about the primordial C and N solar abundances [7, 8]. The Standard Solar Model (SSM) depends on about 20 input parameters: environmental ones, as

the solar age and luminosity, and nuclear parameters, in particular the cross sections of the pp chain and CN cycle reactions [7]. The environmental parameters are sensitive to the solar core temperature T_c, and the fluxes of solar neutrinos can be reconduced to this parameter. The strategy adopted is the one of measuring ^{8}B neutrino flux (related to the solar core temperature T_c) to calibrate environmental effects of the metals and other SSM parameters, with the aim of isolating the CN cycle dependence on primordial C and N abundances. Among the remaining limiting uncertainties one seems to be the one relative to the $^{14}N(p,\gamma)^{15}O$ reaction, that should be improved through cross section measurements. In Fig. 6 the expected neutrino spectrum based on previous calculations is reported.

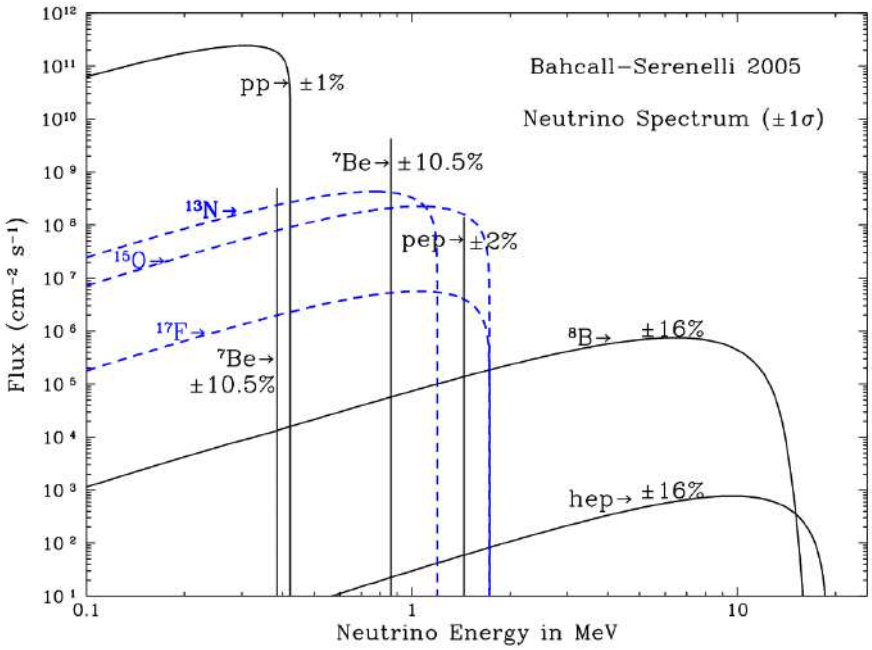

Figure 6: Expected neutrino spectrum based on BS05 model calculation: both fluxes from p-p chain (solid black) and CNO (dashed blue) are shown [12].

1.3 Turnoff luminosity point of the Globular Clusters

Another problem of interest related to the reaction studied in this thesis is the dating of the Globular Clusters stars [4, 9], which have similar age and chemical composition but different masses. These objects represent the oldest stellar population and were present during the period of formation of the first stars. The dating of this group of stars is important to set a limit on the age of the Universe.

The latter quantity can be determined from the turnoff luminosity point, for which stars of lower mass move off from the main sequence to the phase of CNO hydrogen burning; this is believed to happen at a temperature of about $20{\cdot}10^6$ K. The dating of these stars requires an accurate calibration of the turnoff luminosity-age relation [9], which depends on processes of energy generation and transport, and on the chemical composition of the star. Since thermonuclear reactions supply most of the energy irradiated from the surface and are responsible for chemical modification, the age of these stars depends on the rate of these reactions, in particular on the one of $^{14}N(p,\gamma)^{15}O$. An higher value of that rate implies fainter turnoff points for a fixed age, and younger ages for a given turnoff point. In Fig. 7 are reported the isochrones in the HR diagram corresponding to different rates of the $^{14}N(p,\gamma)^{15}O$ reaction.

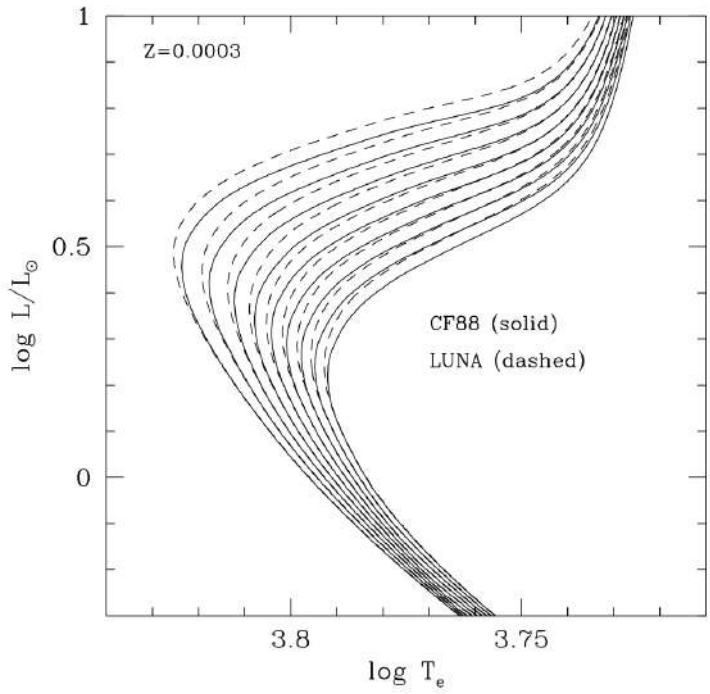

Figure 7: Isochrones for Globular Clusters obtained with different rates of the ^{14}N(p,γ)^{15}O reaction. The brightest isochrone (of each set) is the youngest (10 Gy),while the fainter is the oldest (18 Gy) [9].

A revision of the rate of this reaction [9, 12] led to a recalculation of the turnoff luminosity point. The lower rate estimated implies brighter turnoff luminosity points for a given age (the variation of the isochrones from the old (CF88) and new (LUNA) estimations are displayed in Fig. 7). Since this point is fixed by observations, the age of the cluster increases and also the lower limit to the age of the Universe [9] (with a variation of 0.7-1 Gy it reaches 14 $\pm$ 1 Gy).

1.4 Cross section of nuclear reactions

Nuclear reactions are fundamental for the evolution of the Universe: here we introduce the main astrophysical quantities of interest, such as the cross section, the reaction rate and the S-factor. If we consider a reaction between two bodies, its Q-value can be obtained from the energy conservation [1, 4]:

$$\mathrm{Q} = (\mathrm{M_1} + \mathrm{M_2} - \mathrm{M_3} - \mathrm{M_4})\mathrm{c}^2, \tag{4}$$

where $\mathrm{M_1}$ and $\mathrm{M_2}$ are the masses of the colliding nuclei, $\mathrm{M_3}$ and $\mathrm{M_4}$ the ones of the particles produced after the process. The cross section σ(E) of a nuclear reaction is defined as the ratio between the number of reactions per unit time $\mathrm{N_R/t}$ and the number of target nuclei $\mathrm{N_t}$ multiplied by the number of beam particles $\mathrm{N_b}$ per unit time and unit area A of the target:

$$\sigma = \frac{\mathrm{N_R/t}}{(\mathrm{N_b/(tA)})\mathrm{N_t}}. \tag{5}$$

For astrophysical purposes, an important quantity is the reaction rate, i.e. the number of reactions per unit volume and unit time, which can be obtained from the cross section definition:

$$\mathrm{r} = \frac{\mathrm{N_R}}{\mathrm{V}\cdot\mathrm{t}} = (\sigma \mathrm{N_t})\left(\frac{\mathrm{N_b}}{\mathrm{V}\cdot\mathrm{A}\cdot\mathrm{t}}\right) = \sigma v \frac{\mathrm{N_t}}{\mathrm{V}}\frac{\mathrm{N_b}}{\mathrm{V}}. \tag{6}$$

V is the volume and v the relative velocity between the target and the projectile nuclei. In a stellar plasma at thermodynamic equilibrium, the relative velocity v is not constant, it follows a probability distribution $\mathrm{P}(v)$. Thus the formula for the reaction rate becomes:

$$\mathrm{r}_{12} = \frac{\mathrm{n}_1 \mathrm{n}_2 \langle \sigma v \rangle_{12}}{(1+\delta_{12})}. \tag{7}$$

n_1 and n_2 are the densities of the particles involved in the reaction, the δ_{12} factor takes into account for identical particles, and $\langle \sigma v \rangle$ is defined as:

$$\langle \sigma v \rangle = \int_0^\infty v \mathrm{P}(v) \sigma(v) dv. \tag{8}$$

Nuclei in a stellar plasma move non relativistically and under non-degenerate conditions [1], so the probability distribution $\mathrm{P}(v)$ for the relative velocities is Maxwellian (assuming that the velocity distribution of interacting nuclei separately is Maxwellian). As a consequence, energies of particles moving inside hot stellar matter are described by the Maxwell Boltzmann distribution:

$$\phi(\mathrm{E})\mathrm{dE} = \frac{2}{\sqrt{\pi}} \frac{1}{(\mathrm{kT})^{3/2}} \sqrt{\mathrm{E}} \cdot \mathrm{e}^{\frac{-\mathrm{E}}{\mathrm{kT}}} \mathrm{dE}, \tag{9}$$

where T represents the local temperature and k is the Boltzmann constant.
The reaction rate $<\sigma(v)v>$ can be obtained by knowing the cross section $\sigma(\mathrm{E})$ of the reaction studied along with the energy distribution of the particles:

$$< \sigma(v)v > = \left[\frac{8}{\pi \mu (\mathrm{kT})^3} \right]^{\frac{1}{2}} \cdot \int_0^\infty \sigma(\mathrm{E}) \mathrm{e}^{\frac{-\mathrm{E}}{\mathrm{kT}}} \mathrm{E} \mathrm{dE}. \tag{10}$$

E is the energy in the center of mass reference frame and μ the entrance channel reduced mass. For charged particle induced reactions at energies below the Coulomb barrier nuclear reactions undergo through quantum tunneling and the cross section drops by several orders of magnitude due to the decreasing transmission probability. It can be described by [1]:

$$\sigma(\mathrm{E}) = \frac{1}{\mathrm{E}} \cdot \mathrm{e}^{-2\pi\eta(\mathrm{E})} \mathrm{S}(\mathrm{E}), \tag{11}$$

where the Gamow factor $\mathrm{e}^{-2\pi\eta}$ approximates the s-wave transmission probability and η is the Sommerfeld parameter, described by:

$$\eta(\mathrm{E}) = \frac{\mathrm{Z}_1 \mathrm{Z}_2 \mathrm{e}^2}{\hbar} \cdot \left(\frac{\mu}{2\mathrm{E}} \right)^{\frac{1}{2}}. \tag{12}$$

Z_1 and Z_2 are the atomic numbers of the incoming particles, μ the reduced mass of the entrance channel and e the electric charge. The Sommerfeld parameter is obtained by assuming that there is a Coulomb potential outside the nucleus, the projectile energy is much smaller than the Coulomb barrier height and there is no centrifugal term (s-wave approximation). The S(E) factor has a weaker energy dependence compared to the cross section because the exponential drop due to the Coulomb barrier was factored out. Particle induced reactions can be non resonant or resonant: in the first case the cross section varies smoothly with energy, in the second one it has strong variations in the vicinity of a specific value of the resonant energy. For non resonant processes to obtain the reaction rate we can substitute Eq. 11 in Eq. 10 to get:

$$< \sigma(v)v > = \left[\frac{8}{\pi \mu} \right]^{\frac{1}{2}} \cdot \frac{1}{(\mathrm{kT})^{\frac{3}{2}}} \int_0^\infty \mathrm{S}(\mathrm{E}) \exp\left(-\frac{\mathrm{E}}{\mathrm{kT}} - 2\pi\eta \right) \mathrm{dE}. \tag{13}$$

In this case, the S(E) factor does not vary strongly with the energy: the integral is dominated by the exponential term, which represents the Gamow peak. This quantity is defined for both resonant and non resonant processes and is important since it represents the narrow energy range in which nuclear reactions happen in the stellar plasma:

$$e^{-\frac{E}{kT}} \cdot e^{-2\pi\eta}. \tag{14}$$

The first exponential represents the contribution from the Maxwell Boltzmann distribution, while the second one is the Gamow factor. The Gamow peak has a maximum at an energy of:

$$E_0 = 0.122(Z_1^2 Z_2^2 \mu T_9{}^2)^{\frac{1}{3}} \qquad (\text{MeV}). \tag{15}$$

T_9 is the temperature in GK and μ is expressed in atomic mass units (u). This energy is usually larger than the maximum of the Maxwell Boltzmann distribution, indicating that reactions mostly take place on its high energy tail. The peak E_0 is shifted towards higher energies for increasing temperature and particle atomic number, still remaining below the Coulomb barrier value V_c for T<10 GK [1]. In addition, the probability of a reaction decreases with increasing charges of the particles involved in the reaction; processes with the smallest Coulomb barrier account for most of the nuclear energy generation, while higher barriers inhibit energy production. In Fig. 8 the Gamow peak versus energy for the $^{14}N(p,\gamma)^{15}O$ reaction is shown for two different temperatures: the location of the maximum increases with increasing temperatures.

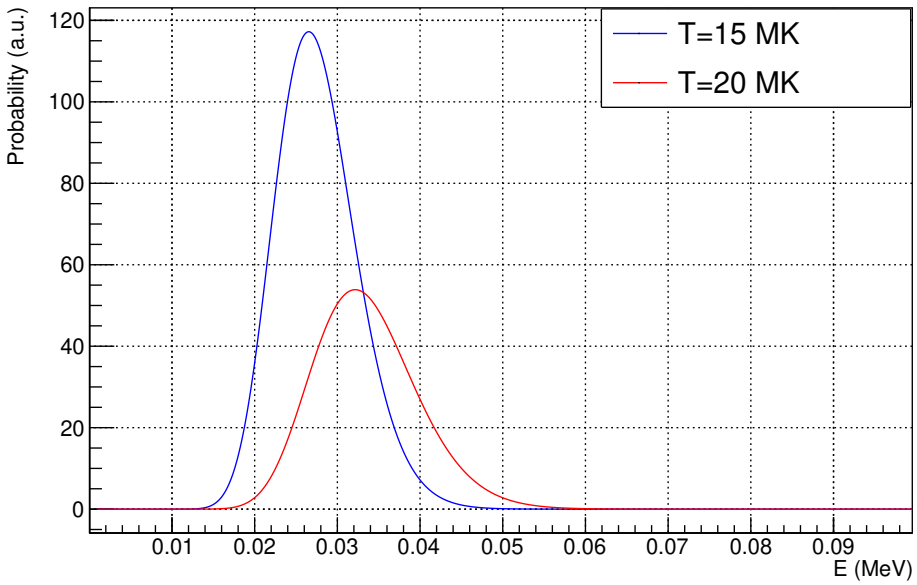

Figure 8: The Gamow peak vs energy for T = 15 MK and T = 20 MK for the $^{14}N(p,\gamma)^{15}O$ reaction. The curves are normalized by their area.

If the process instead is resonant, a compound nucleus would be formed at an excitation energy of $E_x = E_{cm} + Q$, where E_{cm} is the energy in the center of mass frame. This relation is valid only for particle capture reactions in which the compound nucleus formed coincides with the product of the reaction. In this case the cross section is described by the Breit Wigner formula [1]:

$$\sigma(E) = \frac{\lambda^2}{4\pi} \frac{2J+1}{(2J_1+1)\cdot(2J_2+1)} (1+\delta_{12}) \frac{\Gamma_a \Gamma_b}{(E-E_r)^2 + \Gamma^2/4}, \tag{16}$$

where J is the angular momentum of the compound, J_1 and J_2 the ones of the particles in

the entrance channel; E_r the resonance energy and Γ, Γ_a, Γ_b the total and partial widths of the resonant state; the de Broglie wavelength is given by:

$$\lambda = 2\pi\hbar/\sqrt{2\mu E}. \tag{17}$$

If we have a narrow resonance, in which the total width Γ is much smaller than the energy E_r, the exponential term $e^{-\frac{E}{kT}}$ in Eq. 10 and the partial widths Γ_i are approximately constant over the width of the resonance and the reaction rate can be described in terms of a parameter $\omega\gamma$, which represents the strenght of the resonance cross section, being proportional to the area under the $\sigma(E)$ curve. The reaction rate is thus described by:

$$< \sigma v >= \left(\frac{\sqrt{2\pi}\hbar^2}{(\mu kT)^{3/2}}\right) e^{-\frac{E_r}{kT}} \frac{(2J+1)(1+\delta_{12})}{(2J_1+1)(2J_2+1)} \frac{\Gamma_a\Gamma_b}{\Gamma} 2\int_0^\infty \frac{\Gamma/2}{(E_r-E)^2+\Gamma^2/4} dE \tag{18}$$

$$< \sigma v >= \left(\frac{2\pi}{\mu kT}\right)^{3/2} \hbar^2 e^{-\frac{E_r}{kT}} \omega\gamma \qquad \omega\gamma = \frac{(2J+1)(1+\delta_{12})}{(2J_1+1)(2J_2+1)} \frac{\Gamma_a\Gamma_b}{\Gamma}. \tag{19}$$

In this case ($\Gamma \ll E_r$) the reaction rate depends only on the resonance energy and on the $\omega\gamma$ factor, but not on the exact shape of the cross section curve [1].

1.5 The ^{14}N(p,γ)^{15}O reaction

The ^{14}N(p,γ)^{15}O reaction consists in proton capture by the ^{14}N nuclei and production of ^{15}O via a non resonant (direct capture) or a resonant mechanism [12]. Prompt gamma rays from capture to a state of ^{15}O are emitted together with secondary photons in cascade (if the level populated by the first gamma transition is an excited one). The reaction has a Q-value at 7297 keV and the most important resonances for astrophysical interest are located at E_r = 259 keV and 987 keV, including also a subthreshold resonance at E_r = -505 keV in the center of mass frame. In Fig. 9 a scheme of the excited levels of ^{15}O is reported.

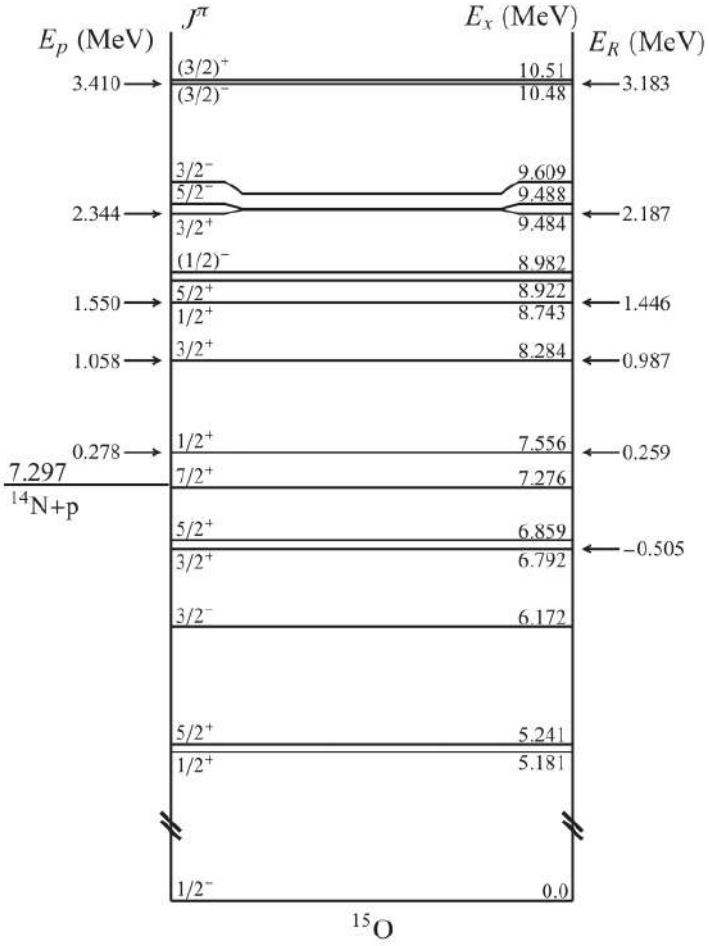

Figure 9: Level scheme of the ^{15}O compound nucleus. The laboratory frame (E_p) and center of mass frame (E_R) energies and corresponding excitation energies (E_x) are given [17].

Resonances play a major contribution in determining the trend of the cross section versus energy and in the extrapolation to very low energies of astrophysical interest [12]. The 259 keV resonance in particular is a point of interest and its strength is well known with 5 % uncertainty: $\omega\gamma_{th}$ = (13.7 ± 0.7) meV (value taken from [1]). When the energy in the center of mass reaches 259 keV, the excited state at 7.556 MeV in the ^{15}O nucleus is populated. This state decays either directly to the ground state or by cascades on the 6.792, 6.172 and 5.181 MeV excited states [17]. They are related to the emission of four primary gamma rays at E_γ = (763.4 ± 1.7) keV, (1380.1 ± 1.7) keV, (2373 ± 1) keV and (7554.5 ± 0.4) keV; furthermore, three secondary gamma rays are emitted in cascade after the primary ones at E_γ = (6791.4 ± 1.7) keV, (6174.9 ± 1.7) keV and (5182 ± 1) keV [1]. Also the subthreshold resonance at E_r = -505 keV corresponding to the 6792 keV excited state of ^{15}O plays a role, especially for what concerns the contribution of the capture to ground state transition [12].

Several experiments were performed in the previous years in order to get the cross section behavior and the extrapolation of the S-factor at zero energy for each of the main transitions of the reaction under study: one of the first estimations of the $S_{tot}(0)$ factor was from an experiment performed in 1987 at Bochum, Munster and Toronto [13], using a proton beam on evaporated TiN targets and implanted TaN ones, and exploring the energy range E_p = 0.18-3.6 MeV. A Ge detector was used to detect gamma rays from primary and secondary transitions of ^{15}O. They gave a value of $S_{tot}(0)$ = (3.2 ± 0.54) keV b, while the estimation for the capture to ground state transition contribution $S_{GS}(0)$ to the total $S_{tot}(0)$ factor was $S_{GS}(0)$ = (1.55 ± 0.34) keV b.

[1] Data of the gamma transitions are taken from *https://www.nndc.bnl.gov/nudat3/*.

These two values are supposed to be overestimated, in particular due to a re-measurement of the width of the subthreshold resonance corresponding to the excited level of 6792 keV in ^{15}O [20]. Due to the reduction of the subthreshold resonance width, the $S_{GS}(0)$ contribution to the total $S_{tot}(0)$ factor was supposed to be lower than previous estimations [21], and confirmed by new direct measurements of the cross section at TUNL [14], LUNA in 2005 [16] and at HZDR in 2017 [15]. In addition to using a too high value estimated for the total width of the 6792 keV state, the Bochum group also did not consider the summing in effects.

The experiment performed in 2004 at the LENA facility at TUNL provided a proton beam in the energy range E_p = 155-524 keV with implanted TaN targets. Gamma rays were detected in single and in coincidence with a germanium and a NaI(Tl) detector. They extrapolated the contribution to the total S-factor at zero energy $S_{GS}(0) = (0.49 \pm 0.08)$ keV b, about one third of the value reported from the experiment performed in 1987.
LUNA measurements were obtained at the Gran Sasso laboratories in 2005, using a proton beam up to 500 μA intensity and solid sputtered TiN targets, in the energy range between 119 keV and 367 keV in the center of mass reference frame. They used Ge detectors in two geometry configurations to get the gamma rays from the ^{14}N(p,γ)^{15}O transition. They obtained a value of $S_{GS}(0) = (0.25 \pm 0.06)$ keV b. The experiment performed in 2017 in Dresden (HZDR) explored the energy range between 0.357 MeV and 1.292 MeV using proton beams and sputtered TiN targets on tantalum backings. Two HPGe detectors were shielded by a BGO scintillator for escape suppression. The value reported for the $S_{GS}(0)$ contribution was $S_{GS}(0) = (0.19 \pm 0.05)$ keV b [15], significantly lower than the one reported by the Bochum studies.
Another experiment was performed at Notre Dame University in 2016 [17] in the E_p = 0.7-3.6 MeV energy range, using a proton beam on sputtered TiN and implanted TaN targets, detecting the gamma rays with Ge detectors. They gave a value of $S_{GS}(0) = (0.42 \pm 0.04)$ keV b, lower than the Bochum one but almost double than the one reported by HZDR [15]; large inconsistencies between the low energy data and the extrapolation of the S_{GS} value at zero energy suggested a systematic uncertainty of $^{+0.09}_{-0.19}$ keV b.
The Dresden experiment performed in 2017 [15] also focused on the S-factor relative to the capture to the 6.79 MeV excited level of ^{15}O, which accounts for about 70% of the total cross section. Its S-factor curve is flat over a wide energy range, displaying the dominance of direct capture contribution. They reported a value of $S_{6.79}(0) = (1.24 \pm 0.11)$ keV b, while other two works provided slightly higher values. In Tab. 1 are reported extrapolations of the S-factor at zero energy from different works for the most important transitions of the ^{14}N(p,γ)^{15}O reaction.

Transition	Bochum [13]	HZDR [15]	TUNL [14]	LUNA [16]	Notre Dame [17]
R/DC→6.79	1.41 ± 0.02	1.24 ± 0.11	1.15 ± 0.05	1.20 ± 0.05	1.29 ± 0.04 (stat) ± 0.09 (sys)
R/DC→6.18	0.14 ± 0.05		0.04 ± 0.01	0.08 ± 0.03	
R/DC→5.24	0.018 ± 0.003			0.070 ± 0.003	
R/DC→5.18	0.014 ± 0.004			0.010 ± 0.003	
R/DC→0	1.55 ± 0.34	0.19 ± 0.05	0.49 ± 0.08	0.25 ± 0.06	0.42 ± 0.04 (stat)$^{+0.09}_{-0.19}$ (sys)
Sum	3.20 ± 0.54		1.68 ± 0.09	1.61 ± 0.08	

Table 1: Extrapolation of the S factor (in keV b) to zero energy for the most important transitions of the ^{14}N(p,γ)^{15}O reaction. R/DC stands for capture to the 259 keV resonance (R) or direct capture contribution (DC).

For what concerns the experimental data, the HZDR measurements taken in the 2017 experiment for the capture to the 6.79 MeV transition are higher if compared with Bochum data at energies in the range 1000-1300 keV, showing a slope about 25% higher. Fewer of Dresden data are available for the capture to the ground state transition, and there is only one

point which overlaps with low energy data from previous experiments [15]. The extrapolations obtained from the HZDR measurements show discrepancies at lower and higher energies if compared with Notre-Dame ones. In Fig. 10 and 11 are reported the S-factors vs energy of the capture to 6.79 MeV and capture to ground state transitions taken from previous experiments [13, 15, 16, 18, 19]. The aim of the LUNA MV experiment is to obtain new data for the cross section of this reaction in a wide energy range, overlapping with the previous low energy data, in order to obtain a good extrapolation for the S-factor at low astrophysical energies.

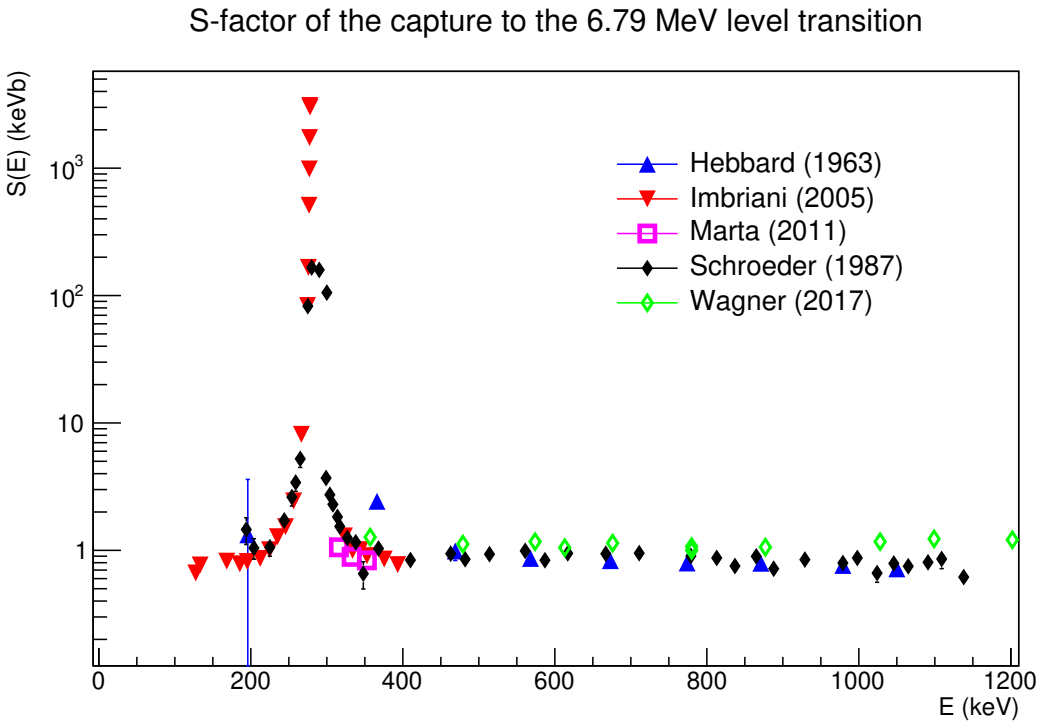

Figure 10: S-factor vs energy for the capture to 6.79 MeV transition in the ^{14}N(p,γ)^{15}O reaction (Data taken from [13, 15, 16, 18, 19]).

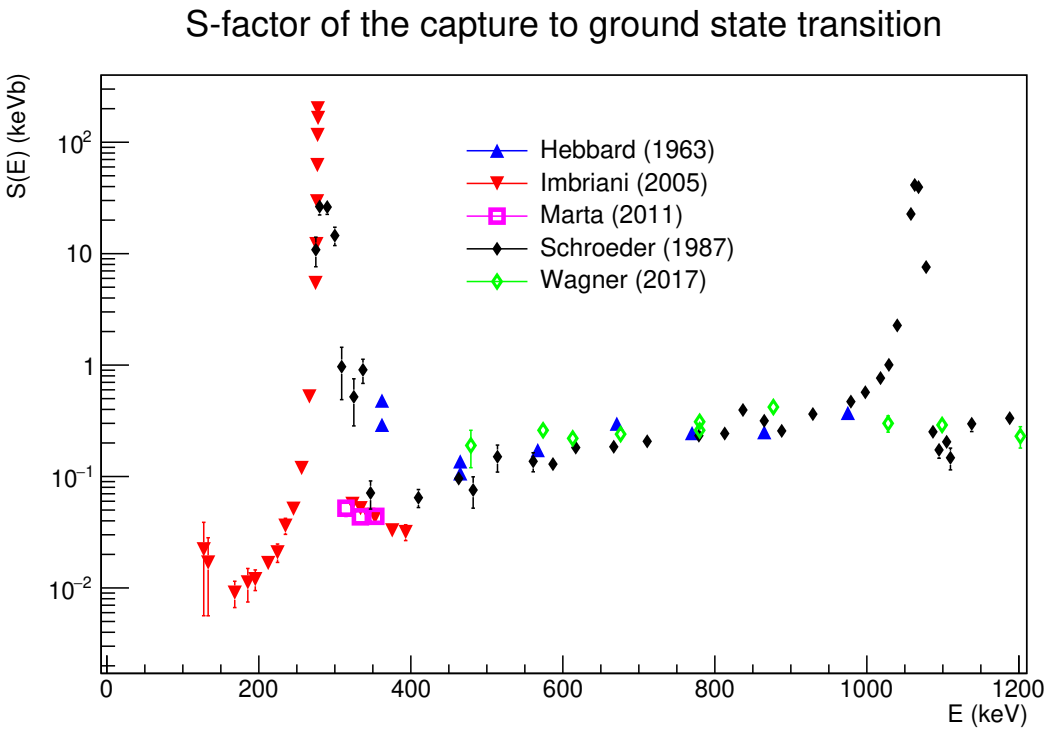

Figure 11: S-factor vs energy for the capture to ground state transition in the ^{14}N(p,γ)^{15}O reaction (Data taken from [13, 15, 16, 18, 19]).

2 Planning the new experiment

As discussed in section 1.5, the study of the $^{14}N(p,\gamma)^{15}O$ reaction in a wide energy range, overlapping also the low energy LUNA data, is extremely important. This can be done with the new LUNA-MV accelerator, recently installed at the "Bellotti" ion beam facility at LNGS. With this accelerator we could study the cross section from 1.4 MeV down to the 259 keV resonance. To plan an experiment such this it is important to study carefully the experimental setup and this thesis is focused on one of the most important sources of uncertainty in the absolute cross section experiments, such as the targets. We will discuss the production of those and their characterization using the LUNA 400 accelerator.

In this chapter are reported the two main techniques used to produce the TaN targets analyzed at LNGS: sputtering and implantation. Sputtering is an example of a Physical Vapor Deposition (PVD) process, which consists of the evaporation of a target material that is then transported to the substrate. Implantation instead is based on the bombardment of the target with the ions of the active material. In the sections below we firstly report some examples of PVD techniques including sputtering. Then we focus on the latter technique and on its application at LNL, where the sputtered targets used at LNGS laboratories are produced. Then we describe the target implantation. Finally, the Rutherford Backscattering (RBS) technique used for target analysis is displayed.

2.1 PVD techniques and sputtering

PVD (Physical Vapor Deposition) [23, 24] are processes where a species of a target material is transformed into vapor phase and then transported from the source to the substrate where it condensates. Typically it is used to deposit films with thicknesses of 1-100 nm, that can be composed by a single element or by a chemical compound. In the latter case the process is called "reactive" because the depositing material reacts with the ambient gas environment (e.g. N if we want to sputter TaN). Some categories of PVD are vacuum deposition or vacuum evaporation, arc vapor deposition, ion plating and in particular sputtering.

Vacuum deposition consists in thermal evaporation of the target material, without interaction with the molecules present in the environment. Generally heated sources like tungsten wire coils or high energy electron beams are used to vaporize the target material. High vacuum levels are required to reduce gaseous contamination, with pressure values usually between 10^{-5} and 10^{-9} Torr. Thermal vaporization has a higher rate compared to other vaporization methods. Arc vapor deposition makes use of a high current and low voltage arc to vaporize a cathodic or an anodic electrode; the vaporized material is highly ionized and a bias is applied to the substrate in order to accelerate ions towards it. Ion plating uses energetic particles to bombard the depositing film to modify and control its properties. It can be done both in a plasma environment or in vacuum and can provide dense coatings.

Sputter deposition is instead obtained through physical processes, where the surface of the target ejects particles due to momentum transfer between an energetic ion and the molecules of the material to be sputtered. Ions can be produced from a plasma source at low pressure (typically noble gases like Ar at pressures below 5 mTorr are used) or by an ion gun in vacuum. Plasma ions can be confined near the target or fill all the region up to the substrate. An important quantity is the sputtering yield, defined as the number of particles emitted by the target per incident ion. It depends on several factors like the mass and energy of the incident particles, the angle of incidence and the strength of the chemical bonds of the atoms on the surface. The pressure on the sputtering chamber instead affects the deposition of the sputtered material on the substrate: at high pressure gas-phase collisions can take place, deviating the

particles ejected from the target and affecting the film formation process on the substrate.

2.1.1 Target production at LNL

Sputtered targets of TaN are produced at LNL laboratories through the sputtering and reactive sputtering techniques. The TaN layer is part of a composite substrate. In Fig. 12 is shown the '129' sputtered target produced at LNL.

Figure 12: Photograph of the '129' sputtered target taken on 28/03/2023.

The sputtering chamber used at LNL consists in an external case which acts as anode (grounded), a substrate kept at the same voltage as the anode and a cathode at negative potential made of Cu and magnets of Nd on which a target is deposited. An argon plasma ion source is used. A schematic view of the chamber is shown in Fig. 13. Since magnets lose their magnetic properties above the Curie temperature T_C, water cooling of the system is needed. Magnets are used to confine secondary electrons on the target surface [25]. They are arranged in such a way that one pole is positioned at the central axis of the target and the second pole is formed by a ring of magnets around the outer edge. A magnetic field parallel to the target surface constrains the electrons on its vicinity. Trapping the electrons increases the ionizing electron-atom collision probability: this leads to an increased plasma density in the target region, and consequently to further sputtering and to an increased deposition rate on the substrate.
The chamber is kept in vacuum at a pressure of $4.5{\cdot}10^{-3}$ mBar, obtained through a turbomolecular pump and read by a capacitance pressure gauge. The voltage difference between cathode and anode is kept at V_b, which represents the voltage needed to have plasma discharge. The breakdown voltage V_b is gas dependent and is represented by the Paschen curves [26, 27] in Fig. 14, which shows different behaviors for He, Ne, Ar, H_2 and N_2. Since the breakdown voltage depends also on the product of the anode-to-cathode distance and on the pressure, we can control the latter quantity to obtain the voltage difference corresponding to the minimum of the Paschen curves.

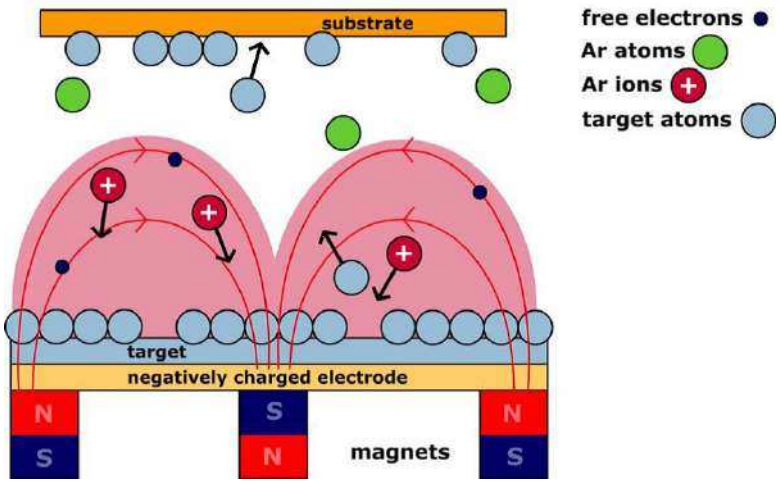

Figure 13: Scheme of the magnetosputtering chamber.

Pulsed DC voltage is provided to the target in order to avoid the production of an electric field between the target itself and the positive ions of Ar that attach to the insulating layer of TaN. This electric field would cause a voltage drop on this layer and decreases the sputtering rate. Furthermore at a critical voltage [22] arcing would form due to a breakdown of the insulating layer. By changing the polarity it is possible to attract electrons to that layer and prevent this phenomenon.

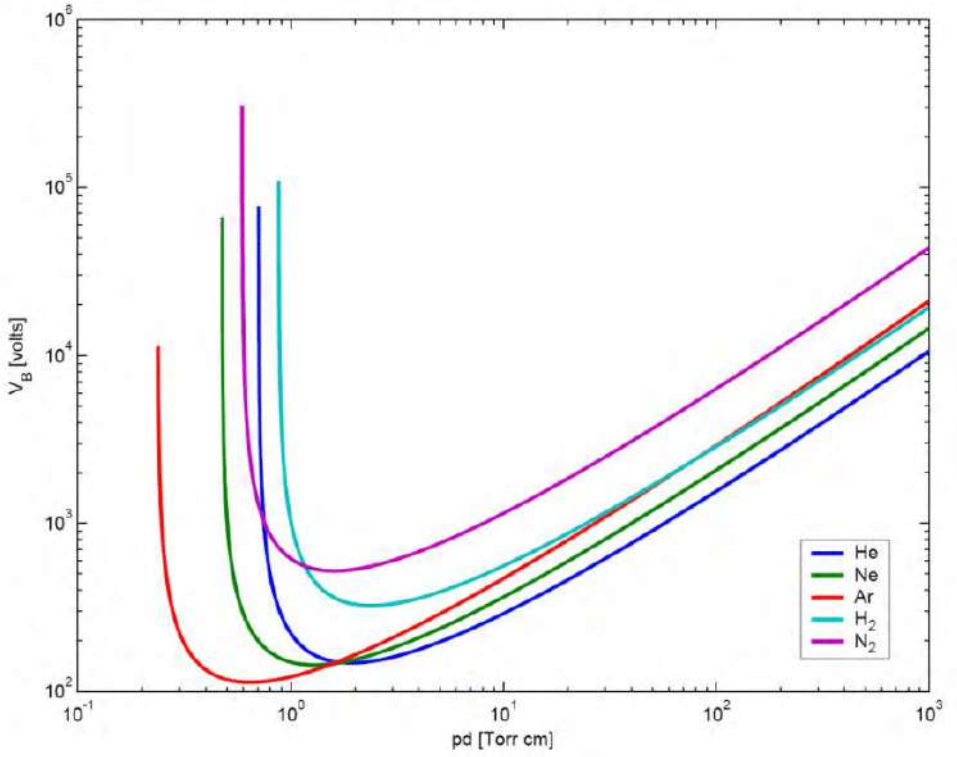

Figure 14: Paschen curves for different gases. The position of the minimum changes as a function of the gas, for noble gases the minimum shifts towards lower values of V_b and pd by increasing the atomic number [27].

Substrates produced at LNL are made of three different layers. The first one consists of a Ta backing of 99.9 % purity, the second one is a Ta layer of 99.99 % purity and the last

layer is made by TaN with Ta of 99.99 % purity. The Ta backing can be obtained by cutting a Ta foil with a laser beam technique. Tantalum is used as backing because of its capability to resist to an high amount of power given in a small area (it has an high temperature of fusion and an high thermal capacity) and because it does not introduce background contamination. Before creating the Ta and TaN layers the backing needs to be cleaned chemically by using acids like clorydric (HCl) or nitric (HNO_3) in order to remove contaminants and to obtain an homogeneous surface. Additional cleaning must be done with Argon plasma etching. During the sputtering process the sample must be cooled down by water.
The second layer is obtained by bombarding a tantalum target by Ar plasma ions to obtain a layer of pure material deposited on the backing. The gas injected into the chamber is ionized and the plasma ions are accelerated due to the potential difference between cathode and anode and hit the target surface at negative potential, transferring their kinetic energy to the molecular layers of Ta. Atoms expelled from the target deposit on the substrate. Then nitrogen is introduced in the sputtering chamber and it reacts with the metal of the target forming a chemical compound of TaN. This compound can be sputtered by the plasma ions and then attaches to the substrate. The amount of N gas must be accurately controlled, since if it is too low it would not be able to form molecules of TaN_x ($x<1$) and if it is too much molecules will form but the target would be "poisoned" by nitrogen and the sputtering rate would decrease (TaN has an higher binding energy than Ta alone).

Poisoning of the target is related to the very non-linear behaviour of some parameters, i.e. deposition and erosion rate, but also pressure and optical emission as a function of the reactive gas supply, in particular they exhibit an hysteresis effect [22]. This behaviour can be described by analyzing e.g. the deposition and erosion rates in Fig. 15. When Q_{tot} reaches the position corresponding to P_1, the erosion rate suddenly decreases to P_2, and then continues with a slow decrease. When decreasing the total gas supply instead, the erosion rate reaches the point P_3 and then increases rapidly up to point P_4. It is impossible to reach any point in the segment connecting the points P_3 and P_1. The separation width between increasing and decreasing behaviour denotes the hysteresis region width (shaded region between the P_1, P_2, P_3 and P_4 points).

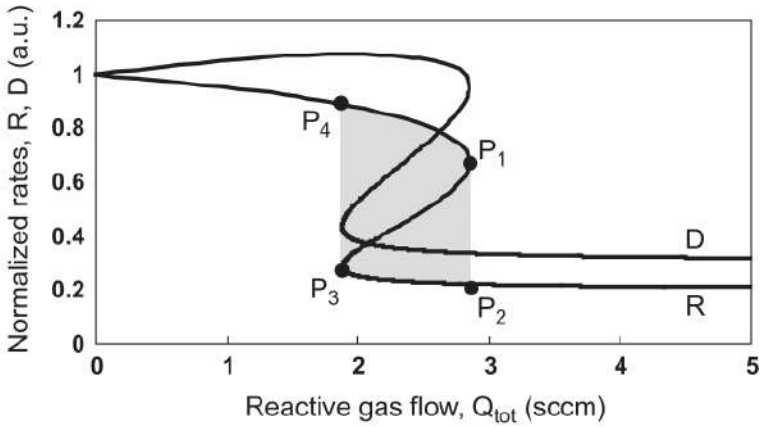

Figure 15: Calculated target erosion rate R and substrate deposition rate D vs. total supply rate of reactive gas, Q_{tot} [22].

The sputter erosion and deposition rates are linked to the pressure P of the reactive gas [22]. It is possible to get a relation of these two quantities with the partial pressure P, which do not show a hysteresis behaviour. Since it is difficult to control this quantity, the total reactive gas flow rate Q_{tot} is used as control parameter.

Two methods are used at LNL to control the level of poisoning of the target: one varies the

total gas flow rate Q_{tot} and measures the pressure behaviour inside the chamber. The other one consists of varying the level of the gas flow rate and to see the behaviour of the optical emission of the material, which has a characteristic wavelength at 265 nm for Ta, and around 500-600 nm for Ar. In particular the value of optical emission decreases by increasing the value of the gas flow Q_{tot} because of the target poisoning.

2.2 Ion implantation

Ion implantation consists into bombarding a surface of an element (e.g. Ta in the case of TaN targets) with an ion beam accelerated through a voltage difference [28, 31]. Ions lose their entire energy and are embedded into the substrate material: they can remain in a solid solution or form chemical bindings. Typically acceleration voltages used are around 50-250 keV for industrial applications, but they can also reach 10 MeV in research experiments [28].

When an ion penetrates the substrate elastic and inelastic collisions with the material take place [31]. Energy loss due to collisions can be divided into three contributions:

$$\frac{dE}{dx} = \left(\frac{dE}{dx}\right)_{nucl.} + \left(\frac{dE}{dx}\right)_{elect.} + \left(\frac{dE}{dx}\right)_{exch.}, \tag{20}$$

where the first term in the right hand side is the nuclear stopping power, that dominates at lower energies, while the second term is the electronic stopping power. The third term represents energy loss by charge exchange processes between ions and atoms of the substrate. After loosing all their energy, the incident particles stop in the substrate. The distance R_{tot} (or range) covered before stopping is specific of each ion and is given by:

$$R_{tot} = \int_0^{E_p} -\frac{dE}{(dE/dx)_{tot}}, \tag{21}$$

where E_p is the incident energy and $(dE/dx)_{tot}$ the total energy loss. Particle depth can also be represented by a distribution, the projected range R_p corresponds to its peak and represents the average depth of an ion, along the incident beam direction. The straggling along this mean value is defined by ΔR_p, which represents the spread of the ion path length [31].
The dose is defined as the integral over time of the ion beam current and it can be obtained by reading the number of counts N measured by a current integrator:

$$D = NS/qe. \tag{22}$$

D is the dose (or ion fluence, in atoms/cm^2), q the charge state of the ion and e the electric charge, S the scale at which the digital integrator is set (in units of C/cm^2). For high dose implantation (i.e. exceeding 10^{12} atoms/cm^2) effects like atomic mixing, sputtering, ion beam induced migration and chemical effects influence the state of the implanted material and the depth reached by the implanted ions [31]. When a beam of ions at high energy hits a layer of an impurity inside the substrate, mixing between impurity and host atoms occurs. This effect has a little influence on the projected range R_p, but modifies substantially the straggling ΔR_p. Furthermore, high doses favour sputtering of the superficial substrate atoms: this effect is more pronounced for heavier and high energetic projectiles and is inversely proportional to the atom's binding energy.

A Montecarlo simulation code SRIM-2013 [29] was used to simulate the transport of ^{14}N in tantalum. The output of the simulation provides the ^{14}N projected range R_p, the corresponding straggling ΔR_p, the sputtering yield S and the fraction of the backscattered nitrogen ions. The theoretical implanted profile as a function of depth is calculated independently from the SRIM

simulation as [30]:

$$n(x) = \frac{n_a(1 - BS)}{2S}\left[\mathrm{erf}\left(\frac{x - R_p + D_N(S/n_a)}{\sqrt{2}\Delta R_p}\right) - \mathrm{erf}\left(\frac{x - R_p}{\sqrt{2}\Delta R_p}\right)\right], \tag{23}$$

where x is the depth of the Ta layer, n(x) and n_a the implanted ion and substrate atomic density respectively, D_N is the nominal fluence, BS describes the number of backscattered ions. It is also possible to calculate the number of ions remaining in the substrate D_I (retained fluence):

$$D_I = \int_0^\infty n(x)dx. \tag{24}$$

Some implanted profiles are shown in Fig. 16 for different nominal fluences D_N using a proton beam of 40 keV on a Ta target. At lower doses the implantation profile resembles to a gaussian, while increasing this parameter the peak of the curve increases in width and shifts towards the surface. It saturates at a dose of $D_N = 6 \cdot 10^7$ atoms/cm^2, the one relative to the implanted target studied at LNGS on march 2023. Input parameters used for the calculation are presented in Tab. 2.

Energy (keV)	S (atoms/ion)	BS	R_p (Ang)	ΔR_p (Ang)
40	0.9098	0.2114	414	222

Table 2: Parameters used to calculate the ion implantation density.

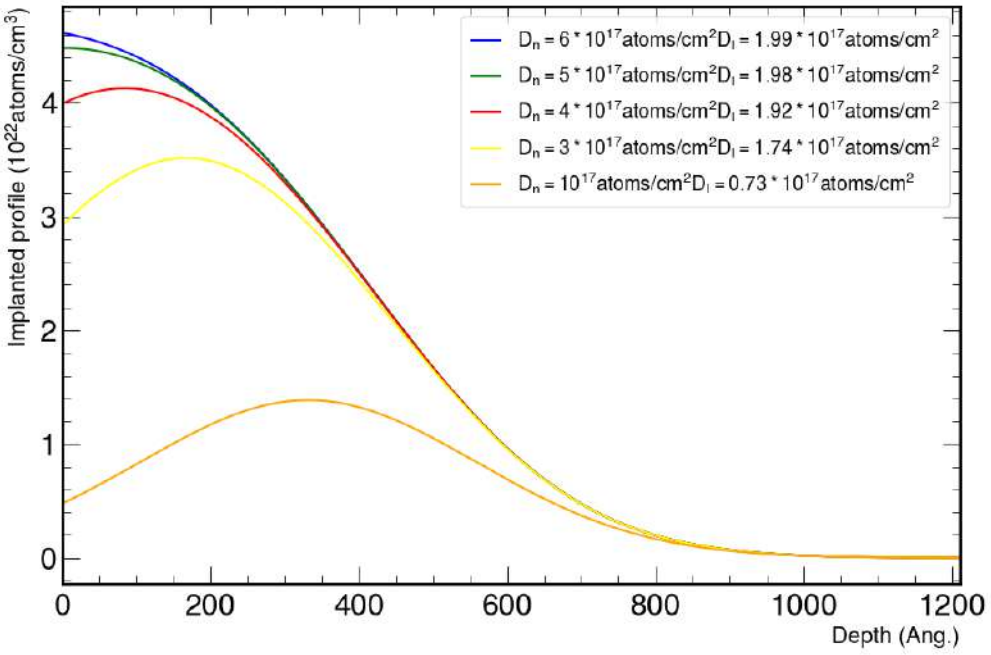

Figure 16: Implanted profile (implanted ion density) as a function of depth for different nominal doses D_N.

2.3 RBS analysis

Rutherford Backscattering (RBS) [32, 33] is a technique used to analyze the composition of a material. It is used to obtain targets thickness and atomic composition before sending them

to the LNGS laboratories for characterization. An ion beam at high energy (typically of the order of MeV) impinges on the sample and undergoes elastic Coulomb interactions with the electrons of the material. The chemical species of the target can be determined from the energy of the backscattered ions, since the peak position in the RBS spectra depends on the mass of the particle which is impacted.
The ratio between the incident ion energy E_1 and its initial energy E_0 is related to the kinematical factor K by:

$$\frac{E_1}{E_0} = K(M_1, M_2, \theta) \qquad K(M_1, M_2, \theta) = \left[\frac{\sqrt{M_2^2 - M_1^2 \sin(\theta)^2} + M_1 \cos(\theta)}{M_1 + M_2}\right]^2, \tag{25}$$

where M_1 and M_2 are the incident ion mass and the target mass respectively and θ is the incidence angle. The energy of the scattered ions is specific of the atom which is impacted and in particular higher target masses correspond to an higher energy of the scattered particle. If the target has a surface layer with lower mass, a peak will arise on the top of the continuum representing the target's spectrum. In Fig. 17 a schematic RBS spectrum for Ni and Si is shown. The above formula is valid only for ions impinging on the surface of the target material [33], while beam particles can penetrate the target and be backscattered in any direction inside the material.

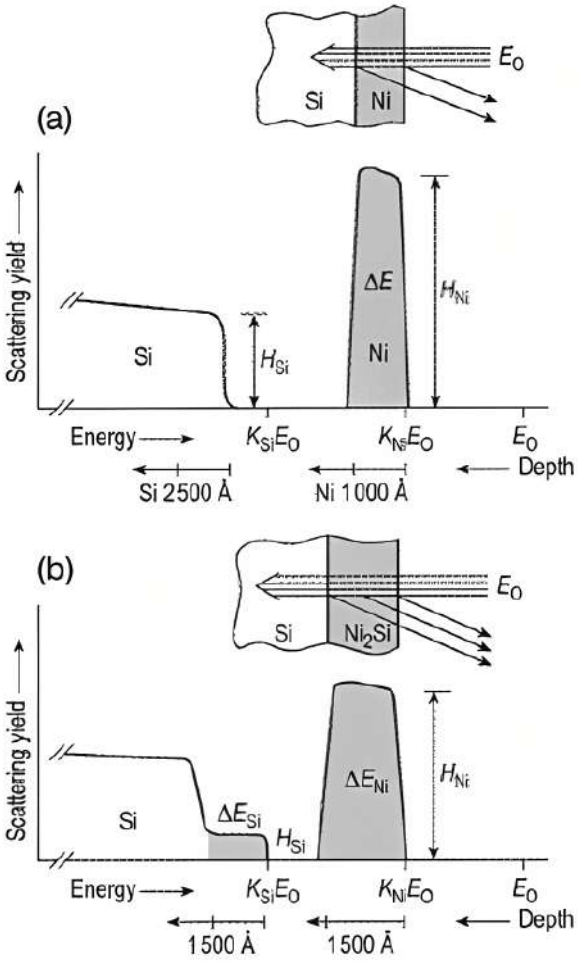

Figure 17: Schematic backscattering spectra for MeV He^+ ions incident on a 100 nm Ni film on Si (a) and after reaction to form Ni_2Si (b). The depth scales are indicated below the energy axes [33].

A more accurate analysis of the composition of the material is given by the cross section and the stopping power. Since the number of target particles depends on the cross section,

from the latter quantity we can derive how many particles are inside the material. For elastic collisions the cross section is given by the Rutherford formula:

$$\frac{\mathrm{d}\sigma}{\mathrm{d}\Omega} = \left(\frac{\mathrm{Z_1 Z_2 e^2}}{4\mathrm{E}}\right)^2 \frac{4}{(\sin(\theta))^4} \cdot \frac{(\sqrt{1-((\mathrm{M_1}/\mathrm{M_2})\sin(\theta))^2} + \cos(\theta))^2}{\sqrt{1-((\mathrm{M_1}/\mathrm{M_2})\sin(\theta))^2}}. \tag{26}$$

$\mathrm{M_1}$ and $\mathrm{M_2}$ are the projectile and target mass respectively, $\mathrm{Z_1}$ and $\mathrm{Z_2}$ their atomic numbers; E is the projectile energy immediately before the collision, θ the scattering angle and e the electric charge. In particular the cross section is proportional to the square of the target atomic number, showing a better sensitivity of this process to heavy elements. Deviations from the Rutherford formula can appear at high bombarding energies due to nuclear interactions and for inelastic collisions.
The energy lost by the beam in the target is mainly due to excitation or ionization of the atomic electrons of the material. This quantity is related in particular to the target thickness. The additional energy ΔE lost by a particle inside the target compared to one backscattered directly from the surface determines the thickness in energy of the peaks in the backscattering spectrum.
The height of the yield in the energy spectrum is determined by the thickness τ_i of the target and the number of scattering centers present.We have that:

$$\mathrm{H_i} = \frac{\sigma(\mathrm{E_i})\Omega\mathrm{Q}\mathrm{N}\tau_\mathrm{i}}{\cos(\theta)}, \tag{27}$$

where $\sigma(\mathrm{E_i})$ is the differential cross section averaged over the solid angle Ω, Q is the number of incident particles, N the atomic density of the sample analyzed and θ the angle between the normal to the target surface and the incident beam. In Fig. 18 is reported an RBS spectrum obtained for the TaN implanted target that was used at LNGS on march 2023; different energies of $^4\mathrm{He}^+$ bombarding particles were used. The presence of nitrogen can be seen from the double structure in the spectra: a layer of nitrogen has been deposited on the tantalum reducing the height at higher energies. From these spectra the percentage of nitrogen as a function of target depth can be deduced [30].

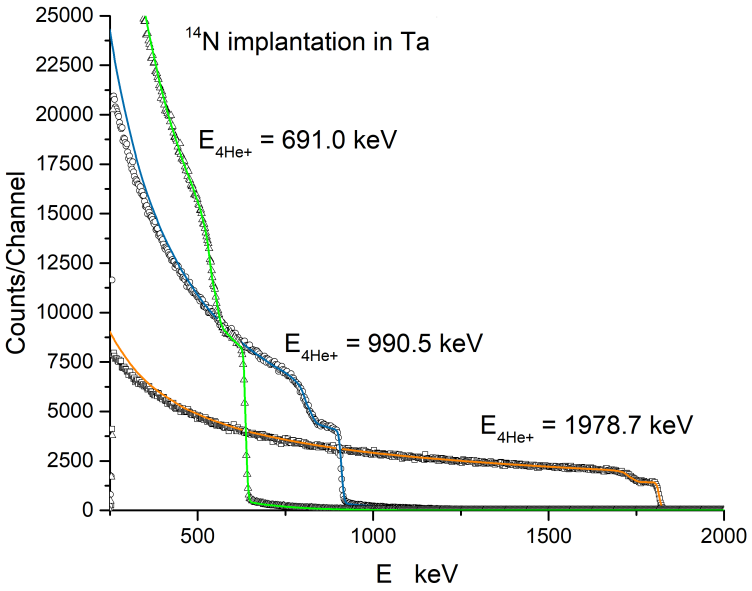

Figure 18: RBS Spectrum for different beam energies obtained for the implanted TaN target used at LNGS on March 2023.

3 Study of the targets at LNGS and estimation of the $\omega\gamma$ factor

This chapter focuses on the data analysis of the four TaN targets that will be used for the new measurement of ^{14}N(p,γ)^{15}O reaction at LNGS laboratories: one is an implanted target produced and analyzed with RBS at Lisbon, while the other three were produced at LNL laboratories with the sputtering technique. A week at the end of March 2023 was spent at LNGS for the data acquisition at the LUNA 400 accelerator.
At first the LUNA experiment is introduced, focusing on the reduction of the environmental background at LNGS and on the LUNA 400 and LUNA MV accelerators. Then the LUNA 400 experimental setup for target analysis is presented, followed by data analysis: yield calculations, energy and efficiency calibration are described. Contaminant analysis of the four targets and check for target stability is performed, including a fit to evaluate the target thickness in energy. Estimations of the $\omega\gamma$ factor for the E_r^{lab} = 278 keV resonance and of the branching ratios relative to the gamma rays emitted by the ^{15}O deexcitation are reported. A calculation was performed in order to reproduce the implanted target profile starting from Lisbon RBS analysis.

3.1 The LUNA experiment

Experimental data for the ^{14}N(p,γ)^{15}O reaction are taken at the LUNA 400 and LUNA MV accelerators installed at the Gran Sasso National Laboratories (LNGS). The natural shielding provided by the Gran Sasso mountain permits to reduce the cosmic flux by orders of magnitude [37].

The main sources of background radiation at LNGS are neutrons and gamma rays. Also high energetic muons can penetrate the rock depth and reach the underground facilities, but they are mostly stopped by the mountain rock [39], with a muon flux reduction of 6 orders of magnitude compared to the one at the Earth surface [37]. Neutrons with energies above 10 MeV come from cosmic muon particle showers induced by the interaction of muons with the atmosphere [38, 39]. Other sources of neutrons with energy below 10 MeV are due to (α,n) interactions on light elements like C, O, F, Na, Mg, Al and Si, where the α particles are emitted from the radioactive decays of the ^{238}U source present in the underground environment [38]. The flux of neutrons is reduced by 3 orders of magnitude by going in underground. It was measured in the LNGS interferometer tunnel with a NaI(Tl) detector obtaining a value between 1.5 x 10^6 s^{-1} cm^{-2} and 4.6 x 10^6 s^{-1} cm^{-2} [38].
The gamma ray background, also induced from muon induced particle showers, is strongly reduced by going in underground, as we can see in Fig. 19, which shows the gamma ray spectrum taken at LNGS compared to the one measured in Milan. Gamma rays below 3 MeV are still visible in the LNGS laboratories, due to radioactive isotopes present in the experimental room environment. The rock of the mountain at Gran Sasso and the concrete used in the laboratories contain radioactive sources of ^{238}U, ^{232}Th and ^{40}K. Gamma rays are emitted from the decay chains of these elements.

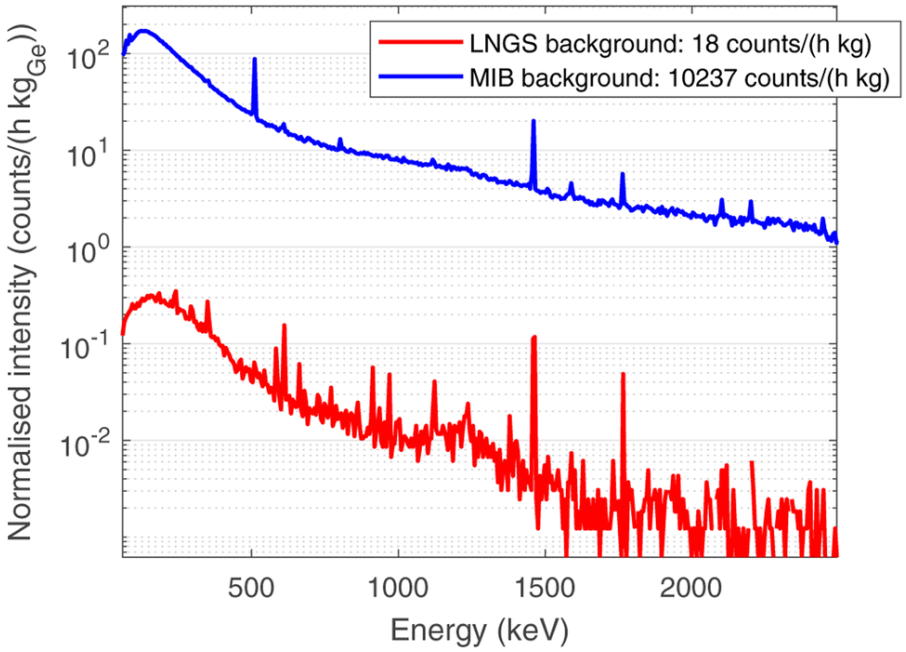

Figure 19: Comparison between the normalized background at LNGS (lower curve, red), with a depth of 3400 meter water equivalent, and the background at the radioactivity laboratory at the University of Milano-Bicocca MIB (upper curve, blue), at sea level. Spectra are normalized in time of measurement and mass of germanium in each detector [40].

The LUNA 400 accelerator, with a terminal voltage of 400 kV provides proton and helium beams that permitted to study most of the proton capture reactions involved in hydrogen burning. Beam stability is important to study reactions at astrophysical energies since the cross section drops exponentially. The LUNA proton beam energy is calibrated with 0.3 keV accuracy and a long term stability of 5 ev/h, with a 100 eV beam spread was found [41]. Two beam lines are available: one for solid targets and one for a windowless gas target.
The new LUNA MV accelerator (in Fig. 20 and 21) has been installed at the LNGS in 2023, and is capable to provide beams of H^+, $^4He^+$, $^{12}C^+$ and $^{12}C^{++}$ in the range 0.2-3.5 MV [36]. The accelerator has been constructed at High Voltage Engineering Europe (HVEE) in the Netherlands and installed in the Hall-B of the LNGS underground laboratories, with 80 cm thick concrete walls for neutron shielding. Carbon and helium burning reactions will be studied with this new facility, thanks to its stability and capability to reach sufficiently high energies, high beam intensity and to the background reduction thanks to the LNGS environment. The first reaction to be measured is the $^{14}N(p,\gamma)^{15}O$: the new machine will permit to cover a single dataset in the energy range from 2 MeV down to LUNA 400 energies, allowing the reduction of systematic errors down to 5 % [37]. Other reactions of interest that will be studied with this new accelerator in the next five years by the LUNA collaboration are the $^{13}C(\alpha,n)^{16}O$, the $^{22}Ne(\alpha,n)^{25}Mg$ and the $^{12}C + {}^{12}C$ one.

(a) Accelerator installed at LUNA MV.

(b) View of the beam lines at LUNA MV.

Figure 20

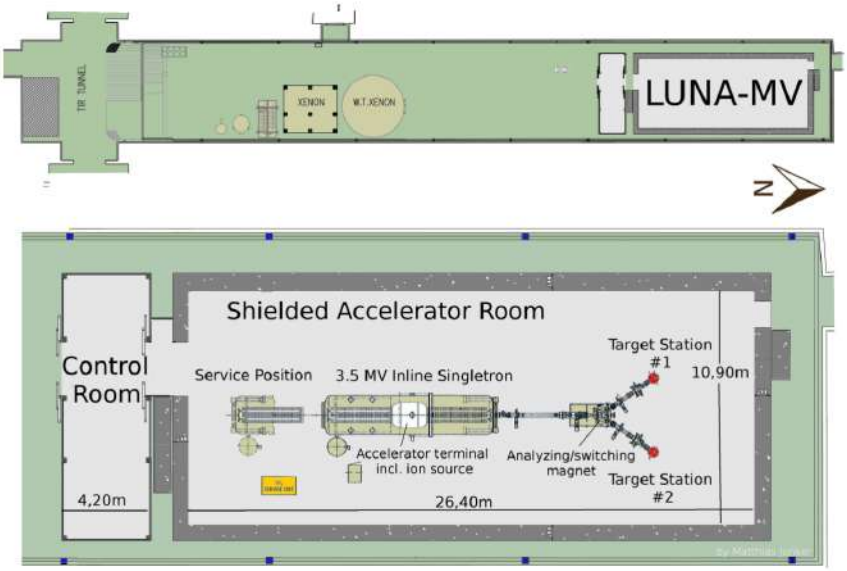

Figure 21: Location of the LUNA-MV installation with the 3.5 MV accelerator with two beam lines [36].

3.2 Experimental setup at LUNA 400

The experimental setup used to acquire data for the targets is composed by several parts, starting from the accelerator up to the target chamber, a scheme is reported in Fig. 22. The system is kept in vacuum by a primary and a turbomolecular pump, reaching pressures of 10^{-6} mBar.

The accelerator uses a plasma produced by a radiofrequency ion source that can provide He or proton beams (in this experiment protons are used). Ionized particles are then accelerated through a voltage difference with a maximum of 400 kV and sent to the beam lines [35]. Control panels permit varying terminal and probe voltage to modify the beam energy. One beam line is used for solid and another for gas targets. For the target tests the first one was used. A steerer is needed to focus the beam, and it is placed immediately after the accelerator. A series of magnets is placed along the beam line: one He magnet (HeI) is located immediately after the steerer and is used to deviate the beam along the gas target line. A quadrupole and another He magnet (HeII) are located along the solid target line after the first magnet. The HeII magnet serves to curve the beamline in the correct direction, while the quadrupole is used for the beam focalization.

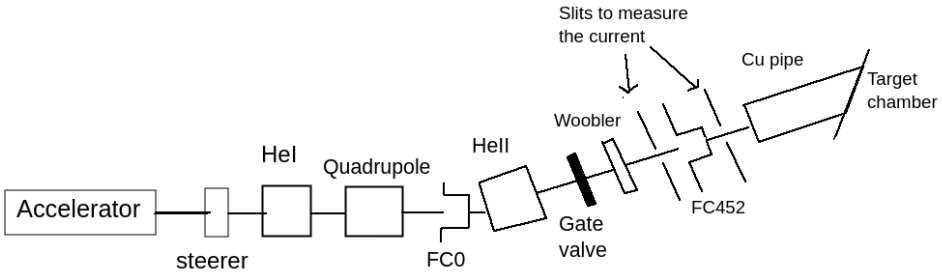

Figure 22: Scheme of LUNA 400 experimental apparatus.

A gate valve is placed immediately after the HeII magnet and is used to maintain the vacuum in the beam line towards the accelerator in case the pressure on the other side is not good enough. Wooblers are located after the gate valve and between the HeI magnet and the quadrupole. They are used to move the beam in different regions of the target in order not to damage it due to the high powers used.
A Cu tube cooled by liquid nitrogen acts as cold trap and is placed before and into the scattering chamber. The cold cathode trap at negative potential repels the secondary electrons and guarantees a correct measurement of the current. The scattering chamber, placed at the end of the beam line, is shielded by lead walls, contains the target placed in an apposite holder and is used for current measurement. In Fig. 23 is shown the LUNA 400 accelerator.

Figure 23: Accelerator installed at LUNA 400.

Faraday cups, the target chamber and slits are used to monitor the beam current: Faraday cup zero (FC0) is located between the quadrupole and the HeII magnet, another Faraday cup (FC452) is placed after the HeII magnet (it is not used). The scattering chamber serves to measure the beam current at the same place of the reaction (the current on the target is about

100-150 μA).
Solid targets used are an implanted TaN target produced at Lisbon and three sputtered targets produced at LNL. One is made with natural nitrogen, named '129'; the other two, named '130' and '131', are made of enriched nitrogen. Their thickness is reported in Tab. 3. Target holders B and C are used to mount the targets in the scattering chamber. A water flush is constantly provided to the targets during the experiment. CeBr and germanium detectors are used, data analysis is focused onto the latter one, placed at 55° with respect to the beam line in a close geometry configuration: the distance between the detector and the target in the scattering chamber is of the order of 2 cm.
The charge is read by a counter by integrating the current at the scattering chamber. Data for the charge, energy spectra and timestamps are saved for offline analysis.

	Δx (10^{18} atoms/cm^2)
implanted	0.89
'129'	2.54
'130'	2.48
'131'	1.24

Table 3: Thickness Δx of the targets used at LNGS.

3.3 Data analysis

3.3.1 Yield calculations

The experimental yield is an important quantity for targets characterization, in particular for the study of their profile through scans of the $E_r^{lab} = 278$ keV resonance. The yield can be obtained by dividing the number of reactions by the number of beam particles, which in practice is the number N_c of detected photons (relative to a specific nuclear transition) divided by the efficiency η of the detector, the angular correlation W, the branching ratio of the transition B and by the number of beam particles N_b (the efficiency, branching ratio and angular correlation are specific of the analyzed transition) [1]:

$$Y = \frac{N_R}{N_b} = \frac{N_c}{N_b \eta W B}. \tag{28}$$

In the data analysis we also use the yield calculated as the number of net counts under the energy peak of interest divided by the charge Q, given in μC:

$$Y = \frac{N_c}{Q}. \tag{29}$$

This equation has to be corrected by the charge factor e = $1.602 \cdot 10^{-19}$ C, the efficiency, angular correlation and branching ratio to obtain the first expression. The latter definition of the yield is used to obtain the efficiency versus energy curve using the ^{15}O transitions in section 3.3.3. Target profile analysis and fits to evaluate the target thickness in section 3.3.5 also use this definition. Since relative measurements are used, the above corrections are not needed for this part of analysis. The yield in eq. 28 is related to the cross section by [1]:

$$Y(E_p) = \int_{E_p - \Delta E}^{E_p} \frac{\sigma(E)}{\epsilon_{eff}(E)} dE, \tag{30}$$

where E_p is the beam energy, $\sigma(E)$ the cross section of the reaction and $\epsilon_{eff}(E)$ the effective stopping power, and the integral is performed over the thickness of the target ΔE. The effective

stopping power is given by [1]:

$$\epsilon_{\mathrm{eff}}(\mathrm{E}) = \epsilon_{\mathrm{x}} + \sum_{\mathrm{y}} \frac{\mathrm{n_y}}{\mathrm{n_x}} \epsilon_{\mathrm{y}}. \tag{31}$$

ϵ_{x} is the stopping power of the active species, i.e. the ones which participate to the reaction, such as ^{14}N for the reaction studied in this thesis. ϵ_{y} instead is the stopping power of the passive species, which do not participate to the reaction, while $\mathrm{n_x}$ and $\mathrm{n_y}$ are the atoms per cm^2 of active and inactive nuclei respectively.
If there is a narrow resonant state for which the cross section can be described by the Breit Wigner formula (Eq. 16 in section 1.4), we can substitute it in Eq. 30 to calculate the yield. Assuming also that the stopping power ϵ, the de Broglie wavelength λ and the partial widths Γ_{i} are independent of the energy over the entire resonance width, substituting the $\omega\gamma$ factor as in Eq. 19 in section 1.4, the yield that can be obtained from the integral of the cross section can be approximated by an arctangent function [1]:

$$\begin{aligned} \mathrm{Y}(\mathrm{E_p}) &= \frac{\lambda_{\mathrm{r}}^2}{2\pi} \frac{\omega\gamma}{\epsilon_{\mathrm{r}}} \frac{\Gamma}{2} \int_{\mathrm{E_p}-\Delta\mathrm{E}}^{\mathrm{E_p}} \frac{\mathrm{dE}}{[(\mathrm{E}-\mathrm{E_r})^2 + (\Gamma/2)^2]} \\ \mathrm{Y}(\mathrm{E_p}) &= \frac{\lambda_{\mathrm{r}}^2}{2\pi} \frac{\omega\gamma}{\epsilon_{\mathrm{r}}} \left[\arctan\left(\frac{\mathrm{E_p}-\mathrm{E_r}}{\Gamma/2} \right) - \arctan\left(\frac{\mathrm{E_p}-\mathrm{E_r}-\Delta\mathrm{E}}{\Gamma/2} \right) \right]. \end{aligned} \tag{32}$$

The de Broglie wavelength λ_{r} and the effective stopping power ϵ_{r} are calculated at the resonance energy. If the target thickness is much smaller than the resonance width, the shape of the yield curve is similar to the cross section one, while for thick targets ($\Gamma \ll \Delta\mathrm{E}$) the yield curve is dominated by the arctangent function and it is possible to reach a plateau performing a resonance scan. In Fig. 24 there is an example for a scan of the $\mathrm{E_r^{lab}} = 278$ keV resonance: the yield curve (calculated as the number of counts $\mathrm{N_c}$ divided by the charge Q in μC) is reported for the 1380 keV γ ray transition using the '129' sputtered target.

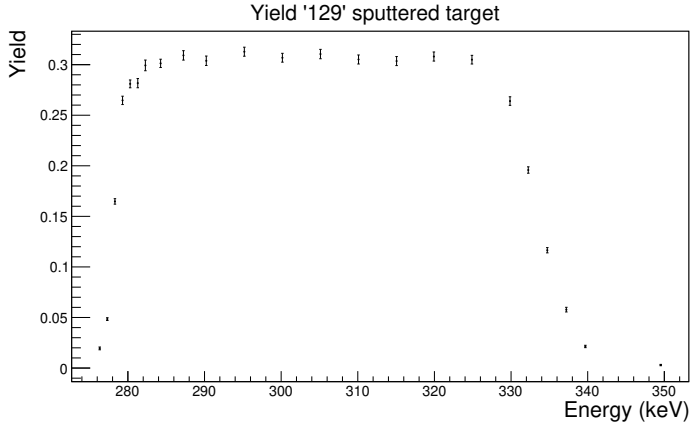

Figure 24: Plot of the yield relative to the 1380 keV γ ray transition for the '129' sputtered target (data taken on 28/03/23).

In the limit of an infinitely thick target ($\Delta\mathrm{E} \to \infty$) the yield is described by:

$$\mathrm{Y}_{\Delta\mathrm{E}\to\infty}(\mathrm{E_p}) = \frac{\lambda_{\mathrm{r}}^2}{2\pi} \frac{\omega\gamma}{\epsilon_{\mathrm{r}}} \left[\arctan\left(\frac{\mathrm{E_p}-\mathrm{E_r}}{\Gamma/2} \right) + \frac{\pi}{2} \right], \tag{33}$$

and the strength $\omega\gamma$ of the reaction can be obtained from the experimental yield calculated in

the plateau of the yield vs energy curve:

$$\omega\gamma = \frac{2\epsilon_r}{\lambda_r^2} Y_{max,\Delta E \to \infty}. \tag{34}$$

$Y_{max,\Delta E->\infty}$ is the yield in the plateau of the yield profile and the $\frac{\lambda_r^2}{2}$ factor is given by:

$$\frac{\lambda_r^2}{2} = 2\pi^2 \frac{\hbar^2}{2\mu_{01} E_r} = \left(\frac{M_0 + M_1}{M_1}\right)^2 \cdot \frac{4.125 \cdot 10^{-18}}{M_0 E_r^{lab}} \quad (cm^2), \tag{35}$$

where μ_{01} is the reduced mass of the entrance channel, M_0 (in amu) the projectile mass and M_1 (in amu) the target one, while E_r^{lab} (in eV) is the resonance energy in the laboratory system.

3.3.2 Energy calibration

Before starting with the data analysis for the targets, we proceed with the energy and efficiency calibration of the setup. In order to have a calibration in energy of the spectra acquired with the germanium detector we took the centroids of the peaks of the Co, Cs and Ba calibration sources, and of some of the background peaks in the long run taken between 27 and 28 March 2023 which are not affected by the Doppler shift. The ^{137}Cs source is responsible for a peak at E_γ = (661.657 ± 0.003) keV; the ^{60}Co one emits two gamma rays at E_γ = (1173.228 ± 0.003) keV and (1332.501 ± 0.005) keV; ^{133}Ba is responsible for four peaks at E_γ = (276.3989 ± 0.0012) keV, (302.8508 ± 0.0005) keV, (356.0129 ± 0.0007) keV and (383.8485 ± 0.0012) keV.
The (477.612 ± 0.003) keV peak corresponds to the decay of ^{7}Be into ^{7}Li through electron capture; the 511 keV one comes from the β decay of ^{15}O; the (609.321 ± 0.007) keV peak is related to the β decay of ^{214}Bi into ^{214}Po; the (1460.820 ± 0.005) keV one corresponds to the decay by electron capture of ^{40}K into ^{40}Ar; finally the (2614.511 ± 0.010) keV peak is due to the β decay of ^{208}Tl into ^{208}Pb. In Fig 25 are shown the peaks of the background used for the energy calibration.

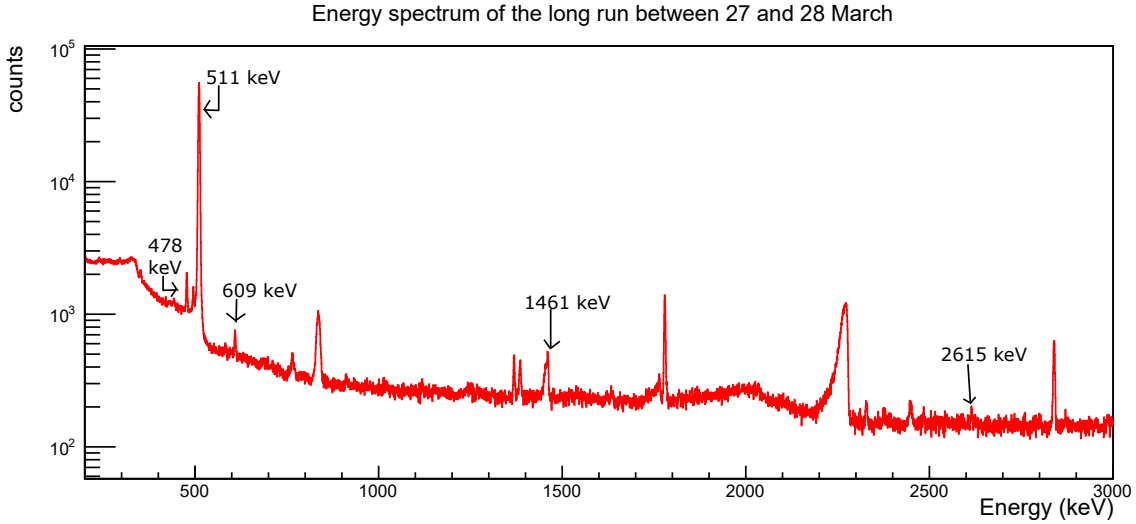

Figure 25: Energy spectrum of the long run taken between 27 and 28 March using the implanted target. Some of the peaks used for the energy calibration are indicated.

The detector is assumed to work in linear regime, so the correspondence between channels

and energies is expected to follow the linear relation:

$$E_\gamma = m \cdot N_{channel} + q. \tag{36}$$

To obtain the values of the parameters m and q, a linear fit of the pairs ($N_{channel}$, E_γ) is performed. The channel number $N_{channel}$ is obtained taking the mean of gaussian fits of all the peaks of interest. The mean values $N_{channel}$ are reported in table 4, while the calibration parameters are reported in table 5 together with the fit parameters. To obtain a good calibration in an energy range up to 10 MeV it is important to have a good correlation between the data, and this is confirmed by the correlation factor ρ.

E_γ (keV)	$N_{channel}$
276	407.59 ± 0.02
303	446.62 ± 0.01
356	525.136 ± 0.006
384	566.18 ± 0.01
662	975.92 ± 0.01
1173	1731.40 ± 0.02
1333	1966.60 ± 0.02
478	704.83 ± 0.07
511	754.264 ± 0.005
609	899.3 ± 0.2
1461	2151.9 ± 0.4
2615	3859.6 ± 0.7

Table 4: Centroids of the peaks in channels.

m (keV/ch)	q (keV)	ρ	t_{NC}	ν	α	CL
0.677471 ± 0.000006	0.174 ± 0.005	0.999	2655	10	3.169	0.05

Table 5: Parameters obtained from the fit: t_{NC} is the T-Student variable, α the threshold associated to the confidence level CL at which we reject the hypothesis of non linear correlation if $t_{NC} > \alpha$.

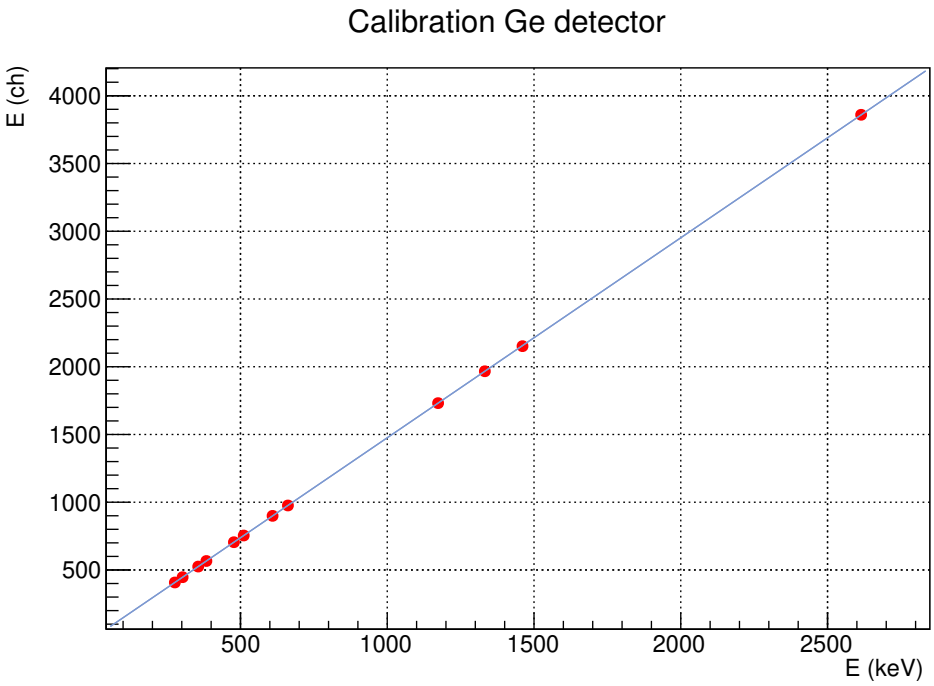

Figure 26: Energy calibration of the germanium detector.

3.3.3 Efficiency calibration

In this section full energy peak and total efficiency of the germanium detector are calculated as a function of the energy of the radiation source (i.e. the gamma ray that enters the detector). Total efficiency is a measure of how many gamma rays are seen by the detector regardless they deposit all their initial energy or only a part of it, while the peak efficiency only considers interactions which deposit all the initial energy of the source in the detector. Peak and total efficiencies are both function of the energy E of the incident gamma ray [3]. Here we use data from the calibration sources and from the ^{14}N(p,γ)^{15}O reaction to obtain the curves for the peak and total efficiency with two equivalent methods that will be compared. The radioactive sources used in the experiment are ^{137}Cs, ^{60}Co and ^{133}Ba. Their decay schemes are reported in Fig. 27 and 28, while their activities and half-lives are reported in Tab. 6.

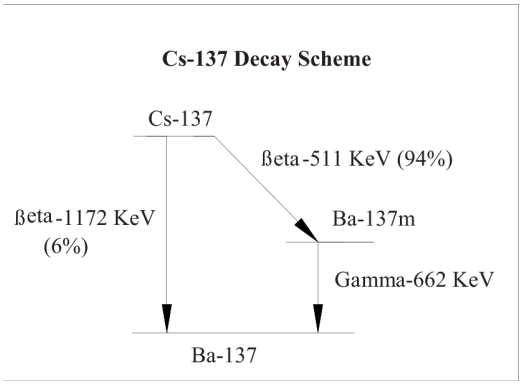

Figure 27: Level schemes of the decay of ^{137}Cs [42].

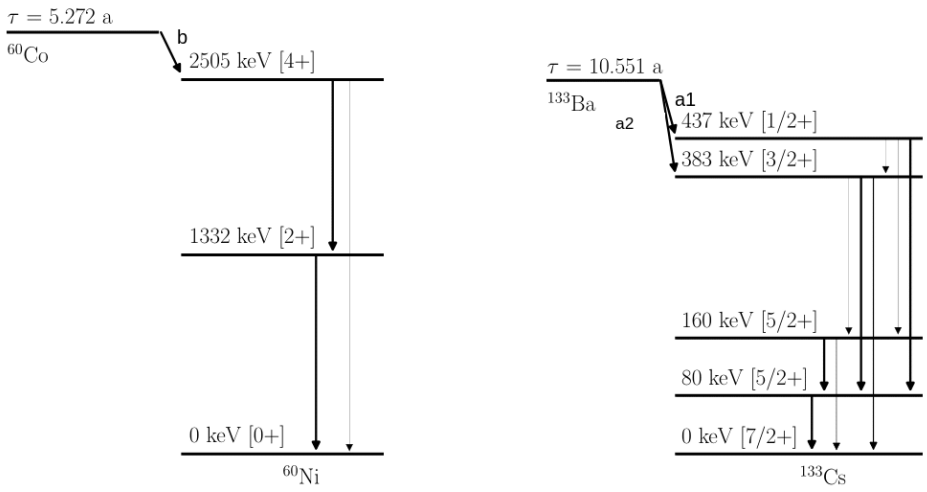

Figure 28: Level schemes of the decay of ^{60}Co and^{133}Ba.

Source	Activity (Bq)	$t_{1/2}$
^{133}Ba	22700 ± 700	10.551 ± 0.011 years
^{137}Cs	5530 ± 60	110000 ± 900 days
^{60}Co	3710 ± 30	1925.3 ± 0.4 days

Table 6: Activities of the sources measured on 27/03/23 for ^{133}Ba and on 31/03/23 for ^{137}Cs and ^{60}Co.

To evaluate the number of counts under the peak of interest we used a germanium detector and acquired data using a linear background subtraction system [2]. We calculated the net area under each peak as:

$$A = \sum_{i=L}^{U} C_i - \frac{n}{2}\left(\frac{\sum_{i=L-m_1}^{L-1} C_i}{m_1} + \frac{\sum_{i=U+1}^{U+m_2} C_i)}{m_2}\right), \tag{37}$$

where C_i are the counts in the i-th bin, L is the lower limit of the region of interest of the peak, U is the upper limit of the region of interest of the peak, n is the number of bins under the peak and m_1 and m_2 the number of bins on which the left and right background contributions are evaluated. Figure 29 shows graphically this notation.

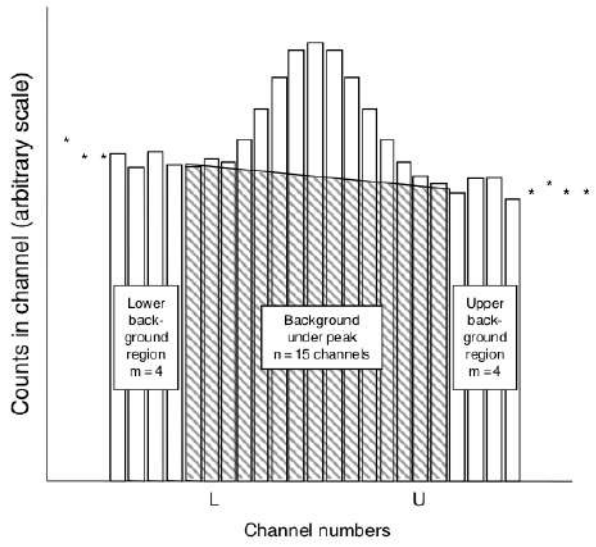

Figure 29: Background subtraction method used for the germanium detector [2].

The ratio between the counts under the peak N_c and the number of decays N_0 of these sources was estimated as:

$$\overline{Y} = \frac{N_c}{N_0} = \frac{N_c}{A(t)\Delta t}, \tag{38}$$

where A(t) is the activity of the source at the time of the experiment and Δt is the acquisition time. In Tab. 7 are reported the ratios $\overline{Y_i}$ for each γ ray peak.

Source	E_γ (keV)	$\overline{Y} = \frac{N_c}{\Delta t A(t)}$
^{133}Ba	276.3989 ± 0.0012	0.00164 ± 0.00005
^{133}Ba	302.8508 ± 0.0005	0.0041 ± 0.0001
^{133}Ba	356.0129 ± 0.0007	0.0137 ± 0.0004
^{133}Ba	383.8485 ± 0.0012	0.00193 ± 0.00006
^{137}Cs	661.657 ± 0.003	0.0185 ± 0.0002
^{60}Co	1173.228 ± 0.003	0.0160 ± 0.0002
^{60}Co	1332.501 ± 0.005	0.0149 ± 0.0002
^{60}Co	2505.729 ± 0.006	0.00032 ± 0.00002

Table 7: Ratios $\overline{Y} = N_c/(\Delta t\ A(t))$ for every gamma ray emitted from the source.

The full energy peak η^P for a monoenergetic source as ^{137}Cs can be estimated by dividing the ratio $\overline{Y}_{662}$ by its branching ratio b_{662}, i.e.:

$$\eta^P_{662} = \frac{\overline{Y}_{662}}{b_{662}}. \tag{39}$$

The two sources of ^{60}Co and ^{133}Ba instead display gamma ray decay cascades, and when the gamma rays are emitted in coincidence (i.e. in a time window narrower than the timing resolution of the detector), they can be partially or totally absorbed by it and give rise to the following effects that have to be corrected to have a good peak efficiency estimation:

- **Summing out**: one of the gamma rays is fully detected while the other may deposit some or all of its energy, giving rise to a decrease in the measured full energy peak.

- **Summing in**: the two gamma rays in the cascade ($E_{\gamma,1}$ and $E_{\gamma,2}$) are fully absorbed and contribute to the energy peak of the $E_\gamma = E_{\gamma,1} + E_{\gamma,2}$.

It is important to notice that the summing corrections are proportional to the solid angle, so they give a non negligible contribution only for small distances. In our case the efficiency measurements are done in a close geometry configuration (the Ge detector is placed immediately after the scattering chamber, at 2 cm from the target), so we must account for these effects. In particular we obtain the formulas for the $\overline{Y}_i$ of visible ^{60}Co and ^{133}Ba gamma peaks:

^{60}Co

$$\begin{aligned} \overline{Y}_{1173} &= (bBR_{1173,\gamma})\eta^P_{1173}(1-\eta^{tot}_{1332}BR_{1332,\gamma}) \\ \overline{Y}_{1332} &= (bBR_{1173,\gamma}BR_{1332,\gamma})\eta^P_{1332}(1-\eta^{tot}_{1173}) \\ \overline{Y}_{2505} &= (bBR_{2505,\gamma})\eta^P_{2505} + (bBR_{1173,\gamma}BR_{1332,\gamma})\eta^P_{1332}\eta^P_{1173} \end{aligned} \tag{40}$$

^{133}Ba

$$\begin{aligned} \overline{Y}_{276} &= (a_1BR_{276,\gamma})\eta^P_{276}(1-\eta^{tot}_{160}BR_{160,\gamma}-\eta^{tot}_{79}BR_{79,\gamma}-\eta^{tot}_{80}BR_{79,\gamma}BR_{80,\gamma}) \\ \overline{Y}_{302} &= (a_1BR_{53,\gamma}BR_{302,\gamma})\eta^P_{302}(1-\eta^{tot}_{53}-\eta^{tot}_{80}BR_{80,\gamma}) + (a_2BR_{302,\gamma})\eta^P_{302}(1-\eta^{tot}_{80}BR_{80,\gamma}) \\ \overline{Y}_{356} &= (a_1BR_{356,\gamma})\eta^P_{356}(1-\eta^{tot}_{80}BR_{80,\gamma}) \\ \overline{Y}_{383} &= (a_1BR_{53,\gamma}BR_{383,\gamma})\eta^P_{383}(1-\eta^{tot}_{53}) + (a_2BR_{383,\gamma})\eta^P_{383}, \end{aligned} \tag{41}$$

where η^P and η^{tot} are the peak and total efficiency respectively; b, a_1, a_2 are the probability of β decay of ^{60}Co to the ^{60}Ni 2505 keV excited state and of the β decays of ^{133}Ba on the excited levels of ^{133}Cs at E_x = 437 keV and 383 keV respectively. BR_γ are the probability of γ decays from the excited levels of the daughter nuclei.
To extend the efficiency curve to higher energies we use the resonance of the ^{14}N(p,γ)^{15}O reaction at E_r^{lab} = 278 keV. In Fig 30 are shown the gamma rays emitted by the ^{15}O deexcitation.

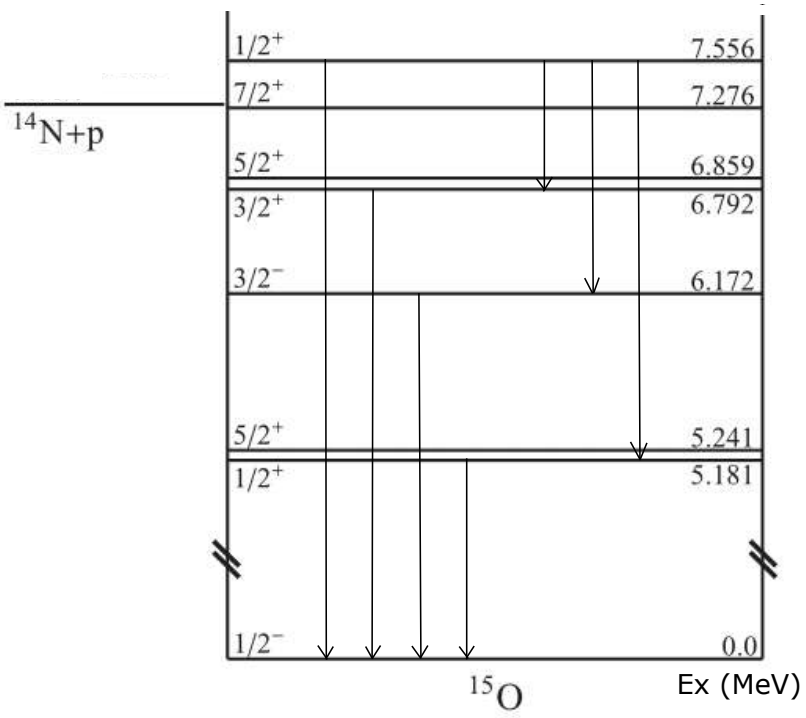

Figure 30: Level scheme of the ^{15}O nucleus and of the gamma rays emitted after populating the E_r^{lab} = 278 keV resonant state corresponding to the excited state at 7.556 MeV [17].

The ratio between the yields of the two gamma rays emitted in cascade due to the deexcitation of ^{15}O is related to the ratio between their peak efficiencies. Since the low energy gamma ray belongs to the energy region in which efficiency is constrained by the calibration sources, it is possible to extend the curve to higher energies by including in the fit also the yield ratios between a high energy and low energy gamma ray emitted in one to one scheme. Two equivalent methods can be used to obtain the efficiency curve: one is to fit the ratios between the yields of the two gamma rays emitted in the same cascade. Another way consists into directly fit the expressions for the yields of each transition introducing a parameter R related to the rate of the resonance, which is left free to vary in the fit procedure. The first method uses one half of data compared to the first one, since two yields are coupled in the same ratio, while the second one doubles the number of yields used but introduces another free parameter to be fitted. The theoretical values for the yields of the transitions are obtained as:

$$\begin{aligned}
Y_{763} &= R \cdot BR_{763,\gamma}\eta^{P}_{763}(1-\eta^{tot}_{6791}) \\
Y_{1380} &= R \cdot BR_{1380,\gamma}\eta^{P}_{1380}(1-\eta^{tot}_{6174}) \\
Y_{2373} &= R \cdot BR_{2373,\gamma}\eta^{P}_{2373}(1-\eta^{tot}_{5182}) \\
Y_{6791} &= R \cdot BR_{763,\gamma}\eta^{P}_{6791}(1-\eta^{tot}_{763}) \\
Y_{6174} &= R \cdot BR_{1380,\gamma}\eta^{P}_{6174}(1-\eta^{tot}_{1380}) \\
Y_{5182} &= R \cdot BR_{2373,\gamma}\eta^{P}_{5182}(1-\eta^{tot}_{2373}) \\
Y_{7554} &= R \cdot BR_{7554,\gamma}\eta^{P}_{7554} + R \cdot BR_{763}\eta^{P}_{6791}\eta^{P}_{763} + \\
&\quad R \cdot BR_{1380,\gamma}\eta^{P}_{6174}\eta^{P}_{1380} + R \cdot BR_{2373,\gamma}\eta^{P}_{5182}\eta^{P}_{2373}.
\end{aligned} \tag{42}$$

The experimental yield of each transition is obtained as the ratio of the net counts under the peak N_c by the charge Q given in μC, as in Eq. 29 in section 3.3.1. In Tab. 8 the yield values obtained on the plateau of the yield profile using the '129' target are reported for all the primary and secondary transitions.

E_γ (keV)	$Y=\frac{N_c}{Q}$ $(\mu C)^{-1}$
763.4 ± 1.7	0.160 ± 0.003
1380.1 ± 1.7	0.301 ± 0.004
2373 ± 1	0.059 ± 0.002
6791.4 ± 1.7	0.033 ± 0.001
6174.9 ± 1.7	0.092 ± 0.002
5182 ± 1	0.027 ± 0.003
7554.5 ± 0.4	0.0056 ± 0.0005

Table 8: Experimental yields for different transitions of ^{15}O from the sputtered target '129' taken on 28 March 2023 at E_p = 284 keV.

In order to obtain a curve of the efficiency in energy we fitted equations 39, 40, 41 with the ratios $\overline{Y}_i$ reported in Tab. 7. We also fitted the ratio of the primary to secondary transition yields of ^{15}O calculated from Eq. 42 with the ratio of the experimental ones given in table 8; in particular we fitted the following quantities:

$$\frac{Y_{763}}{Y_{6791}} \qquad \frac{Y_{1380}}{Y_{6174}} \qquad \frac{Y_{2373}}{Y_{5182}}. \tag{43}$$

Furthermore we included in the fit the estimation of the total efficiency of the ^{137}Cs source, calculated as the area A_{Cs} of the energy spectrum taken using only that source divided by the time of acquisition Δt and by the activity A(t):

$$\eta^{tot}_{662} = \frac{A_{Cs}}{\Delta t A(t)}. \tag{44}$$

This is an important reference point for the total efficiency and since ^{60}Co is a monoenergetic source the overall area of the energy spectrum gives an estimation of how many quanta of radiation emitted at 662 keV are recorded by the detector independently on the amount of initial energy deposited. Environmental background peaks in the energy spectrum can be neglected thanks to the high rate of emission of the ^{60}Co source. Total efficiency is also constrained by the summing corrections present in Eq. 40, 41 and 42. This curve is difficult to be calculated through this fitting procedure, since we have only one data point for the total efficiency and very weak constraints represented by the summing corrections.
The peak efficiency η^P and the total one η^{tot} are estimated using the following parametrizations [17]:

$$\begin{aligned} \eta^P &= A \cdot \exp(a + b \cdot \ln(E_\gamma) + c \cdot \ln(E_\gamma)^2) \\ \ln(\frac{\eta^P}{\eta^{tot}}) &= k_1 + k_2 \cdot \ln(E_\gamma) + k_3 \cdot \ln(E_\gamma)^2, \end{aligned} \tag{45}$$

where a, b, c, k_1, k_2, k_3 were left free to vary, while A = 0.0379, taken from previous efficiency curves obtained at LUNA to facilitate the minimization. The parameters obtained from the fit are presented in Tab. 9, while in Tab. 10 are shown the statistical parameters of the fit (the χ^2 value is calculated using both the experimental data uncertainties and the model ones). In Fig. 31 is plotted the curve of peak efficiency obtained with the parameters of the fit. The fit quality is good, with a reduced χ^2 value of 1.55 and a χ^2 value lower than the threshold associated to its corresponding confidence level, permitting to accept the hypothesis for the model described above. In Fig. 32 are reported the residuals obtained from the fit of the ratios $\overline{Y}_i$ of Eqs. 39, 40, 41 versus energy, the residuals of the ratios of the primary to secondary transition yields

relative to ^{15}O and the residual of the total efficiency for the ^{137}Cs source (Eq. 44).

a	b (keV^{-1})	c (keV^{-2})	k_1	k_2 (keV^{-1})	k_3 (keV^{-2})
-0.68 ± 0.02	-0.34 ± 0.02	-0.191 ± 0.009	-1.9 ± 0.2	-1.7 ± 0.3	7 ± 1

Table 9: Best parameters obtained from the fit.

χ^2	ν	χ^2/ν	α	CL
9.325	6	1.55	12.59	0.05

Table 10: Statistical parameters from the fit: ν are the degrees of freedom, α the threshold corresponding to the confidence level CL at which we accept the hypothesis for the model if $\chi^2 < \alpha$.

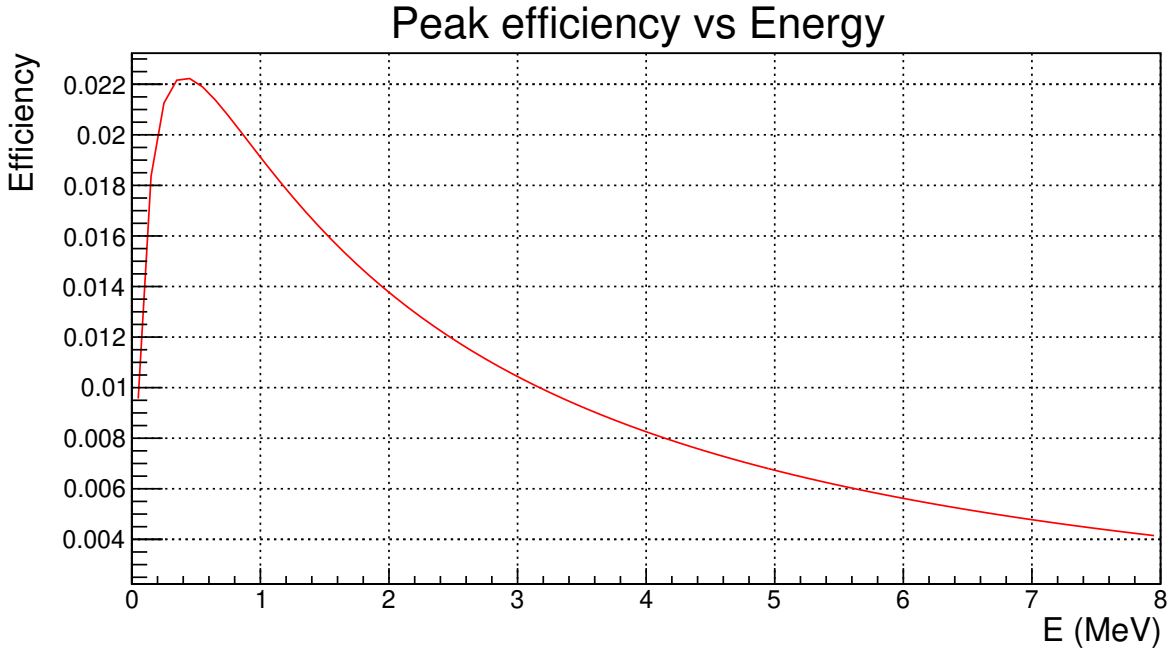

Figure 31: Peak efficiency obtained with best fit parameters.

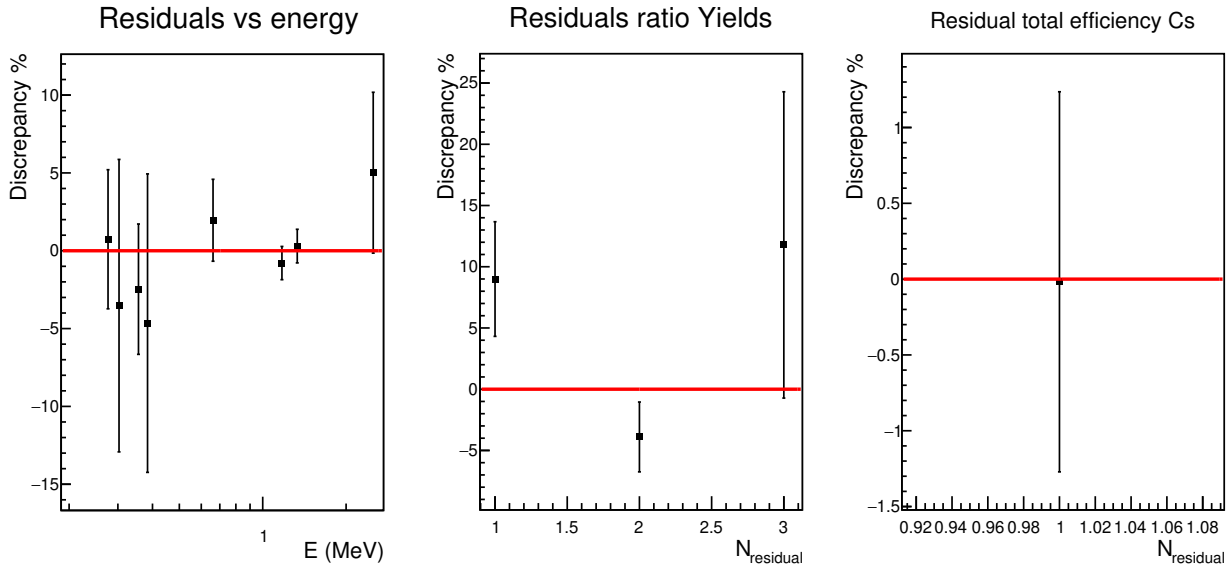

Figure 32: Residuals of the ratios $\overline{Y}_i$ versus energy, of the ratios of the primary to secondary transition yields relative to ^{15}O and of the total efficiency for the ^{137}Cs source.

The other way to obtain the efficiency curve is to fit together with the data from the Co, Cs and Ba sources the yields of the ^{15}O transitions instead of their ratios, except from the yield relative to the 7554.5 ± 0.4 keV peak. The fit is performed using the yields in a point of the plateau of the resonance for '129' and '130' targets, data are reported in Tab. 11 and 12. Fit parameters are reported in Tab. 13, together with the ones obtained by fitting the yield ratios for comparison. Statistical parameters obtained from the fits are displayed in Tab. 14.

E_γ (keV)	$Y = \frac{N_c}{Q}$ $(\mu C)^{-1}$ (28/03)	$Y = \frac{N_c}{Q}$ $(\mu C)^{-1}$ (29/03)
763.4 ± 1.7	0.160 ± 0.003	0.162 ± 0.004
1380.1 ± 1.7	0.301 ± 0.004	0.315 ± 0.005
2373 ± 1	0.059 ± 0.002	0.063 ± 0.002
6791.4 ± 1.7	0.033 ± 0.001	0.035 ± 0.002
6174.9 ± 1.7	0.092 ± 0.002	0.092 ± 0.003
5182 ± 1	0.027 ± 0.003	0.030 ± 0.004
7554.5 ± 0.4	0.0056 ± 0.0005	0.0056 ± 0.0007

Table 11: Experimental yields for different transitions of ^{15}O taken from the sputtered target '129' taken on 28 and 29 March 2023 at E_p = 284.3 keV and E_p = 285.3 keV respectively.

E_γ (keV)	$Y = \frac{N_c}{Q}$ $(\mu C)^{-1}$ (29/03)	$Y = \frac{N_c}{Q}$ $(\mu C)^{-1}$ (30/03)
763.4 ± 1.7	0.163 ± 0.004	0.150 ± 0.004
1380.1 ± 1.7	0.310 ± 0.005	0.297 ± 0.005
2373 ± 1	0.059 ± 0.002	0.060 ± 0.002
6791.4 ± 1.7	0.037 ± 0.002	0.032 ± 0.002
6174.9 ± 1.7	0.095 ± 0.003	0.090 ± 0.003
5182 ± 1	0.028 ± 0.004	0.036 ± 0.003
7554.5 ± 0.4	0.0043 ± 0.0006	0.0058 ± 0.0007

Table 12: Experimental yields for different transitions of ^{15}O taken from the sputtered target '130' taken on 29 and 30 March at E_p = 290.2 keV.

	a	b (keV^{-1})	c (keV^{-2})	k_1	k_2 (keV^{-1})	k_3 (keV^{-2})	R $(\mu C)^{-1}$
'129' (28/03)	-0.73 ± 0.01	-0.39 ± 0.02	-0.181 ± 0.009	-1.2 ± 0.2	-1.2 ± 0.4	4 ± 1	33.5 ± 0.7
'129' (29/03)	-0.73 ± 0.01	-0.39 ± 0.02	-0.188 ± 0.009	-1.1 ± 0.2	-1.4 ± 0.4	3.5 ± 0.9	34.8 ± 0.7
'130' (29/03)	-0.73 ± 0.01	-0.38 ± 0.02	-0.18 ± 0.01	-1.1 ± 0.2	-1.4 ± 0.4	3.5 ± 0.9	34.3 ± 0.7
'130' (30/03)	-0.73 ± 0.01	-0.38 ± 0.02	-0.181 ± 0.009	-1.2 ± 0.2	-1.3 ± 0.4	3.7 ± 0.9	32.7 ± 0.7
Ratios	-0.68 ± 0.02	-0.34 ± 0.02	-0.191 ± 0.009	-1.9 ± 0.2	-1.7 ± 0.3	7 ± 1	

Table 13: Best parameters obtained from the fit for '129' and '130' sputtered targets and by the method which fits the yield ratios.

	χ^2	ν	χ^2/ν	α	CL
'129' (28/03/23)	18.53	9	2.06	16.92	0.05
'129' (29/03/23)	14.95	9	1.66	16.92	0.05
'130' (29/03/23)	18.48	9	2.05	16.92	0.05
'130' (30/03/23)	18.15	9	2.02	16.92	0.05

Table 14: Statistical parameters from the fit: ν are the degrees of freedom, α the threshold corresponding to the confidence level CL at which we accept the hypothesis for the model if $\chi^2 < \alpha$.

In Fig. 33, are reported the residuals of the ratios $\overline{Y}_i$ for the Cs, Co and Ba sources and the yields of the transitions of the $^{14}N(p,\gamma)^{15}O$ as a function of the energy, while in Fig. 34 the residuals of the total efficiency of Cs are reported for the two sputtered targets and the three days of acquisition.

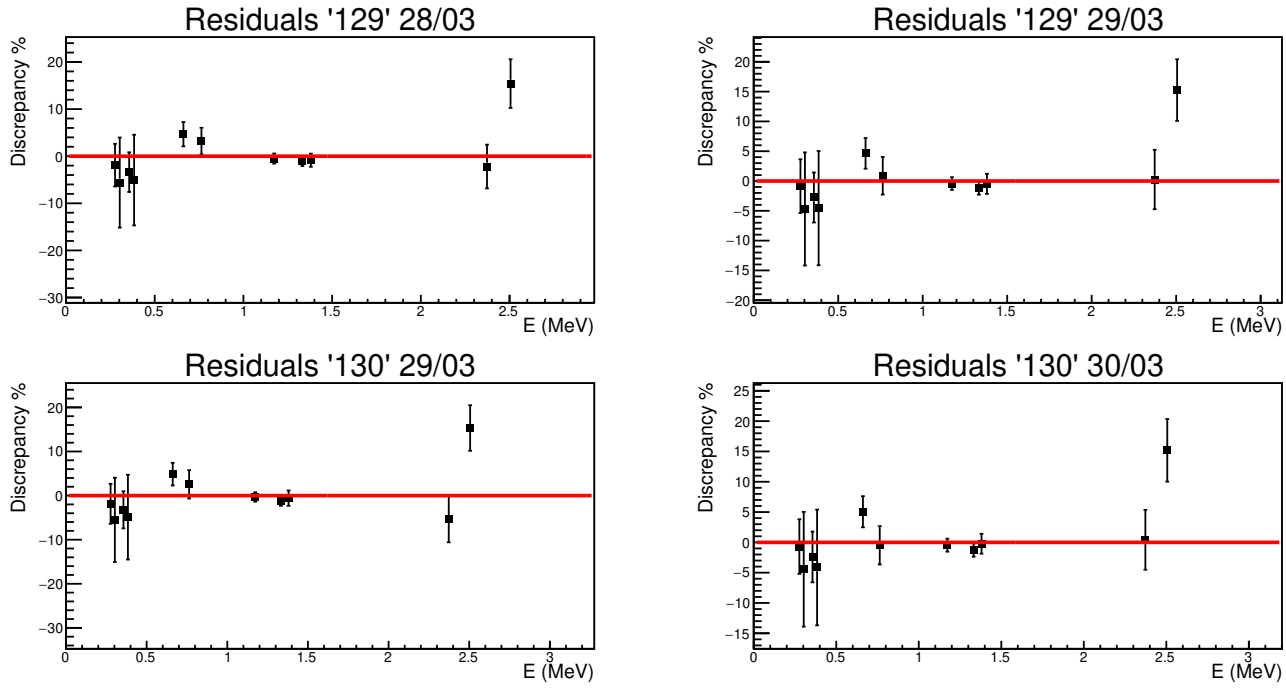

Figure 33: Residuals vs energy for '129' and '130' targets, data taken on 28, 29 and 30 March 2023.

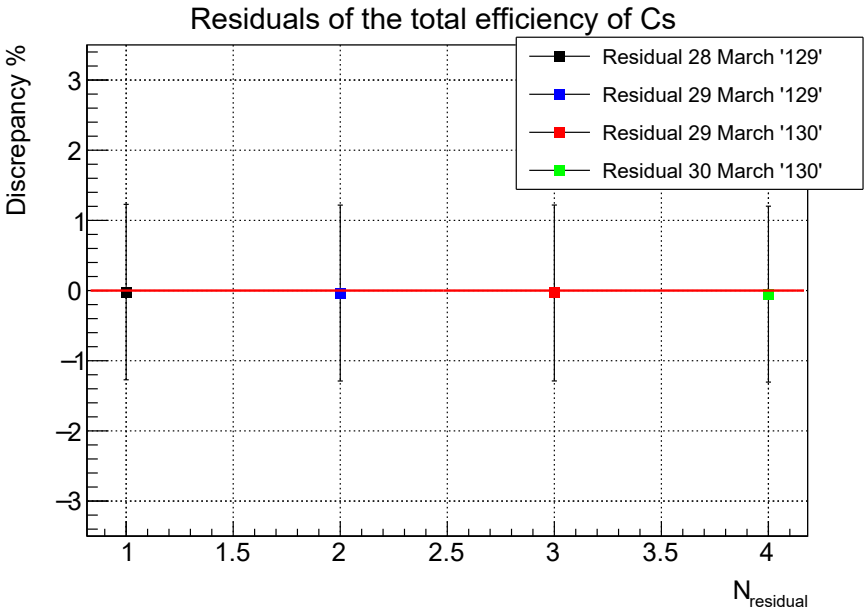

Figure 34: Residuals of the total efficiency of the ^{137}Cs source taken at different days for different targets.

There is a discrepancy between the curves obtained with the two methods described previously which derives from the difference between the parameters a, b, c, k_1, k_2 and k_3. The first three parameters, which describe the peak efficiency, differ by 5-10 % if we compare the ones obtained by fitting the ratio of the yields and the ones derived from the fit of the R parameter relative to the '129' sputtered target (with data taken on 28 March 2023). Higher differences are found for the k_1, k_2 and k_3 parameters used for the total efficiency calculation, but also experimental errors related to these parameters are quite high (of the order of 10-20 %). The curves obtained for the peak efficiency from the two methods are reported in Fig. 35, together with the discrepancy between the one obtained from the yield ratios and the one that fits the R parameter using '129' target with data taken on 28/03/23. The difference between the two curves is at maximum 5%, this could be due to systematics in the modeling of equations in the two approaches and in the capability of MINUIT in minimizing the χ^2 with "R" parameter. Since other efficiency systematics are of the same order we leave further investigation beyond the scope of the present thesis.

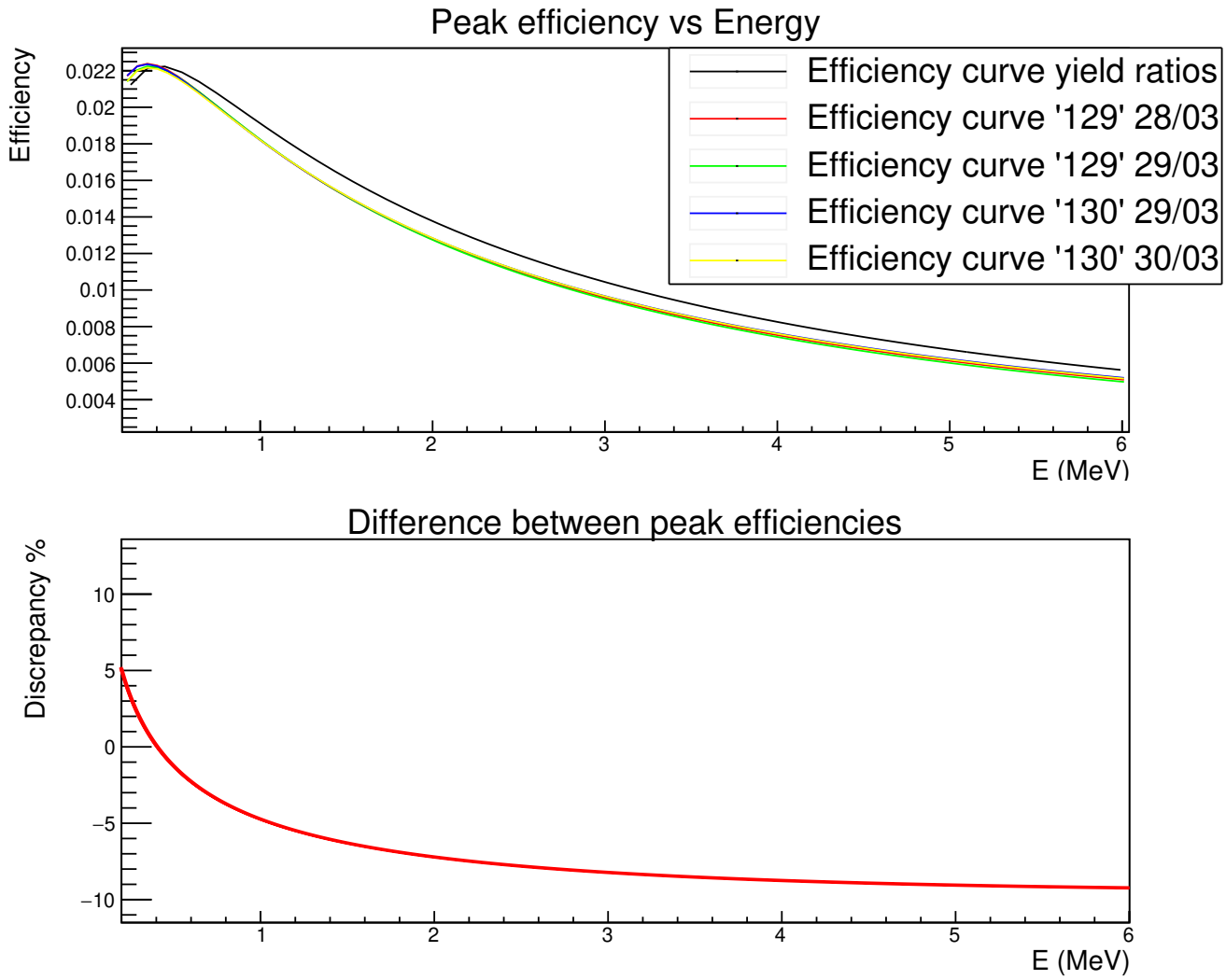

Figure 35: Above: peak efficiency curves obtained from the fit of the yield ratios (black curve), and from the fit of the R parameter using '129' and '130' sputtered targets (colored lines). Below: difference between the efficiency curve obtained with the method that fits the yield ratios and the one which uses the R parameter (using '129' target with data taken on 28/03/23).

3.3.4 Contaminants analysis

Analysis of the possible sources of target contamination is fundamental, since they can introduce unwanted peaks in the energy spectra, covering the gamma ray peaks of interest. Contaminants present in the targets studied are ^{19}F and ^{15}N, but also other sources like carbon and silicon are visible. The peaks in the energy range below 3 MeV are due to the environmental background (Tl, Bi, Ac, Be, K). The energy spectrum for the long run taken in the night between 28 and 29 march is shown in Fig. 36 (the peak at 8020 keV represents the pulser).

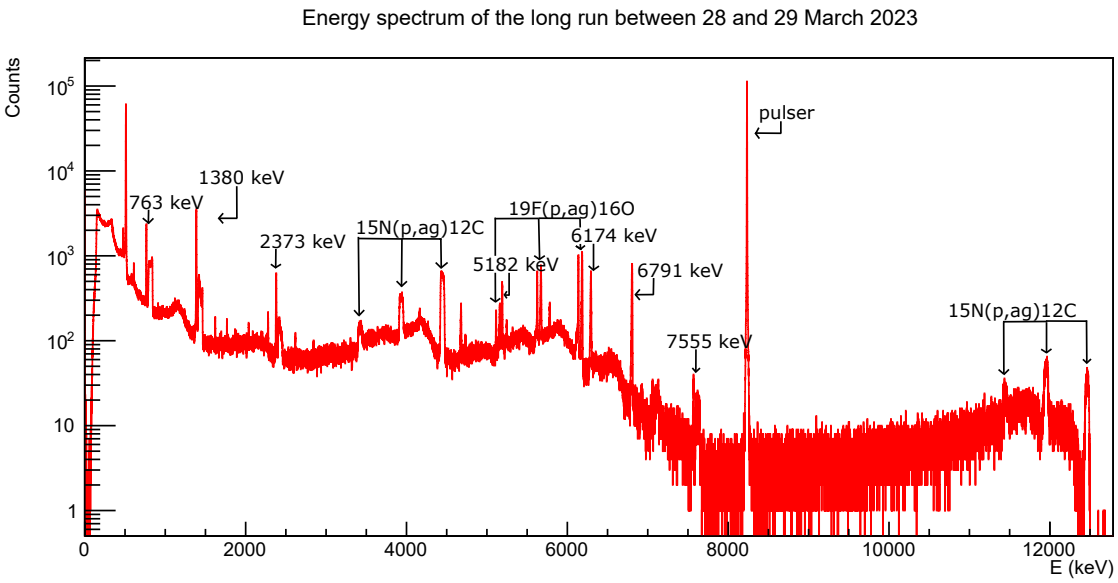

Figure 36: Energy spectrum of the long run between 28 and 29 March 2023 taken using the '129' target. The primary and secondary transitions of ^{15}O and the contamination peaks from ^{15}N(p,$\alpha\gamma$)^{12}C and ^{19}F(p,$\alpha\gamma$)^{16}O together with their single and double escape peaks are visible.

The contamination from fluorine can be clearly seen from the (6128.63 $\pm$ 0.04) keV peak (and by its single and double escape peaks) in the energy spectrum and through the resonance scan at E_r^{lab} = 340 keV: this is due to the ^{19}F(p,$\alpha\gamma$)^{16}O reaction. This contaminant is particularly problematic, expecially in the energy region between 220 keV and 390 keV, where the yield of the ^{14}N(p,γ)^{15}O drops by more than three orders of magnitude [4]. The cross section for this contaminant reaction is several orders of magnitude larger than other (p,γ) reactions [4] and introduces background in the energy region between 5 and 6 MeV, where ^{15}O gamma ray transitions are present. The resonance scans for the implanted, '129' and '131' targets are reported in Fig. 37: the implanted target is uniformly contaminated while the '129' one has a strong surface level of fluorine; the '131' target instead is clean up to the backing.

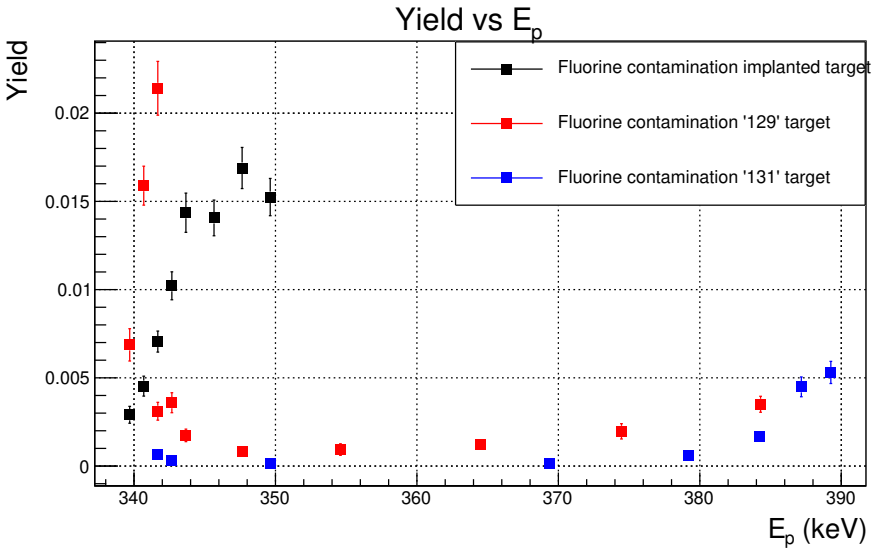

Figure 37: Scan of the 340 keV resonance for the implanted, '129' and '131' targets. Contamination of the implanted target is uniform, showing a slight increase of the yield towards energies higher than 340 keV. The '129' target shows a strong surface contamination, represented by the high yield value at 340 keV compared to higher energies. The '131' target instead is clean up to the backing, showing a slight increase of the yield at 390 keV.

Another contaminant present only in the sputtered targets is the ^{15}N, responsible for two peaks at 12450 keV and 4439 keV due to the ^{15}N(p,$\alpha\gamma$)^{12}C reaction.
The level of ^{15}N in the natural sputtered target, i.e. '129' was compared with the one in the enriched targets '130' and '131'; for this purpose we used the long runs taken during the nights at E_p = 360 keV.
For each target the yield in number of reactions per beam particle[2] under the 12450 keV peak was summed to the ones of its single and double escape peaks (if seen in the energy spectrum). In Tab. 15 we report the ratio between the yield calculated for the natural sputtered target and the one for the enriched target considered. It can be seen that in the enriched targets there is a reduction of two orders of magnitude in the level of ^{15}N contamination.

	$Y_{^{15}N,natural}/Y_{^{15}N,enriched}$
'129' vs '130'	290 ± 70
'129' vs '131'	290 ± 60

Table 15: Ratio between the yield of the 12450 keV transition of the natural sputtered target and the yield of the enriched one.

Other gamma ray peaks are related to the environmental background and come from electron captures of ^{7}Be and ^{40}K, (the latter one is visible only for the implanted target), and β decays of ^{208}Tl, ^{214}Bi, ^{212}Bi, ^{228}Ac (the latter two are visible only in the sputtered ones). In all the targets it is possible to see the contamination from the reaction ^{12}C(p,γ)^{13}N, while the implanted one also shows contamination from ^{27}Al(p,γ)^{28}Si and ^{16}O(p,γ)^{17}F. Also β^+ decays from ^{15}O and ^{13}N can be seen. In Tab. 16 are reported the areas under the peaks of the main contaminants of the implanted, '129', '130' and '131' targets respectively [3].

[2]Calculated using the efficiency obtained with the method that fits the yield ratios.
[3]Nominal energy values with the associated errors are taken from https://www.nndc.bnl.gov/nudat3/, while the value for the peak relative to the ^{12}C(p,γ)^{13}N reaction is given by the calibration.

	implanted	'129'	'130'	'131'	
Energy (keV)	Area $\cdot 10^2$	Area $\cdot 10^2$	Area $\cdot 10^2$	Area $\cdot 10^2$	contaminant
495.32 ± 0.10	34 ± 2				^{16}O(p,γ)^{17}F
511	3680 ± 6	4102 ± 7	4022 ± 7	1491 ± 4	^{15}O, ^{13}N (β^+)
1778.969 ± 0.011	75 ± 1				^{27}Al(p,γ)^{28}Si
2273	332 ± 2	12.6 ± 0.7	8.3 ± 0.5	8.9 ± 0.5	^{12}C(p,γ)^{13}N
3417		42 ± 3			d.e ^{15}N(p,$\alpha\gamma$)^{12}C
3928		139 ± 2			s.e ^{15}N(p,$\alpha\gamma$)^{12}C
4439		370 ± 2	9 ± 1	5.3 ± 0.7	^{15}N(p,$\alpha\gamma$)^{12}C
5106.63	257 ± 2	16.3 ± 0.7	4.3 ± 0.5	3.9 ± 0.3	d.e. ^{19}F(p,$\alpha\gamma$)^{16}O
5617.63	878 ± 4	56 ± 1	11.3 ± 0.6	12.2 ± 0.5	s.e. ^{19}F(p,$\alpha\gamma$)^{16}O
6128.63 ± 0.04	1318 ± 4	89 ± 1	18.5 ± 0.7	20.5 ± 0.6	^{19}F(p,$\alpha\gamma$)^{16}O
11428		7.8 ± 0.6			d.e. ^{15}N(p,$\alpha\gamma$)^{16}O
11939		29.3 ± 0.8			s.e. ^{15}N(p,$\alpha\gamma$)^{16}O
12450		24.1 ± 0.5	0.27 ± 0.06	0.27 ± 0.05	^{15}N(p,$\alpha\gamma$)^{16}O

Table 16: Area under the main contaminant peaks for the long run relative to the implanted, '129', '130' and '131' targets. The notation 's.e.' and 'd.e.' stands for 'single escape' and 'double escape' respectively.

3.3.5 Target stability check and estimation of the thickness ΔE

In this section we analyze the profile of the targets to see if they remain stable after a long period of irradiation, then we estimate their thickness in energy through a fit of the yield curve, and compare the value obtained with the nominal one given by RBS analysis. In order to check the stability of the targets over a long period of beam time we repeated the resonance scans at $E_r^{lab} = 278$ keV two times: before and after a long run lasting a night, accumulating a charge of about 10 C for each run. The yield (here calculated as the net counts under the peaks of the transition considered divided by the charge in μC) is reported in Figs. 38, 39, 40, 41 for all the primary and secondary transitions. The yield profile seems to remain stable after the long run.

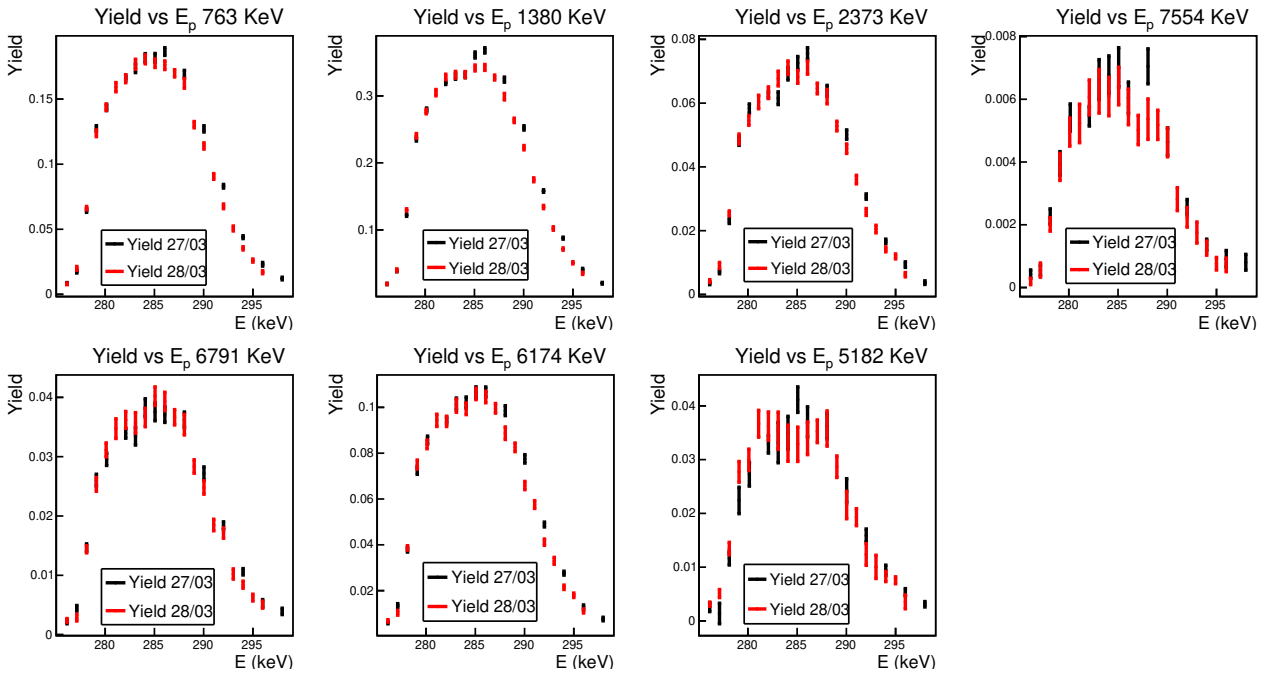

Figure 38: Scan of the implanted target for different transitions: black points were taken on 27 March, red points on 28 March.

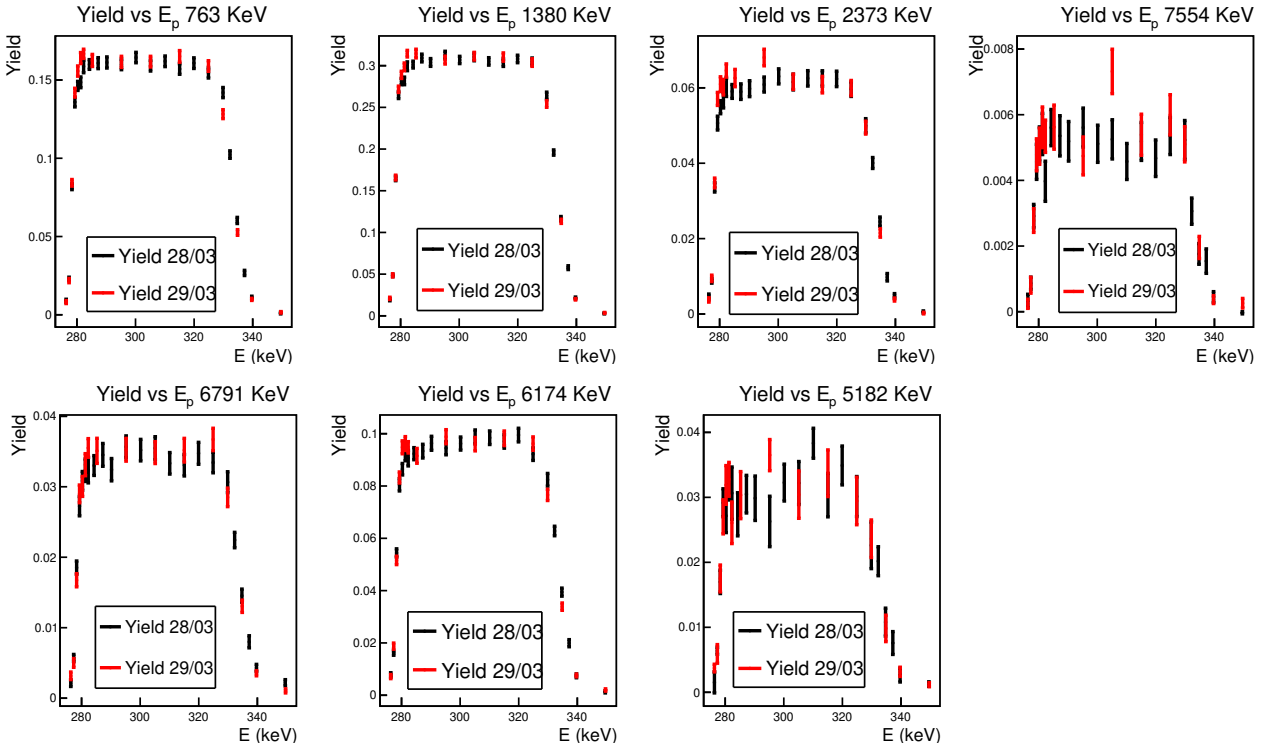

Figure 39: Scan of the sputtered target '129' for different transitions: black points were taken on 28 March, red points on 29 March.

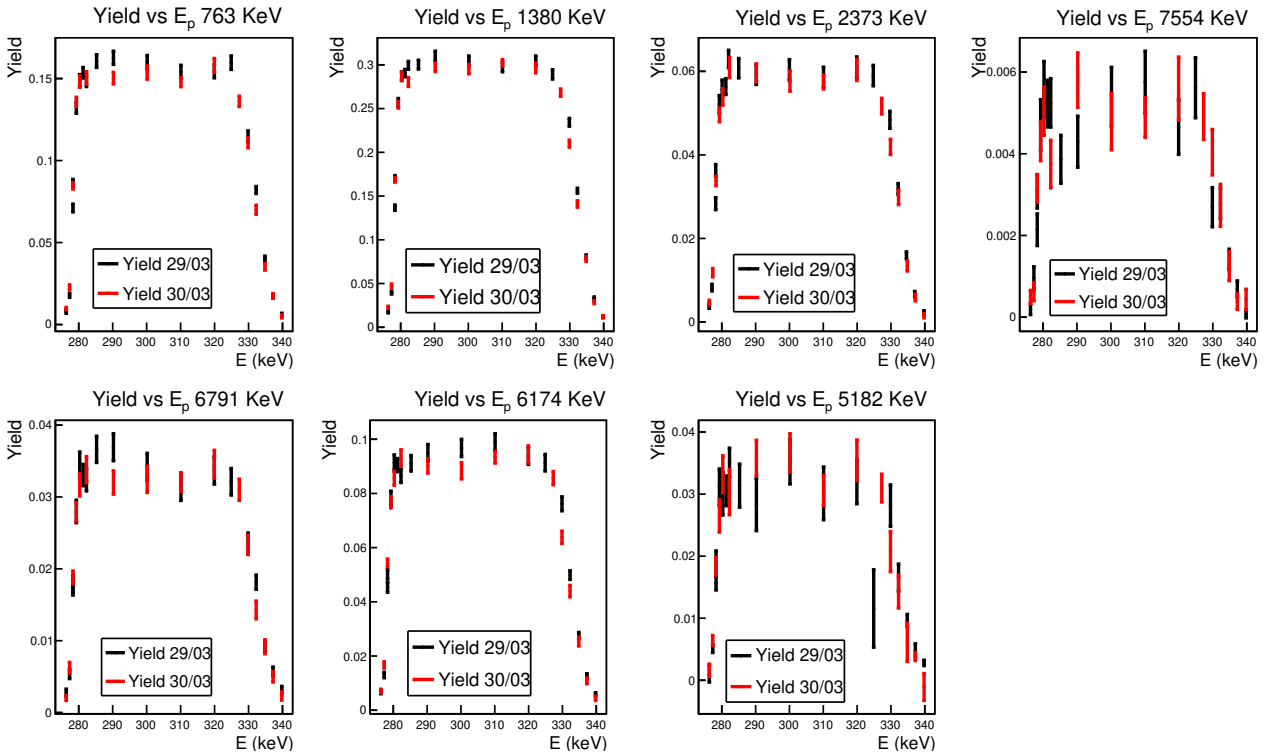

Figure 40: Scan of the sputtered target '130' for different transitions: black points were taken on 29 March, red points on 30 March.

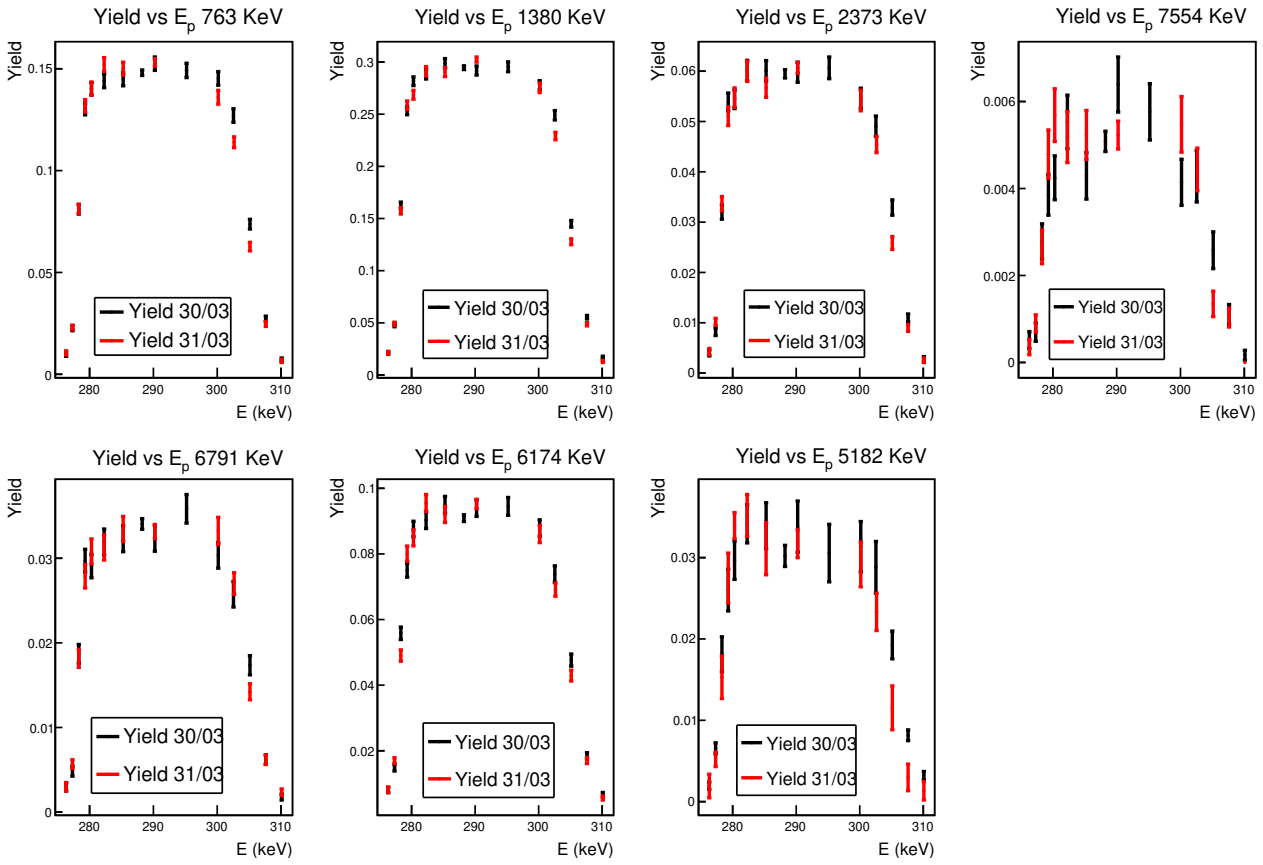

Figure 41: Scan of the sputtered target '131' for different transitions: black points were taken on 30 March, red points on 31 March.

Furthermore, the estimation of the target thickness in energy was performed for all the sputtered targets: data were fitted with a double arctangent function:

$$Y(E) = a \cdot \text{atan}(b(E + c)) + d - e \cdot \text{atan}(f(E + g)). \tag{46}$$

The fit was performed using the yield relative to the 1380 keV transition calculated as in equation 29 in section 3.3.1. The widths Γ_1 and Γ_2 for the rising and falling edge of the curve and the target thickness in energy ΔE are given by:

$$\Gamma_1 = \frac{2}{b} \qquad \Gamma_2 = \frac{2}{f} \qquad \Delta E = g - c. \tag{47}$$

The fits are reported together with the residuals in Fig. 42, 43, and 44 while the widths Γ_1 and Γ_2 are reported together with the thickness in energy ΔE and the expected values ΔE_{th} obtained from RBS analysis in Tab. 17 [4]. The Γ_1 values are near the one given for the resonance $\Gamma^{lab} = (0.96 \pm 0.05)$ keV [17]. The widths obtained from the fit are 2-3 keV higher than the expected ones for '129' and '130' targets, for the '131' target instead the fitted width is about 0.5 keV higher than the expected one. The thicknesses obtained from the fit procedure are more reliable than the estimations obtained from RBS analysis, since they come from data acquired directly in the laboratory. The errors associated to this method are probably underestimated, and the uncertainties associated to these measurements have to be estimated during the next data acquisitions.

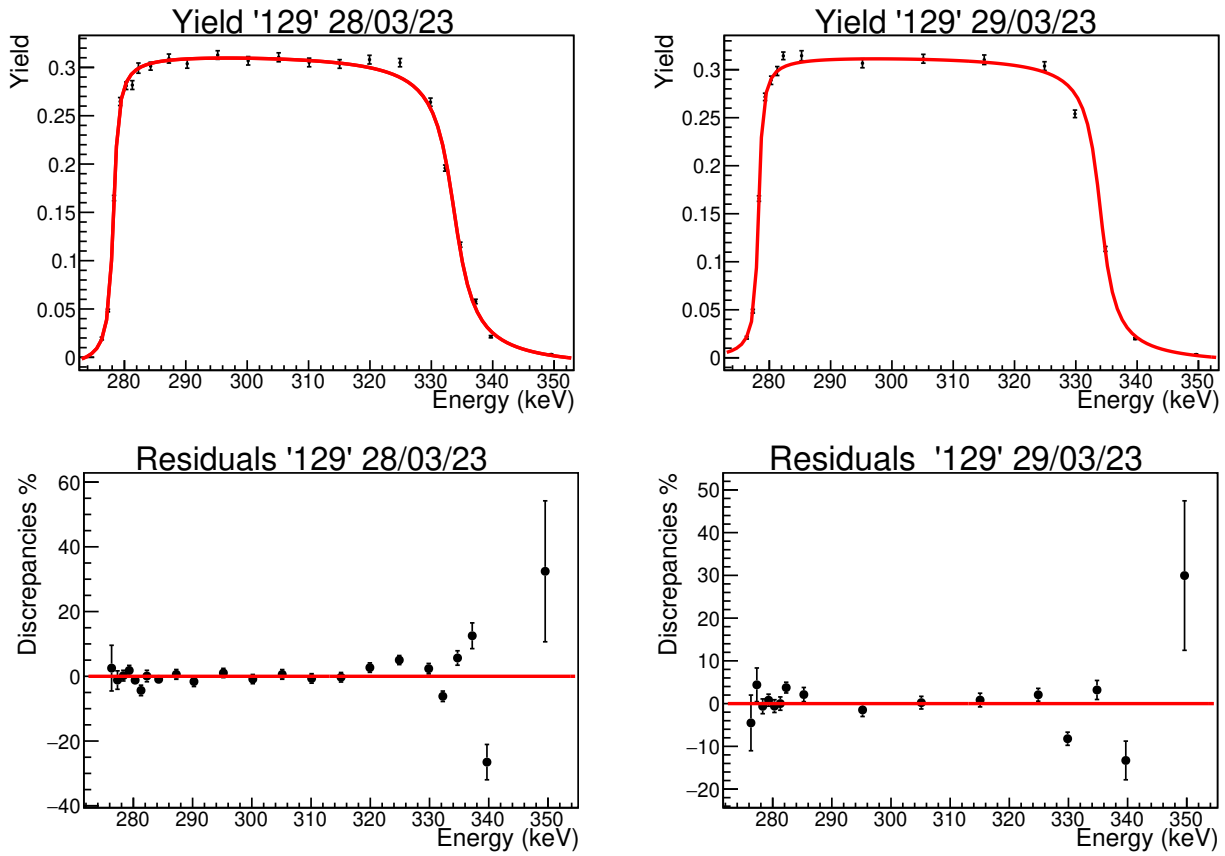

Figure 42: Fit of the yield profile together with the residuals of '129' target (28 and 29 March 2023).

[4] A program was made to calculate the yield profile and the thickness in energy ΔE of the target given the stoichiometry obtained from RBS analysis (percentages of the elements present and target thickness in atoms/cm^2).

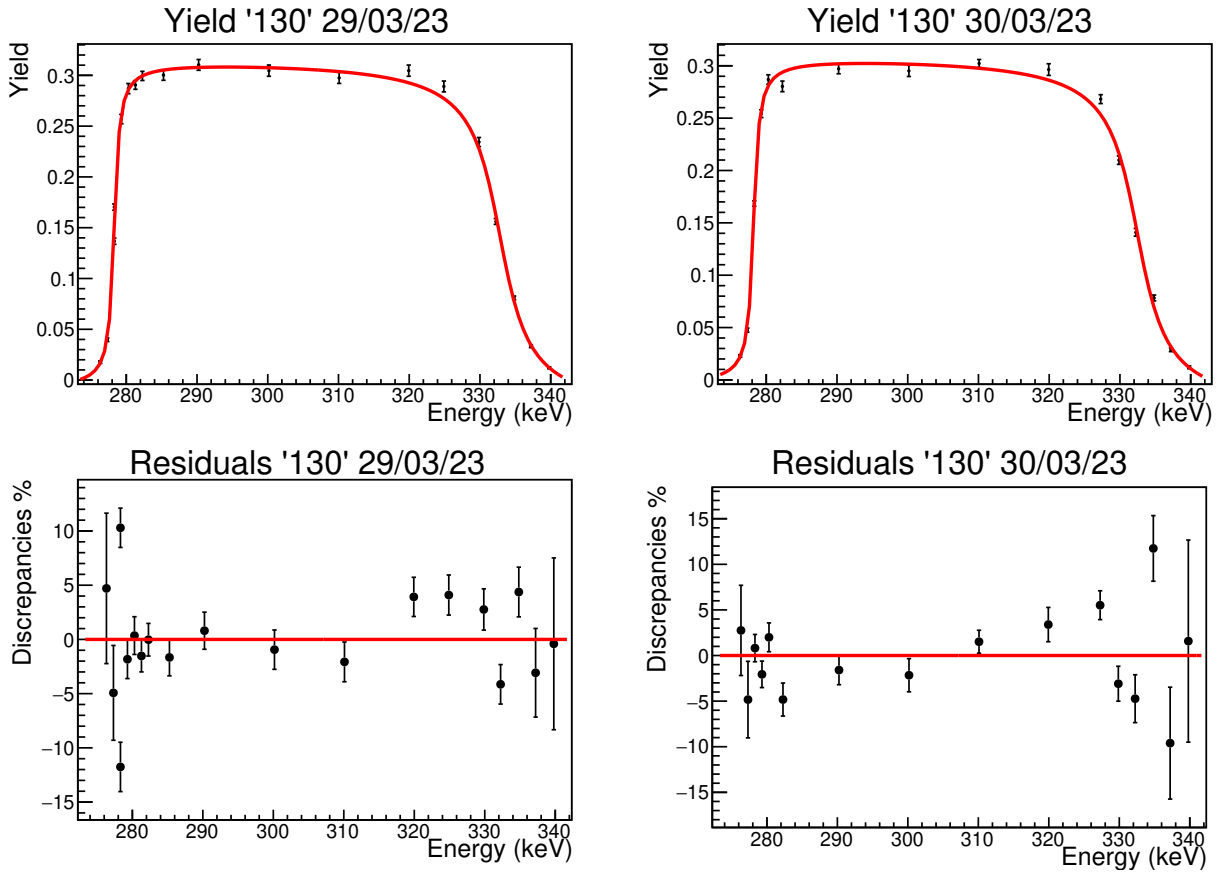

Figure 43: Fit of the yield profile together with the residuals of '130' target (29 and 30 March 2023).

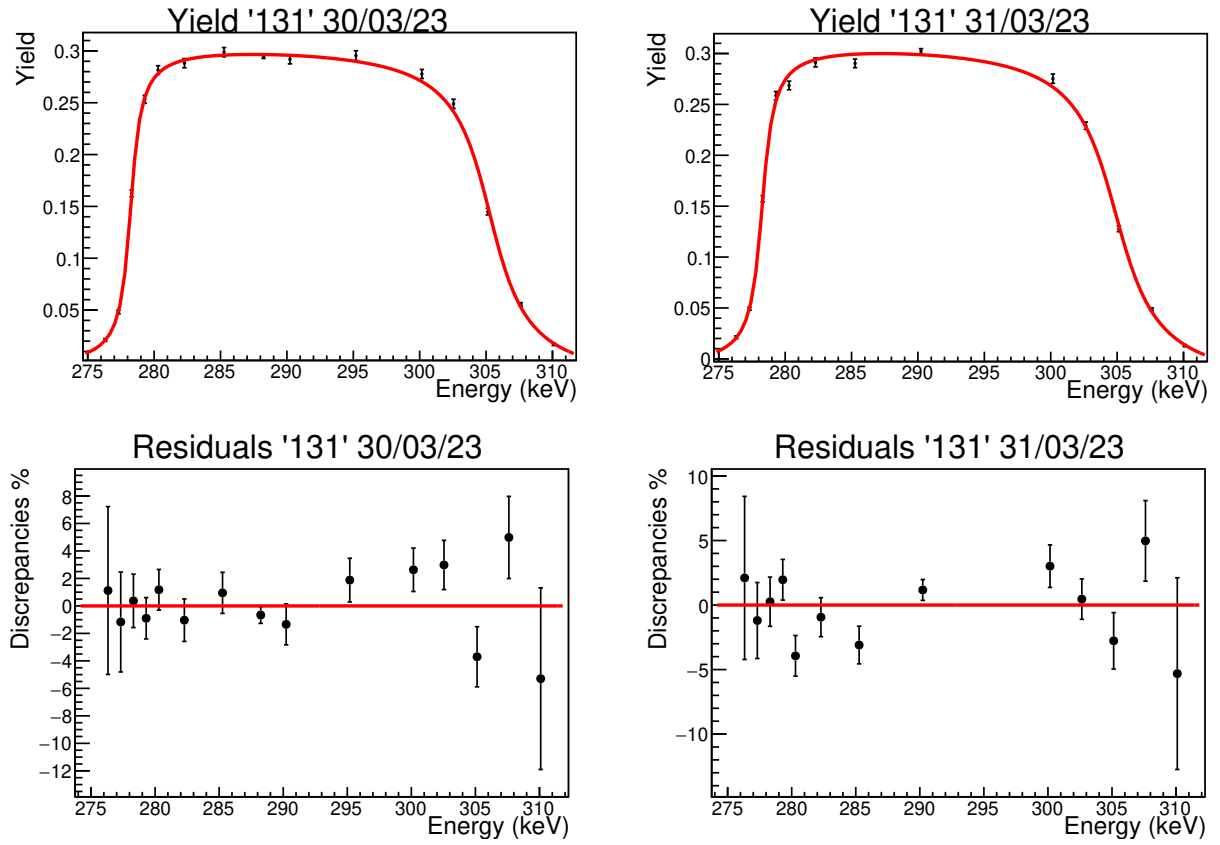

Figure 44: Fit of the yield profile together with the residuals of '131' target (30 and 31 March 2023).

Target	Γ_1 (keV)	Γ_2 (keV)	ΔE (keV)	ΔE_{th} (keV)
'129' (28/03)	1.26 ± 0.06	5.0 ± 0.2	55.46 ± 0.07	53 ± 1
'129' (29/03)	1.02 ± 0.07	3.6 ± 0.2	55.75 ± 0.08	53 ± 1
'130' (29/03)	1.11 ± 0.08	6.2 ± 0.3	54.51 ± 0.08	52 ± 1
'130' (30/03)	1.15 ± 0.07	6.3 ± 0.3	54.2 ± 0.1	52 ± 1
'131' (30/03)	1.20 ± 0.07	4.3 ± 0.2	27.04 ± 0.07	26 ± 1
'131' (31/03)	1.32 ± 0.08	4.7 ± 0.2	26.63 ± 0.07	26 ± 1

Table 17: Parameters obtained from the fit and target thicknesses expected from the RBS analysis ΔE_{th}.

3.3.6 Estimation of the $\omega\gamma$ factor

As aforementioned in sections 1.4 and 3.3.1, the $\omega\gamma$ parameter is important to determine the reaction rate for narrow resonances and can be estimated in the thick target approximation from the plateau of the yield profile of the targets. Here we give an estimation for the strength of the resonant state at $E_r^{lab} = 278$ keV and compare it with the literature value. Experimental yields for the ^{15}O transitions obtained from the targets resonance scans were corrected by the peak efficiency, obtained with the method that fits the yield ratios in section 3.3.3, and by the summing out and summing in contributions and multiplied by the charge factor e = $1.602 \cdot 10^{-19}$C, in order to obtain the yield in number of reactions per unit of beam particle. The $\omega\gamma$ factor can be estimated from the total yield for a point on the plateau of the yield profile, i.e. from the sum of the partial yields of the primary transitions $Y_{tot} = Y_{673} + Y_{1380} + Y_{2373} + Y_{7554}$, using Eq. 34 in section 3.3.1.
In Tab. 18 the yields for each transition are reported together with the total yield for the '129' sputtered target. In Tab. 19 is reported the value of the $\omega\gamma$ factor estimated from each target together with the compatibility [5] with the theoretical value taken from [1] ($\omega\gamma_{th} = 13.7 \pm 0.7$ meV).

E_γ (keV)	$Y = N_R/N_b \cdot 10^{-12}$ (28/03)	$Y = N_R/N_b \cdot 10^{-12}$ (29/03)
763.4 ± 1.7	1.24 ± 0.03	1.26 ± 0.04
1380.1 ± 1.7	2.87 ± 0.07	3.00 ± 0.08
2373 ± 1	0.77 ± 0.03	0.81 ± 0.04
7554.5 ± 0.4	0.13 ± 0.02	0.13 ± 0.02
6791.4 ± 1.7	1.13 ± 0.08	1.20 ± 0.09
6174.9 ± 1.7	3.0 ± 0.2	3.0 ± 0.2
5182 ± 1	0.68 ± 0.09	0.7 ± 0.1
Y_{tot}	5.01 ± 0.08	5.2 ± 0.1

Table 18: Yields obtained from the primary and secondary transitions of ^{15}O, corrected for the summing effects for the '129' target at $E_p = 284.3$ keV (data taken on 28/03/23) and at $E_p = 285.3$ keV (data taken on 29/03/23).

[5] The compatibility between two quantities a and b is calculated as: $\lambda = \frac{|a-b|}{\sqrt{\sigma_a^2+\sigma_b^2}}$ and it is considered 'optimal' when $\lambda \in [0,1]$, 'good' when $\lambda \in [1,2]$, 'not good' when $\lambda \in [2,3]$ and 'bad' when $\lambda > 3$.

	$\omega\gamma$ (meV)	$\lambda(\omega\gamma_{\text{exp}}, \omega\gamma_{\text{th}})$
'129' (28/03)	12.6 ± 0.2	1.49
'129' (29/03)	13.1 ± 0.2	0.82
'130' (29/03)	12.8 ± 0.2	1.28
'130' (30/03)	12.3 ± 0.2	1.90

Table 19: $\omega\gamma$ factor obtained from the total yield on the plateau of the yield profile for different targets and compatibility with the theoretical value $\omega\gamma_{\text{th}}$.

It is also possible to have an estimation of the branching ratios of the primary γ ray transitions by dividing the experimental yield of each transition by the total one. In Tab. 20 are reported the estimations of these factors obtained from the yields of targets '129' and '130' together with the values from literature [6].

	$\text{BR}_{\gamma,763}$	$\text{BR}_{\gamma,1380}$	$\text{BR}_{\gamma,2373}$	$\text{BR}_{\gamma,7554}$
'129' (28/03/23)	0.247 ± 0.008	0.57 ± 0.02	0.153 ± 0.007	0.026 ± 0.003
'129' (29/03/23)	0.242 ± 0.009	0.58 ± 0.02	0.156 ± 0.008	0.025 ± 0.003
'130' (29/03/23)	0.248 ± 0.009	0.58 ± 0.02	0.151 ± 0.008	0.020 ± 0.003
'130' (30/03/23)	0.237 ± 0.008	0.58 ± 0.02	0.158 ± 0.008	0.027 ± 0.004
Literature values	0.232 ± 0.005	0.575 ± 0.002	0.158 ± 0.005	0.035 ± 0.005

Table 20: Branching ratios for each primary transition obtained from targets '129' and '130' compared with literature values.

Another way to estimate the $\omega\gamma$ factor is from the parameter R in equation 42 in section 3.3.3. As aforementioned in that section, this parameter can be included in the fit for the efficiency curve using the yields for every transition of ^{15}O, and used to estimate the $\omega\gamma$ factor using Eq. 34 in section 3.3.1 and substituting the total yield with the parameter R multiplied by the charge factor e. Parameters for each target are given in Tab. 21 together with the $\omega\gamma$ value and its compatibility with the theoretical value $\omega\gamma_{\text{th}}$. There is a 7 % difference between the parameters obtained from this method and the ones reported previously in Tab. 19, with a compatibility λ between 2 and 3. This may be due to the discrepancy between the efficiency curves obtained in section 3.3.3.

	R $(\mu\text{C})^{-1}$	$\omega\gamma$ (meV)	$\lambda(\omega\gamma_{\text{exp}}, \omega\gamma_{\text{th}})$
'129' (28/03/23)	33.5 ± 0.7	13.5 ± 0.3	0.27
'129' (29/03/23)	34.8 ± 0.7	14.0 ± 0.3	0.44
'130' (29/03/23)	34.3 ± 0.7	13.8 ± 0.3	0.12
'130' (30/03/23)	32.7 ± 0.7	13.1 ± 0.3	0.73

Table 21: $\omega\gamma$ factor obtained from the R parameter on the plateau on the yield profile for different targets, and compatibility with the theoretical value $\omega\gamma_{\text{th}}$.

3.3.7 Calculation for the implanted target profile and comparison with data

The implanted target produced and analyzed through the RBS technique at Lisbon presents a non homogeneous distribution of the nitrogen content as a function of depth: this influences the shape of the target's yield profile. A calculation is made to try to reproduce the yield profile

[6] Data taken from *https://www.nndc.bnl.gov/nudat3/.*

of the implanted target data obtained on 27 March 2023. The yield for each bombarding energy in the range E_p = 275-300 keV with steps of 0.1 keV is calculated as:

$$Y(E_p) = \sum_i \int_{\Delta E_i} \frac{\sigma(E)}{\epsilon_{eff,i}(E)} dE, \tag{48}$$

which is the formula 30 given in section 3.3.1 generalized to a target composed by more sublayers. The stopping powers for N and Ta are obtained using SRIM 2013 [29].
The cross section is calculated up to a normalization constant A (to be fitted with the experimental data) as:

$$\sigma(E) = \frac{A}{[(E - E_r)^2 + \Gamma^2/4]}, \tag{49}$$

where Γ and E_r are the width of the resonant state and its corresponding energy respectively. The parameter A is related to the $\omega\gamma$ factor relative to the E_r^{lab} = 278 keV resonance, since the integrated cross section, i.e. the yield, is related to the strength of the resonance through Eq. 34 in section 3.3.1 for thick target approximation. A straggling effect is also added to the calculated data. We started from the target stoichiometry given by Lisbon RBS analysis and then varied the number of sublayers and the percentages of nitrogen until they reproduced the data from the resonance scan taken on 27 March 2023. The parameter used to normalize the cross section to the experimental data is A = $(3.47 \pm 0.01) \cdot 10^{-11}$ keV^2 b. In Tab. 22 are reported the percentage of ^{14}N and the target thickness in atoms/cm^2 for each of the sublayers in which the target was divided obtained from the analysis at Lisbon, while in Tab. 23 are reported the same quantities after varying the stoichiometry.

Layer	^{14}N(%)	Δx (10^{15} atoms/cm^2)
1	55.0132	547.0132
2	41.2155	140.000
3	12.000	100.000
4	3.1721	100.000

Table 22: Percentages of ^{14}N and target thickness for each of the sublayers of the implanted target obtained from Lisbon RBS analysis.

Layer	^{14}N(%)	Δx (10^{15} atoms/cm^2)
1	31.1	29.584
2	47.6	59.168
3	50.1	88.752
4	51.9	88.752
5	52.2	88.752
6	59.7	88.752
7	48.3	88.752
8	41.4	88.752
9	24.4	88.752
10	9.70	88.752
11	3.70	88.752

Table 23: Percentages of ^{14}N and target thickness for each of the sublayers of the implanted target obtained from the calculation using data taken on 27 March 2023.

In Fig. 45 is reported the curve obtained using the stoichiometry data from Lisbon (green curve) together with experimental data taken on 27 March 2023 and the same calculation but

using a different stoichiometry determined in this thesis on the basis of the experimental data taken at LUNA 400 (violet curve). In Fig. 46 also the data taken after target irradiation is plotted. By comparing the experimental data taken on 27 march with the curve obtained from Lisbon stoichiometry, it seems that there is a reduction of the nitrogen content in the more superficial layers, due to RBS analysis or some other mechanism which may have altered the target structure. This is also evident if we compare Tab. 22 with 23: the percentage of nitrogen for the first layers of the target that fits the data is reduced with respect to the one given by Lisbon analysis. Furthermore it seems that some ^{14}N was removed after beam irradiation between 27 and 28 March.

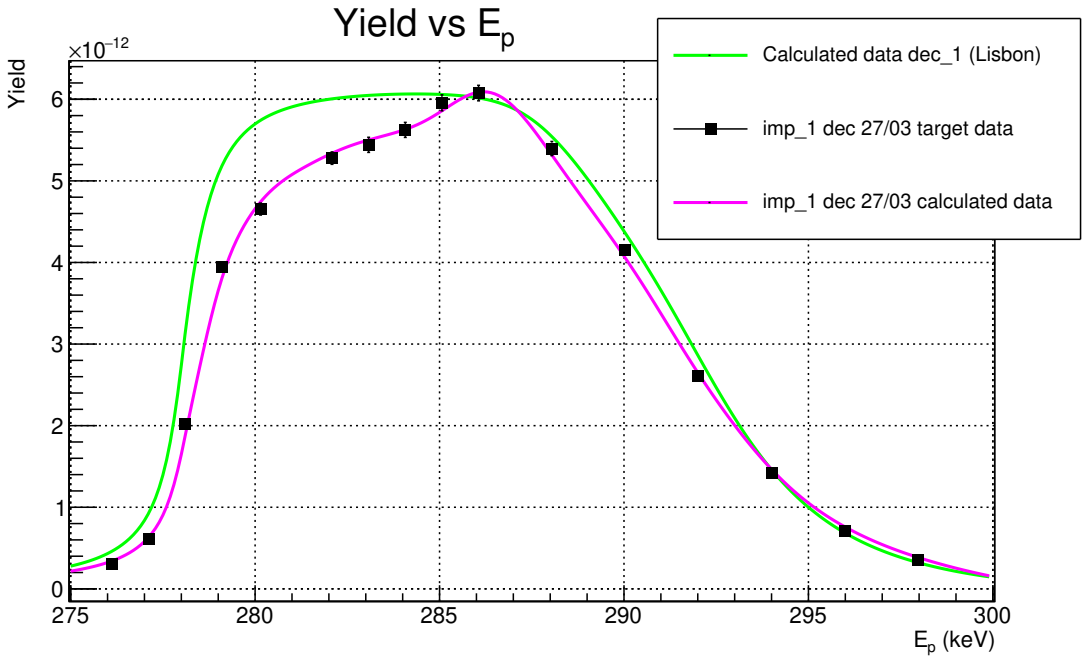

Figure 45: Calculation of the implanted target obtained from the stoichiometry given by Lisbon RBS analysis and by varying the number of layers and the percentages of ^{14}N together with data obtained on 27/03/23.

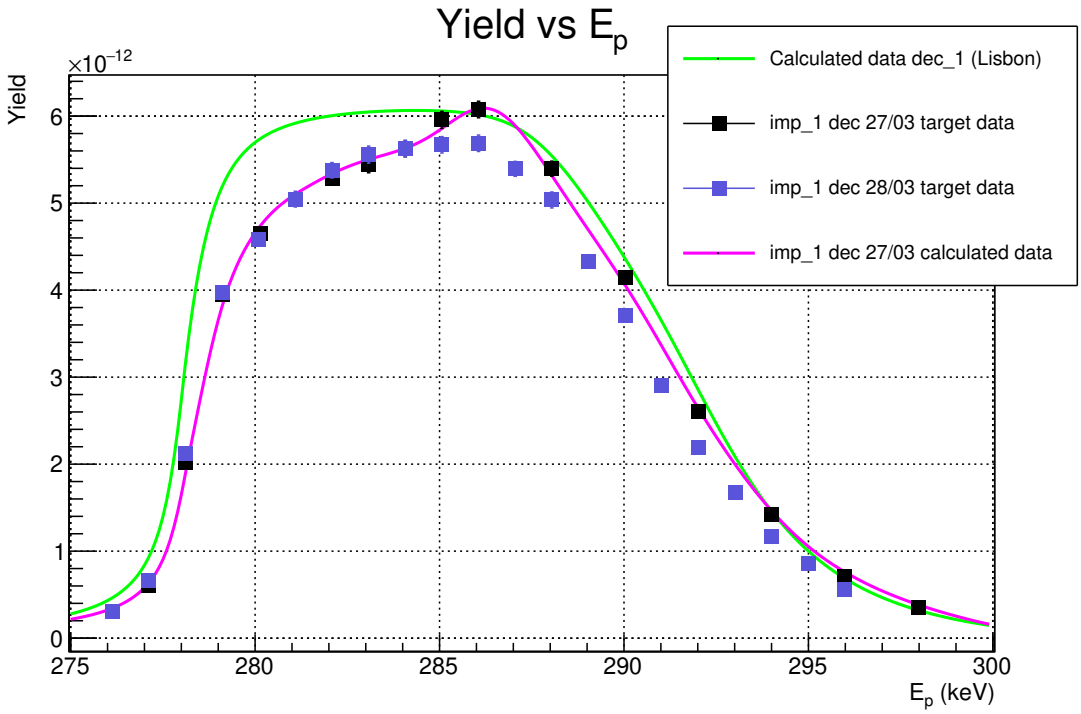

Figure 46: Calculation of the implanted target obtained from the stoichiometry given by Lisbon RBS analysis and by varying the number of layers and the percentages of ^{14}N together with data obtained on 27/03/23 and on 28/03/23.

3.3.8 Considerations on targets analysis

Solid TaN targets have been studied, showing to be stable over a long period of irradiation, without visible deformations of the yield profile. For what concerns contamination, the most clean was found to be the sputtered '131' one, with the lowest level of fluorine. It presents also a low level of ^{15}N compared to the other sputtered targets, and of the ^{12}C(p,γ)^{13}N reaction. Sputtered targets in particular have no contamination from ^{27}Al and ^{16}O. The target thickness in energy was determined from a fit of the yield profile and compared to the nominal values obtained from simulations based on the stoichiometry given by the RBS analysis. The thickness was in agreement with the nominal values except for a discrepancy of a few keV, but this probably enters the uncertainties of the two methods used that have to be accurately defined in the next data acquisition. For what concerns the $\omega\gamma$ factor, the estimation more compatible with the theoretical value seems to be the one relative to the '129' sputtered target for the method which obtains the efficiency curve from the yield ratios, and the one obtained by the '130' sputtered one for the method which fits the R parameter. But it has to be noticed that the two methods are probably affected by a systematic error in the efficiency determination. The $\omega\gamma$ factors more compatible with the theoretical value are the ones obtained from the method which fits the R parameter. The stoichiometry of the implanted target has also been analyzed through a calculation, showing a reduction of the nitrogen content on the surface with respect to the one obtained by Lisbon RBS analysis, probably due to the latter process or other mechanisms not yet understood.

4 New beamtime at LUNA MV

As discussed in the previous chapters, a new experiment for the $^{14}N(p,\gamma)^{15}O$ reaction has to be performed in a wide energy range between 200 keV and 1400 keV at the "Bellotti" ion beam facility. The new LUNA MV accelerator recently installed at the LNGS laboratories is capable to provide high intensity beams of H, He and C, with a terminal voltage of 3.5 MV. Two beam lines are available, and are separated by a magnet. In Fig. 47 is shown a scheme of the new experimental setup installed at the "Bellotti" facility that is planned to be used for the new measurements.

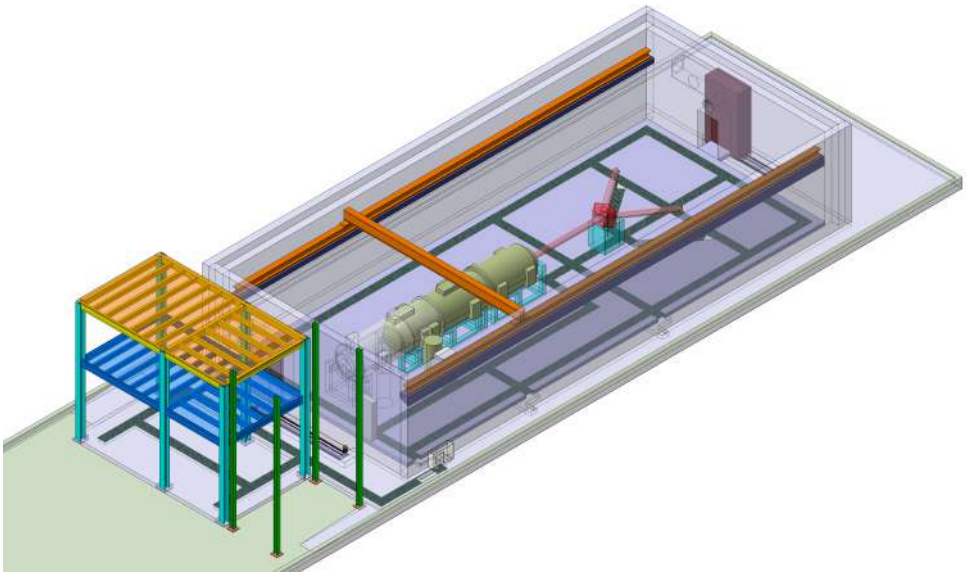

Figure 47: Design of the new experimental setup installed at the "Bellotti" ion beam facility (picture taken from https://www.lngs.infn.it/en/luna).

The experiment is still in phase of characterization and in this thesis we focus in the estimation of the beam time needed to have a good counting statistics for each energy value in the 200-1400 keV energy range, starting from the calculation of the expected count rate. We also estimate the charge accumulated during the beam time for each energy point and try to plan a scheme for the new measurements alternating scans of the $E_r = 259$ keV resonance to the direct capture measurements.
The expected count rate has been calculated for the capture to the ground state of ^{15}O transition and for the capture to the 6.79 MeV level of ^{15}O. The stoichiometries of targets '129' and '130' obtained from RBS analysis were used, reported in Tab. 24. For the implanted target instead, the stoichiometry obtained in Tab. 23 in section 3.3.7 was used.

Target	$^{14}N(\%)$	$^{15}N(\%)$	Ta(%)	Ar(%)	Δx (10^{18} atoms/cm^2)
'129'	47.31	0.19	50	2.5	2.54
'130'	47.50	0	50	2.5	2.48

Table 24: Percentages of ^{14}N, ^{15}N, Ta and Ar together with the target thickness Δx of '129' and '130' sputtered targets.

The count rate is calculated for every beam energy E_p in the range 200-1400 keV at steps of 10 keV as:

$$R(E_p) = \epsilon_{peak} \frac{Y(E_p)I}{e}, \tag{50}$$

where a beam current on the target I = 150 μA is assumed, Y(E_p) is the yield calculated by integrating the cross section as in Eq. 30, e is the electric charge and ϵ_{peak} is the peak efficiency of the Ge detector, relative to the gamma ray of the transition considered.
The efficiency of the detector is still in phase of characterization since the setup has been mounted recently. Here we give an estimation for a geometry configuration in which the germanium detector is placed immediately after the scattering chamber. We assume a value of 1%, also based on the peak efficiency curve obtained in the data analysis section and based on similar experimental setups. Data for the cross section were obtained from [17]. In Fig. 48, 49 and 50 is reported the expected count rate as a function of the proton energy obtained for the implanted, '129 and '130' targets respectively.

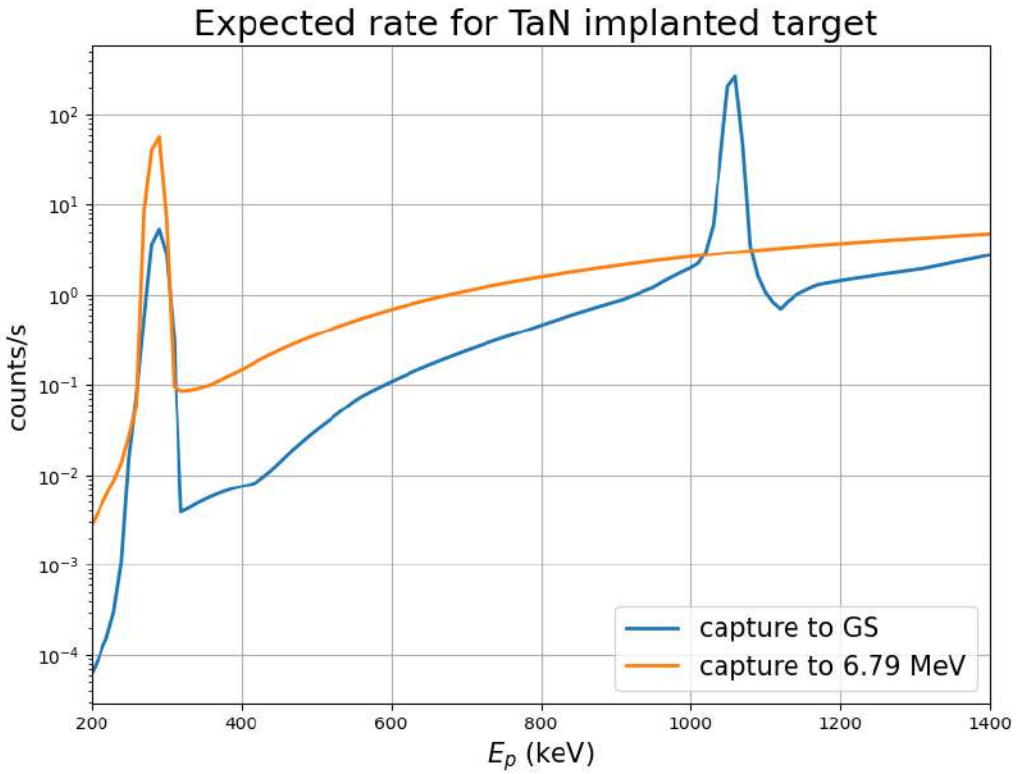

Figure 48: Expected count rate for the capture to the ground state and for the capture to the 6.79 MeV level transitions calculated for the implanted target.

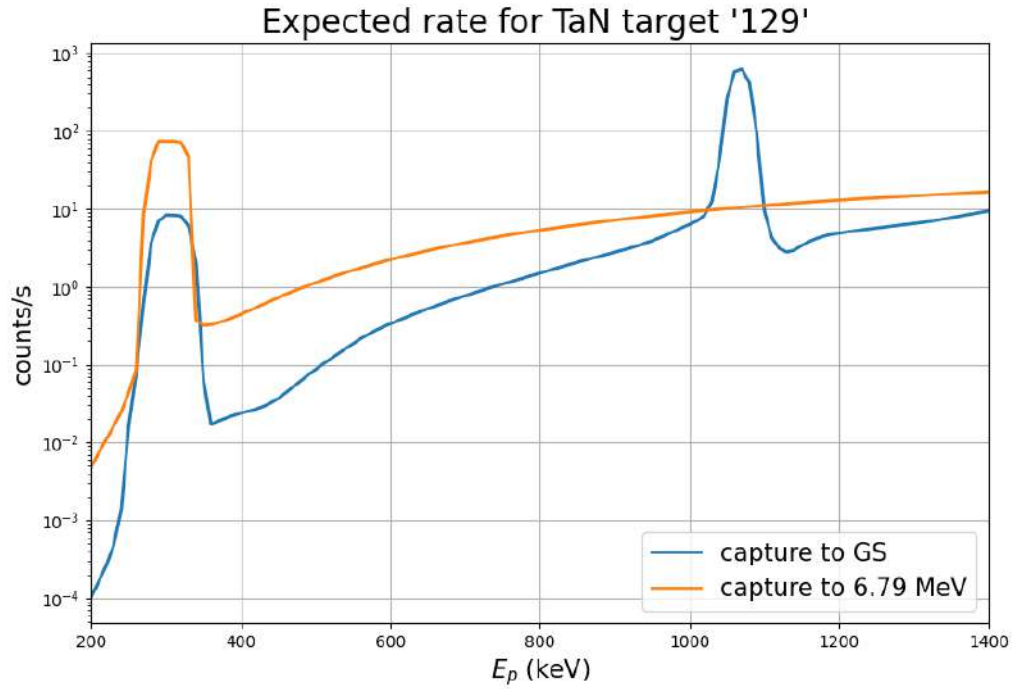

Figure 49: Expected count rate for the capture to the ground state and for the capture to the 6.79 MeV level transitions calculated for the '129' sputtered target.

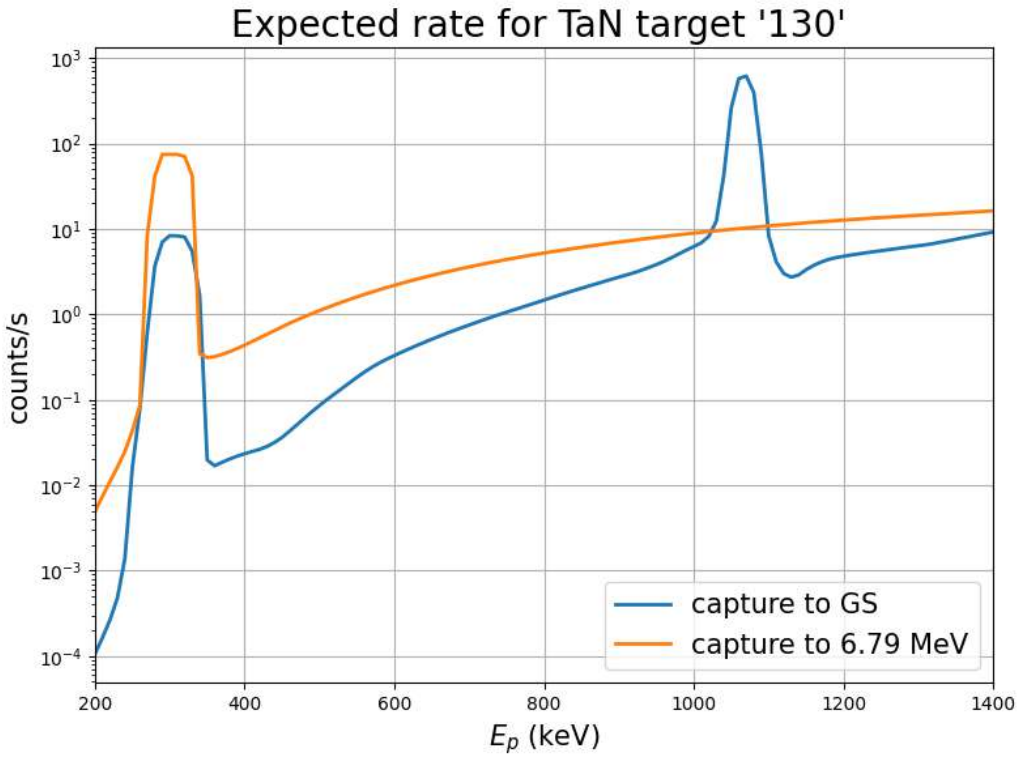

Figure 50: Expected count rate for the capture to the ground state and for the capture to the 6.79 MeV level transitions calculated for the '130' sputtered target.

Starting from the count rate, an estimation of the time required to acquire 10000 counts for each energy value in the range 200-1400 keV at steps of 100 keV is made, together with

the accumulated charge Q. As exercise the time needed to acquire 10000 counts at the Solar Gamow peak (50 keV) is also reported in the table. This demonstrates that even with state of the art experimental setup this energy is not accessible with direct approaches. Data are reported in Tab. 25 for the capture to the ground state and for the capture to the 6.79 MeV level of ^{15}O transitions using the '129' sputtered target.

Energy (keV)	Δt_{GS} (h)	$\Delta t_{6.79MeV}$ (h)	Q_{GS} (C)	$Q_{6.79MeV}$ (C)
50	$8.6 \cdot 10^{10}$	$5.3 \cdot 10^{9}$	$4.62 \cdot 10^{10}$	$2.49 \cdot 10^{10}$
200	26000	570	14200	7690
300*	0.33	0.037	0.180	0.0972
400	120	6.3	62.9	34.0
500	32	2.5	17.2	9.30
600	8.3	1.2	4.47	2.41
700	3.6	0.76	1.96	1.06
800	1.9	0.52	1.00	0.540
900	1.0	0.39	0.540	0.291
1000	0.44	0.30	0.237	0.128
1100*	0.30	0.25	0.160	0.0865
1200	0.57	0.21	0.307	0.166
1300	0.43	0.19	0.231	0.125
1400	0.30	0.17	0.160	0.0864

Table 25: Time required to acquire 10000 counts for each energy value from 200 keV to 1400 keV at steps of 100 keV, together with the corresponding accumulated charge. Also the time required for 50 keV is reported. Data are calculated for the '129' sputtered target for each transition analyzed. The energies marked with the * are those that cover the resonances at $E_r = 259$ keV and $E_r = 987$ keV in the center of mass.

It has to be noticed that a statistics of 10000 counts for each energy value below 200 keV requires several years, and at 50 keV from 10^5 to 10^6 years of beam time are needed, depending on the transition considered. In addition, the new accelerator is unable to go below 200 keV in energy, so the latter measurement cannot be performed.
The range of energies for which it is feasible to have good statistics in a reasonable beam time ranges from 300 keV to 1400 keV. The total time needed to acquire all the points in this energy range at steps of 100 keV are 170 hours and 13 hours for the capture to the ground state transition and for the capture to the 6.79 MeV level of ^{15}O respectively. The total charge accumulated instead is 89.4 C for the capture to the ground state transition and 48.3 C for the capture to the 6.79 MeV level of ^{15}O.
The two resonances at $E_r = 259$ keV and $E_r = 987$ keV in the center of mass are points that have to be accurately analyzed, and they correspond to peaks in the expected count rate. The $E_r = 259$ keV resonance has been studied in several experiments and is well known: to obtain a value of the $\omega\gamma$ parameter for this resonance and for the one at $E_r = 987$ keV can be useful to relate these two quantities in the same experiment. Furthermore, the data that will be obtained for the first resonance can be compared with the ones previously taken with the LUNA 400 accelerator to have a cross check. In addition, the resonant state at lower energy is optimal for performing resonance scans, since lower energies and thicker targets permit to reduce the straggling effects and so the associated systematic errors.
In Tab. 26 we report the time needed to acquire each energy point for the scan of the resonance at lower energy, using the '129' sputtered target, together with the accumulated charge. Data are taken from the analysis did at the LUNA 400 accelerator. The total time needed to perform a resonance scan is 0.87 hours, with an overall accumulated charge of 0.383 C.

Energy (keV)	Δt (h)	Q (C)	Energy (keV)	Δt (h)	Q (C)
282.3	0.025	0.0112	305.1	0.034	0.0152
281.3	0.031	0.0142	310.1	0.037	0.0161
280.3	0.044	0.0197	315.1	0.037	0.0160
279.3	0.035	0.0163	319.9	0.038	0.0160
278.3	0.052	0.0236	324.9	0.039	0.0175
277.3	0.059	0.0271	329.9	0.035	0.0154
276.3	0.026	0.0116	334.7	0.042	0.0183
284.3	0.041	0.0188	339.7	0.044	0.0184
287.2	0.033	0.0149	337.2	0.028	0.0118
290.2	0.033	0.0146	332.2	0.050	0.0207
295.2	0.037	0.0165	349.5	0.032	0.0121
300.2	0.038	0.0169			

Table 26: Time required to acquire data for each energy point of the E_r = 259 keV resonance scan using the '129' target (data are obtained from the scan did during data acquisition at LUNA 400). Also the charge accumulated for each energy point is shown.

If we want to plan an experiment in which we alternate scans of the E_r = 259 keV resonance to measurements for the direct capture, including also the two points that reach the two resonant states, we can proceed as the following, starting from the '129' target and changing it with another one if the overall accumulated charge exceeds 200 C, based on the considerations made in [16]. For what concerns the capture to the 6.79 MeV level of ^{15}O, it is possible to acquire all data points for the direct capture in one day. We take one resonance scan and all the measurements except from the one at 400 keV and then start a long run lasting 17 hours to acquire the latter point (in one lung run the target accumulates 9.24 C). The overall charge accumulated is Q = 23.9 C, so the target does not need to be changed. A resonance scan can be made to verify the target stability.
The capture to the ground state transition instead requires 10 days of acquisition, starting from one resonance scan and measurements of the points from 800 keV to 1400 keV, and the point at 300 keV. Then a long run lasting 17 hours can be done for the point at 600 keV. In the second day we can do another resonance scan and the measurement at 700 keV, followed by a long run for the point at 500 keV. The third day another resonance scan can be taken, followed by the long run which completes the acquisition time needed for the point at 500 keV. Other seven days of acquisition with corresponding resonance scans are needed to acquire sufficient statistics for the point at 400 keV. The target does not need to be changed, since the overall accumulated charge is Q = 101 C.
We could also repeat the same measurements but using another target with a different stoichiometry, such as the implanted one. This can be done in order to see the variation of the cross section with the target stoichiometry, and thus for estimating the corresponding systematic error. The time needed to acquire a statistics of 10000 counts for one data point relative to the direct capture measurements, using the implanted target, is 70 % higher than the one required for the '129' target. In Fig. 51 we report a comparison of the times of acquisition needed for the two targets considering the capture to the 6.79 MeV level of ^{15}O transition. The implanted target has a lower width in energy if compared with the '129' one and this implies a lower count rate and a corresponding higher acquisition time. We can plan to perform measurements for this target only for some of the points in the energy range between 300 keV and 1400 keV.

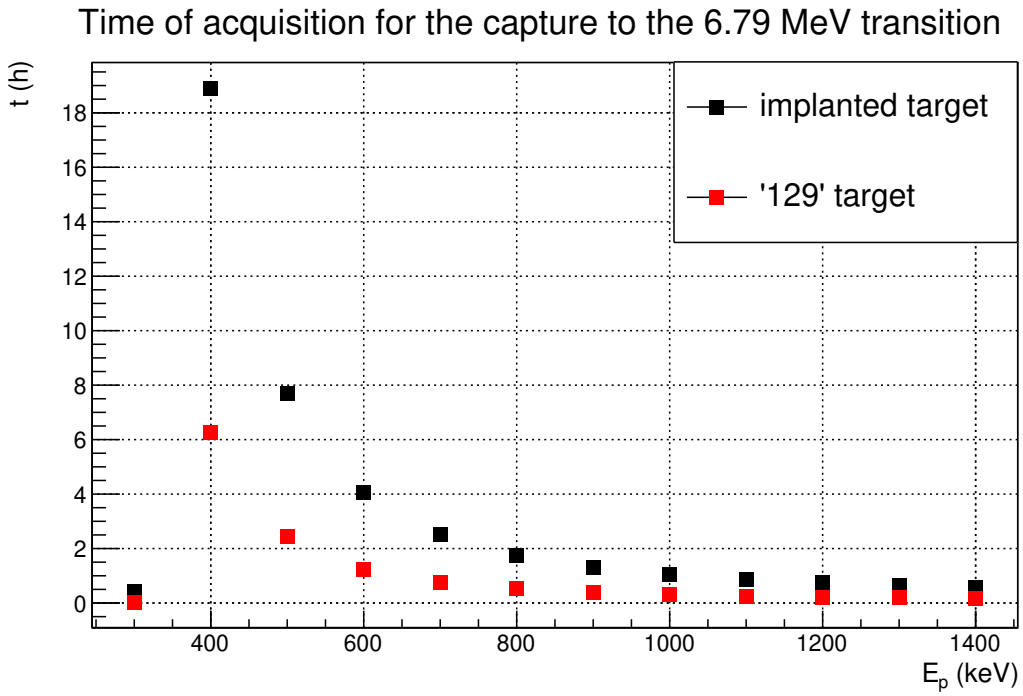

Figure 51: Acquisition times for the implanted and '129' sputtered targets relative to the capture to the 6.79 MeV level of ^{15}O transition. A statistics of 10000 counts for each energy value in the range 300-1400 keV at steps of 100 keV is considered.

4.1 Conclusions

To conclude, this thesis focuses on the ^{14}N(p,γ)^{15}O reaction, which determines the rate of the first CNO cycle and consequently influences the energy production and nucleosynthesis of a star. It is of particular importance for the understanding of the main astrophysical open issues, such as the Globular Clusters' age determination, which depends strongly on the rate of this reaction and gives an upper limit to the age of the Universe. The cross section of the ^{14}N(p,γ)^{15}O reaction has to be determined with high precision, since it is related to the Standard Solar Model for determining the Sun's chemical composition and the fluxes of solar neutrinos recently measured in the Borexino experiment.

It is fundamental to measure the cross section of this reaction in a wide energy range in order to have a good extrapolation down to low astrophysical energies that no experiment can achieve. For this purpose, new measurements in a wide energy range from 200 keV to 1400 keV are planned at the new facility installed at the Gran Sasso National Laboratories, thanks to the LUNA MV accelerator capable to provide sufficiently high beam intensities.

In this thesis we focused on one of the most important sources of uncertainty in the reaction, such as the targets. The four targets were produced at Lisbon and LNL laboratories through two different techniques: implantation and sputtering. In chapter 3 we proceeded to their characterization by checking their stability over long periods of beam time and by analyzing the most important sources of contamination. The target thickness in energy was determined with two different methods. Then the percentage of nitrogen as a function of depth was calculated for the implanted target through a calculation, in order to have a comparison with the stoichiometry obtained from Lisbon RBS analysis. The targets showed to be stable over a night of beam time and the main sources of contamination are fluorine, carbon and ^{15}N. The two methods used to estimate the thickness in energy are quite in agreement. A discrepancy in the nitrogen content of the implanted target was found comparing the stoichiometry given by RBS analysis and the one estimated from the experimental data taken during the targets characterization,

with a reduction in the superficial nitrogen content probably due to the RBS procedure itself. With the data provided by the resonance scans the strength $\omega\gamma$ of the $E_r = 259$ keV resonance has been estimated and compared with the literature value, showing to be in agreement with it.

At the end of the thesis a planning for the new beam time to be performed at the LUNA MV accelerator has been done, estimating in particular the count rate for two important transitions of the $^{14}N(p,\gamma)^{15}O$ reaction. From the count rate it was possible to estimate the time required to acquire sufficient statistics for some of the energies in the range of interest and the charge accumulated during the beam time, trying to plan a scheme for the new measurements. For this purpose we used the parameters of the targets studied and the results obtained show the feasibility of the new measurements foreseen for the new LUNA experiment.

References

[1] C. Iliadis, *Nuclear Physics of stars*, WILEY-VCH Verlag GmbH & Co. KGaA, printed in Darmstadt, 2007, ISBN: 978-3-527-40602-9.

[2] G. R. Gilmore, *Practical Gamma-ray Spectroscopy*, second edition, John Wiley & Sons, Southern Gate, Chichester, West Sussex, England, 2008, ISBN: 978-0-470-86196-7.

[3] G. F. Knoll, *Radiation and detection measurement*, fourth edition, John Wiley & sons, printed in the United States of America, 2010, ISBN: 978-0-470-13148-0.

[4] A. Formicola, *A new study of* $^{14}N(p,\gamma)^{15}O$ *at low energy*, PhD. Thesis, Bochum University, 2004.

[5] M. Asplund et al., *The Chemical Composition of the Sun*, Annu. Rev. Astron. Astrophys., 47, 481-522, 2009, DOI: 10.1146/annurev.astro.46.060407.145222.

[6] The Borexino collaboration, *Experimental evidence of neutrinos produced in the CNO fusion cycle in the Sun*, Nature, 587, 2020, DOI: https://doi.org/10.1038/s41586-020-2934-0.

[7] A. Serenelli, C. P. Garay, W. C. Haxton, *Using the standard solar model to constrain solar composition and nuclear reaction S factors*, Phys. Rev. D, 87, 2013, DOI: 10.1103/PhysRevD.87.043001.

[8] W.C. Haxton, A. M. Serenelli, *CN Cycle solar neutrinos and the Sun's primordial core metallicity*, The Astrophysical Journal, 687, 678-691, 2008, DOI:10.1086/591787.

[9] G. Imbriani et al., *The bottleneck of the CNO burning and the age of the Globular Clusters*, Astron. Astrophys., 420, 625-629, 2004, DOI: https://doi.org/10.48550/arXiv.astro-ph/0403071.

[10] F. Herwig et al., *Nuclear reaction rate uncertainties and astrophysical modeling: Carbon yields from low-mass giants*, Phys. Rev. C 73, 2006, DOI:10.1103/PhysRevC.73.025802.

[11] M. J. Thompson, *Helioseismology and the Sun's interior*, Astronomy & Geophysics, 45, Issue 4, 2004, DOI: https://doi.org/10.1046/j.1468-4004.2003.45421.x.

[12] M. Marta, *The* $^{14}N(p,\gamma)^{15}O$ *reaction studied at low and high beam energy*, PhD. Thesis, Dresden, 2011.

[13] U. Schroeder et al., *Stellar reaction rate of* $^{14}N(p,\gamma)^{15}O$ *and hydrogen burning in massive stars*, Nucl. Phys. A, 467, 240-260, 1987, DOI: 10.1016/0375-9474(87)90528-8.

[14] R. C. Runkle. et al., *Direct Measurement of the $^{14}N(p,\gamma)^{15}O$ S Factor*, Physical Review Letters, 94, 2005, DOI: 10.1103/PhysRevLett.94.082503.

[15] L. Wagner et al., *Astrophysical S factor of the $^{14}N(p,\gamma)^{15}O$ reaction at 0.4-1.3 MeV*, Phys. Rev. C, 97, 2018, DOI: 10.1103/PhysRevC.97.015801.

[16] G. Imbriani et al., *S-factor of $^{14}N(p,\gamma)^{15}O$ at astrophysical energies*, Eur. Phys. J. A, 25, 455-466, 2005, DOI: 10.1140/epja/i2005-10138-7.

[17] Q. Li, R. J. deBoer, G. Imbriani et al., *Cross section measurement of $^{14}N(p,\gamma)^{15}O$ in the CNO cycle*, Phys. Rev. C, 93, 2016, DOI: 10.1103/PhysRevC.93.055806.

[18] M. Marta et al., *The $^{14}N(p,\gamma)^{15}O$ reaction studied with a composite germanium detector*, Phys. Rev. C 83, 2011, DOI: 10.1103/PhysRevC.83.045804.

[19] D. F. Hebbard, G. M. Bailey, *Non-resonant radiation from the $^{14}N(p,\gamma)$ reaction (II)*, Nuclear Physics, 49 666-685, 1963, DOI: https://doi.org/10.1016/0029-5582(63)90130-5.

[20] K. Yamada et al., *E1 strength of the 3/2 subtreshold state in ^{15}O studied by Coulomb excitation*, Physics letters B, 579, 265-270, 2004, DOI: 10.1016/j.physletb.2003.11.024.

[21] A. M. Mukhamedzhanov et al., *Asymptotic normalization coefficients for $^{14}N(p,\gamma)^{15}O$ and the astrophysical S factor for $^{14}N(p,\gamma)^{15}O$*, Physical Review C, 67, 2003, DOI: 10.1103/PhysRevC.67.065804.

[22] S. Berg, T. Nyberg, *Fundamental understanding and modeling of reactive sputtering processes*, *Thin Solid Films*, Science Direct, Vol. 476, 215-230, 2005, https://doi.org/10.1016/j.tsf.2004.10.051.

[23] Donald M. Mattox; *Physical Vapor Deposition (PVD) processes*, Elsevier Science Vol. 97, 417-430, 1999, DOI:https://doi.org/10.1016/S0026-0576(99)80043-9.

[24] D. M. Mattox, *Handbook of Physical Vapor Deposition (PVD) processing*, Elsevier, Oxford, 2010, ISBN: 978-8155-2037-5.

[25] P. J. Kelly, R. D. Arnell, *Magnetron sputtering: a review of recent developments and applications*, Vacuum, 56, 159-172, 2000, DOI: https://doi.or/10.1016/S0042-207X(99)00189-X.

[26] C. Torres et al., *Paschen law for argon glow discharge*, J. Phys. Conf. Ser. 370, 012067, 2012, DOI: 10.1088/1742-6596/370/1/012067.

[27] S. P. Das et al., *A Dielectric Barrier Discharge (DBD) Plasma Reactor: An Efficient Tool to Measure the Sustainability of Non Thermal Plasmas through the Electrical Breakdown of Gases*, IOP Conf. Ser. Mater. Sci. Eng. 410, 012004, 2018, DOI: 10.1088/1757-899X/410/1/012004.

[28] J. Wood, *Ion implantation*, Encyclopedia of Materials: Science and Technology, p. 4284-4286, 2001, ISBN: 0-08-0431526.

[29] J. F. Ziegler, M. D. Ziegler, J. P. Biersack, *SRIM–The stopping and range of ions in matter (2010)*, Nuclear Instruments and Methods in Physics research B, 268 1818–1823, 2010, DOI: 10.1016/j.nimb.2010.02.091.

[30] J. Cruz et al., *Surface Characterization and Performance Evaluation of Nitrogen Implanted Coinage Dies*, Processes 10(3) 479, 2022, DOI:https://doi.org/10.3390/pr10030479.

[31] T. R. Rautray, R. Narayanan, K. Kim, *Ion implantation of titanium based biomaterials*, Progress in Material Science, 56 1137-1177, 2011, DOI: 10.1016/j.pmatsci.2011.03.002.

[32] W. K. Chu, J. W. Mayer, M. A. Nicolet, *Backscattering spectrometry*, Academic Press INC, California Institute of Technology, 1978, ISBN: 0121738507.

[33] L. Palmetshofer, *Rutherford Backscattering Spectroscopy (RBS)*, Surface and Thin Film Analysis cap 11, Wiley-VCH Verlag GmbH & Co., 2011, ISBN: 9783527636921.

[34] A. Notea, Y. Gurfinkel, *Transitions in* ^{133}Cs *from the decay of* ^{133}Ba, Nuclear Physics A, 107, 193-208, 1968.

[35] A. Formicola et al., *The LUNA II 400 kV accelerator*, Nuclear Instruments and Methods in Physics research A, 507, 2003, DOI: 10.1016/S0168-9002(03)01435-9.

[36] P. Prati and on behalf of the LUNA collaboration, *The LUNA-MV facility at Gran Sasso*, J. Phys. Conf. Ser. 1342, 012088, 2020, DOI: 10.1088/1742-6596/1342/1/012088.

[37] A. Caciolli and on behalf of the LUNA collaboration, *Nuclear Astrophysics in underground laboratories: the LUNA experiment*, J. Phys. Conf. Ser. 1610 012002, 2020, DOI:10.1088/1742-6596/1610/1/012002.

[38] M. Haffke et al., *Background measurements in the Gran Sasso Underground Laboratory*, Nuclear Instruments and Methods in Physics Research A, 643 36-41, 2011, DOI: 10.1016/j.nima.2011.04.027.

[39] A. Empl et al, *Study of Cosmogenic Neutron Backgrounds at LNGS*, Instrumentation and Methods for Astrophysics, 2012, DOI: https://doi.org/10.48550/arXiv.1210.2708.

[40] R. Rossini et al., *A new multidisciplinary non destructive protocol for the analysis of stony meteorites: gamma spectroscopy, neutron and muon techniques supported by Raman microscopy and SEM-EDS*, J. Anal. At. Spectrom. 38, 293, 2023, DOI: 10.1039/d2ja00263a.

[41] R. Depalo, *Nuclear Astrophysics deep underground and the LUNA experiment*, Journal of Physics: Conf Series 1308, 2019, DOI: 10.1088/1742-6596/1308/1/012009.

[42] C. G. Cafferty, *Application of Bayesian and Geostatistical Modeling to the Environmental Monitoring of Cs-137 at the Idaho National Laboratory*, M.S. Thesis, Idaho National Laboratory, 2010.